UNIVERSITÀ
DEGLI STUDI
FIRENZE

Dottorato di Ricerca in
Ingegneria Industriale

Ciclo XXVI

Modelling of corrugated core sandwich panels in multidisciplinary optimization processes

Settore Scientifico Disciplinare ING/IND 14

Candidato
Dott. Giorgio Bartolozzi

Tutore
Prof. Marco Pierini

Coordinatore del Dottorato
Prof. Maurizio De Lucia

Controrelatore
Dr. Gerald Kress

Controrelatore
Prof. Patrice Cartraud

Anni 2011/2013

“Faber est suae quisque fortunae”

Sallustio

Abstract

Metal sandwich panels are becoming increasingly important as multi-functional components in many industrial areas. One of the main characteristics is their high stiffness-to-mass ratio, especially under bending conditions. This property strongly depends on the two faces, but other properties – acoustic, thermal, etc. – are governed by the core. Therefore, R&D in innovative cores is justified by the effort the industry is making to create multi-functional components that integrate good performances in different fields. The multi-functionality of components can be efficiently achieved by using multidisciplinary optimization (MDO) processes. Nevertheless, given their iterative nature, quick but accurate simulations are needed to define component characteristics.

In this context, the PhD activity reported in this dissertation aims at developing modelling techniques, even simplified, which allow determining the static and dynamic properties of all-metal corrugated core sandwich panels to include them in optimization processes. To begin with, an analytical formulation to represent a general corrugated core as an equivalent homogeneous layer is presented. The main limitations of already developed formulations are overcome by the proposed methodology. Moreover, given the absence in the literature of accurate formulations for sinusoidal cores, the general one is simplified to adapt it to that specific geometry.

Nevertheless, it is shown that, due to manufacturing processes, the real shape of the corrugation is different from the supposed sinusoidal shape. A measurement campaign – tensile testing and modal analysis – is performed to validate the analytical formulation and to prove the importance of modelling the real shape of the corrugation, especially for the modal analysis.

Finally, to show the industrial advantages of using the proposed modelling technique, a case study was investigated. An optimization process is set up on sinusoidal corrugated sandwich panels with both static and acoustic constraints applied, which would not be possible without the computational time reduction achieved by the analytical equivalent modelling proposed.

Contents

Abstract i

Contents iii

List of figures vii

List of tables xi

1 Introduction 1
- 1.1 Sandwich structures 1
- 1.2 Motivation and objective 2
- 1.3 Outline of the dissertation 5

2 State of the art 7
- 2.1 Introduction 7
  - 2.1.1 Naming convention for stresses 8
  - 2.1.2 Classical lamination theory and extension 8
- 2.2 Homogenization techniques for corrugated cores 10
  - 2.2.1 Triangular corrugation 11
  - 2.2.2 Circular and arc-and-tangent corrugations 12
  - 2.2.3 Trapezoidal corrugation 14
  - 2.2.4 Sinusoidal corrugation 16
- 2.3 Optimization methods 17
  - 2.3.1 Generalities 17
  - 2.3.2 Optimization problems for sandwich panels 18

3 Homogenization of corrugated cores 21
- 3.1 Introduction 21
- 3.2 Analytical formulation 22
  - 3.2.1 Transverse shear modulus G_{xz} 24
  - 3.2.2 Elastic modulus in x-direction E_x 29
  - 3.2.3 Elastic modulus in y-direction E_y 30
  - 3.2.4 In-plane Poisson's ratio ν_{xy} 31
  - 3.2.5 Transverse shear modulus in yz-plane G_{yz} 31
  - 3.2.6 In-plane shear modulus G_{xy} 32
  - 3.2.7 Mass density ρ_{eq} 33

3.3 Additional shear moduli 33
3.3.1 In-plane shear modulus G_{yx} 33
3.3.2 Transverse shear modulus in xz-plane G_{zx} 34
3.3.3 Transverse shear modulus in yz-plane G_{zy} 35
3.4 Additional parameters for a solid representation 35
3.4.1 Elastic modulus in z-direction E_z 35
3.4.2 Poisson's ratio in the *xz-plane* ν_{xz} 36
3.4.3 Poisson's ratio in the *yz-plane* ν_{zy} 37
3.5 Comparison with FE models 37
3.5.1 G_{xz} model 38
3.5.2 E_x model 38
3.5.3 E_y model 39
3.5.4 ν_{xy} model 39
3.5.5 G_{yz} model 40
3.5.6 G_{xy} model 40
3.5.7 G_{yx} model 41
3.5.8 G_{zx} model 41
3.5.9 G_{zy} model 41
3.5.10 Elastic modulus in z-direction E_z 42
3.5.11 Poisson's ratio in the *xz-plane* ν_{xz} 43
3.5.12 Poisson's ratio in the *yz-plane* ν_{yz} 43
3.5.13 Comparison of results 43
3.6 Comparison with previous results 45
3.6.1 Triangular-shaped cores 47
3.6.2 Circular-shaped cores 47
3.6.3 Arc-and-tangent cores 47
3.6.4 Trapezoidal-shaped cores 48
3.7 Discussion 50
3.8 Conclusions 51

4 A specific case: Sinusoidal corrugations 53
4.1 Introduction 53
4.2 Analytical simplified formulation 54
4.2.1 Transverse shear modulus G_{xz} 54
4.2.2 Elastic modulus in x-direction E_x 57
4.2.3 Elastic modulus in y-direction E_y 57
4.2.4 In-plane Poisson's ratio ν_{xy} 57
4.2.5 Transverse shear modulus in yz-plane G_{yz} 57
4.2.6 In-plane shear modulus G_{xy} 57
4.2.7 In-plane shear modulus G_{yx} 58
4.2.8 Transverse shear modulus G_{zx} 58
4.2.9 Transverse shear modulus G_{zy} 58
4.2.10 Elastic modulus in z-direction E_z 58
4.2.11 Poisson's ratio in the *xz-plane* ν_{zx} 58
4.2.12 Poisson's ratio in the *yz-plane* ν_{zy} 58
4.3 Comparison with FE models and previous authors 59

4.4 Static validation for sinusoidal cores 63
4.5 Acoustic validation for sinusoidal cores 65
4.6 Discussion 70
4.6.1 Comparison with FE models and previous authors 70
4.6.2 Static validation for sinusoidal cores 70
4.6.3 Acoustic validation for sinusoidal cores 71
4.7 Conclusions 71

5 Experimental validation 73
5.1 Introduction 73
5.2 Real shape of the corrugated cores 74
5.3 Modal analysis 75
5.3.1 Modal test method 76
5.3.2 Specimen details 78
5.3.3 FE models 79
5.3.4 Results 79
5.3.5 Conclusions 84
5.4 Tensile testing 85
5.4.1 Methodology 85
5.4.2 Specimen details 86
5.4.3 Results 87
5.4.4 Conclusions 89
5.5 Concluding remarks 90

6 Multidisciplinary optimization 93
6.1 Introduction 93
6.2 Methodology 95
6.2.1 Active-set optimization 95
6.2.2 Genetic Algorithm optimization 96
6.3 Optimization set-up 97
6.3.1 Structural constraints 98
6.3.2 Acoustic constraints 98
6.4 Optimization results 102
6.5 Discussion 103
6.6 Conclusions 105

7 Conclusions 107

A Experimental stress-strain curves 111

B Datasheets of tested panels 119

Bibliography 125

Acknowledgements 133

List of publications 137

List of Figures

1.1 Parallelism between sandwich structures and I-beams. 1
1.2 Different types of all-metal sandwich panels. 2
1.3 Different corrugations of sandwich panels. 3

2.1 Stress component nomenclature. 8

3.1 Global system of reference definition. 23
3.2 Sandwich panel with generic corrugated core shape: relevant parameters. 23
3.3 Mirroring process to obtain the two periodic curves. 24
3.4 Deformation in pure shear conditions for the G_{xz} parameter. . . . 25
3.5 Loads and forces acting on the centre line of the corrugation: nomenclature. 28
3.6 Deformation in tensile test for the E_x parameter. 29
3.7 Core approximation for G_{yz} and G_{xy} calculation. 31
3.8 Shear scheme for the G_{yx} parameter. 33
3.9 Shape and parameters of the validation case. 37
3.10 FE model for G_{xz} determination. 38
3.11 FE model for E_x determination. 39
3.12 FE model for E_y determination. 40
3.13 FE model for G_{yx} determination. 41
3.14 FE model for G_{zx} determination. 42
3.15 FE model for E_z determination. 43
3.16 Geometries and dimensions of the compared corrugated core structures. 44
3.17 Split of the trapezoidal core sandwich panel and nomenclature. . . 48

4.1 Loads and forces acting on the centre line: nomenclature. 54
4.2 Parameter comparison varying the core sheet thickness. 60
4.3 Parameter comparison varying the core sheet height. 61
4.4 Parameter comparison varying the corrugation period. 62
4.5 Additional parameter comparison varying the core sheet thickness. 63
4.6 Additional parameter comparison varying the core height. 63
4.7 Additional parameter comparison varying the corrugation period. . 64
4.8 Scheme of the bending test and used distances. 64

4.9 Parametric study on bending stiffness. 65
4.10 TL comparison for a set of parameters t. 66
4.11 TL comparison for a set of parameters h. 66
4.12 TL comparison for a set of parameters p. 67
4.13 Variation of sound TL with the core sheet thickness t. 68
4.14 Variation of sound TL with the core corrugation height $2h$. 68
4.15 Variation of sound TL with the core corrugation half-period p. . . 69

5.1 Comparison of theoretical sine (red lines) and real curves (blue lines) on the scanned images. 74
5.2 Instrumentation for the modal testing. 76
5.3 AutoMAC matrix for measurement point selection. 77
5.4 Positions of stations for the modal testing. 77
5.5 Panel marked and equipped. 78
5.6 Support of the panel for modal testing. 79
5.7 05_02_05 H6 panel. MAC comparison between experimental data and FE models. 81
5.8 08_02_05 H6 panel. MAC comparison between experimental data and FE models. 82
5.9 10_03_10 H6 panel. MAC comparison between experimental data and FE models. 83
5.10 10_03_10 H11.5 panel. MAC comparison between experimental data and FE models. 84
5.11 Tensile test setup for testing along the: (a) *y-direction*, (b) *x-direction*. 86
5.12 Tensile test specimens. 86
5.13 Resin reinforced specimens. 87
5.14 Comparison between experimental Young's modulus and analytical values in the *x-direction*. 88
5.15 Comparison between experimental Young's modulus and analytical values in the *y-direction*. 88

6.1 Typical train floor structure. 94
6.2 Inner floor cross section and optimization variables. 94
6.3 Parametric study on the TL spectra: influence of the t_u variable. . 100
6.4 Parametric study on R_w: influence of the t_u variable. 100
6.5 Parametric study on the TL spectra: influence of the t_c variable. . 101
6.6 Parametric study on R_w: influence of the t_c variable. 101
6.7 R_w with narrower bands. 101
6.8 Objective function trends for the GB method. 102
6.9 TL comparison: asymmetric and symmetrized configurations. . . . 105

A.1 Panel 05_02_05 H6 – *x-direction* 111
A.2 Panel 05_02_05 H6 – *y-direction* 112
A.3 Panel 08_02_05 H6 – *x-direction* 113
A.4 Panel 08_02_05 H6 – *y-direction* 114
A.5 Panel 10_03_10 H6 – *x-direction* 115

A.6 Panel 10_03_10 H6 – *y-direction* 116
A.7 Panel 10_03_10 H11.5 – *x-direction* 117
A.8 Panel 10_03_10 H11.5 – *y-direction* 118

List of Tables

3.1 Comparison of equivalent parameters for the validation geometry – beam representation. 44
3.2 Comparison of additional equivalent parameters for the validation geometry – beam representation. 45
3.3 Comparison of equivalent parameters for triangular profile geometries – plate representation. 46
3.4 Comparison of equivalent parameters for circular profile geometries – plate representation. 46
3.5 Comparison of equivalent parameters for arc and tangent profile geometries – plate representation. 46
3.6 Comparison of equivalent parameters for trapezoidal profile geometries – plate representation. 49

4.1 TL difference in dB, averaged over the frequencies, varying the core sheet thickness. 67
4.2 TL difference in dB, averaged over the frequencies, varying the core height. 69
4.3 Characteristics of the used hardware. 69

5.1 Main dimensions of the available panels. 73
5.2 Comparison of equivalent parameters for theoretical and real corrugation profiles. 75
5.3 Aluminum properties used. 75
5.4 Comparison of eigenfrequencies for the 05_02_05 H6 panel. 81
5.5 Comparison of eigenfrequencies for the 08_02_05 H6 panel. 82
5.6 Comparison of eigenfrequencies for the 10_03_10 H6 panel. 83
5.7 Comparison of eigenfrequencies for the 10_03_10 H11.5 panel. . . . 84
5.8 Summary of measured Young's moduli. 89
5.9 Comparison equivalent Young's moduli for the complete tested panels. 90

6.1 Inner floor dimensions. 97
6.2 Design variable ranges. 97
6.3 Analytical deflection formulas using Timoshenko beam theory. . . 99
6.4 Optimal results obtained with the various techniques. 102
6.5 Comparison of the different optimization methods. 103

Chapter 1

Introduction

1.1 Sandwich structures

A sandwich structure typically consists of two thin faces, or “skins”, made from stiff and strong material bonded to a lightweight material called “core”. The behaviour of such a structure reflects, in two dimensions, the concept of the I-beam, which is an efficient structural shape because as much as possible of the material is placed in the flanges situated farthest from the center of bending or neutral axis – Figure 1.1. Indeed, also for sandwich structures, the main contribution of the skins is to support bending loads, while the core transfers shear force between the faces and resists buckling loads. In a more general way, American Society for Testing and Materials (ASTM) gave the following definition: “A structural sandwich is a special form of a laminated composite comprising of a combination of different materials that are bonded to each other so as to utilize the properties of each separate component to the structural advantage of the whole assembly”.

In particular, the main advantage of these structures is a combination of low density and high flexural stiffness. This feature allows these structures to become extremely popular in aerospace and marine applications, where weight is a major issue, e.g. in commercial planes, pleasure boats, space shuttles and satellites. But also in ground transportation they are increasingly found in cars, buses and trains.

The good stiffness properties of a sandwich construction can be illustrated by the following example. A structure made up of a homogeneous material with a given Young’s modulus and strength having unit width and thickness t will have a certain bending stiffness which is normalized as 1. Then the beam is cut into two

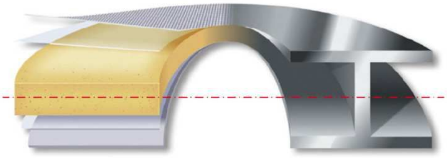

Figure 1.1: Parallelism between sandwich structures and I-beams.

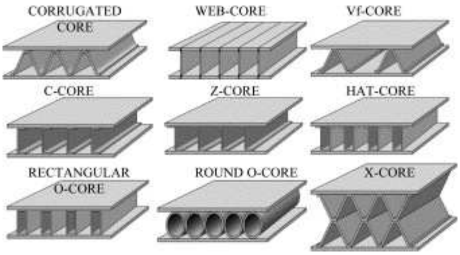

Figure 1.2: Different types of all-metal sandwich panels.

halves of thickness $t/2$ and a core material of thickness $2t$ is bonded between these two halves. The corresponding stiffness and strength is 12 and 6 times more than the homogeneous beam respectively. This phenomenon is called *sandwich effect*. Assuming the core to have a surface density much lower than the face sheets, the gain in bending stiffness is obtained at no addition in weight to the structure.

Depending on the requirements the structure has to fulfill, the choice of the materials to be combined can vary a lot, especially for the core layer, enabling design of multi-functional structures. Indeed, if the skins are usually made of metal or fiber composite, the core layer can be realized with several materials. Cellular foams, e.g. polymer or metal foams, honeycomb core, and balsa wood, are very common in structural applications. In this context, all-metal sandwich structures are very effective in transferring shear forces with a reduced mass per unit area and they can have several different core topologies, as shown in Figure 1.2.

Among all-metal sandwich structures, the corrugated core ones are a very interesting solution which is based on the same concept behind the corrugated cardboard. Nevertheless, due to the higher properties of metals respect to paper, more accurate and precise manufacturing processes can be implemented to build a corrugation tailored on industrial requirements. As a consequence, several corrugation profiles are available on the market, see Figure 1.3, whose characteristics can vary in a very wide range.

One example is the acoustical properties of these panels. These characteristics are to a large extent governed by the detailed design of the core. If the design of the panel is made entirely based only on the mechanical constraints (deflection, stress), a structure that is a poor sound barrier may be obtained and unnecessarily heavy designs may result from the needed addition of damping layers to control the noise transmission.

1.2 Motivation and objective

The great variability of the overall behaviour of the sandwich structures as a function of the core properties, if on the one hand allows a customization of the structure to the imposed requirements, on the other hand requires a proper tool for their design. This is even more relevant when a multi-functional structure is desired. The most efficient way to achieve this goal is to use a multi-disciplinary

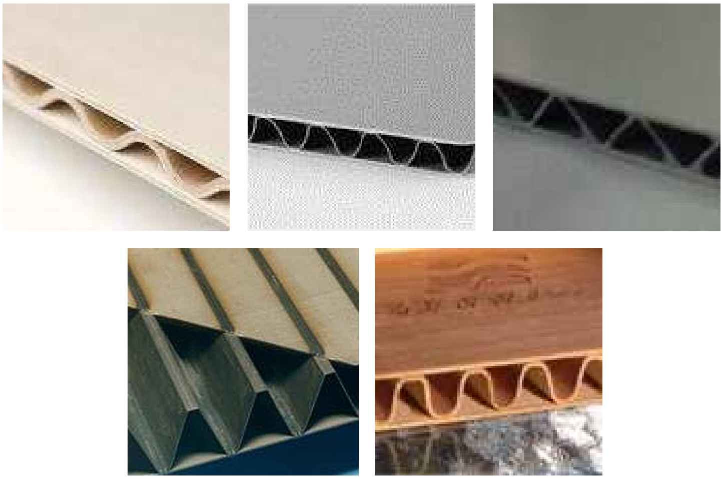

Figure 1.3: Different corrugations of sandwich panels.

optimization (MDO) method. Nevertheless, it is implicitly included in the optimization idea, the iterative nature of such processes. At each iteration of the optimization process, the main parameters of the problem must be computed, e.g. objective and constraint functions, even several times. It is therefore obvious that, to include different performance parameters of the investigated structure in an optimization process, they must be determined in a quick and reliable way.

If the determination of static structural properties, both with analytical or finite element (FE) techniques, is a relatively fast process, the computation of some other properties can be very time consuming, e.g. crash or acoustic simulations. The reason behind the long computational times even for relatively simple structures, as a panel may appear, is the necessary refinement in the model, usually composed of finite elements, to accurately reproduce the complex shaped cores. It is therefore necessary to develop simplifying methodologies which allow a consistent reduction of the computational times required.

The need of simplified models is particularly relevant when sandwich structures are only a part of the assembly to be optimized. As an example, consider one of the main applications of sandwich panels with corrugated cores, i.e. inner components in floor structures of train passenger compartments. These floors should be multi-functional components which combine good structural, sound reduction and thermal insulation properties. In addition, a greater focus on lightweight and thin floor designs is desired to achieve total weight reduction resulting either in lower energy consumption or in higher payload. For this reason, traditional floor panels made of wood are being replaced by lightweight sandwich structure. Nevertheless, the classical design process for vehicle structures, which typically addresses different properties of a new product/design in different phases, may result in iteration loops to meet critical design variables, which may cause project delays and added cost in the design phase. Moreover, typically the structural design is dealt with at first, since it determines safety related aspects like crash resistance and structural fatigue, but on the other hand it implies that the design space for finding solutions that fulfill the complete list of requirements is more and more limited as the design becomes more mature. In this context, integration of MDO into the every-day design process may potentially both reduce cost and time in the design phase of new vehicle projects and allow finding design solutions integrating several functions within the same structure.

In order to apply MDO to sandwich structures, the typical procedure to simplify the models and speed up simulations consist in replacing the heterogeneous core layer with a kind of equivalent material model. This process is called *homogenization*. Several methodologies exist to do that: experimental tests, FE-based techniques and analytical formulations. Obviously, if experimental results may probably give the best accuracy, they are not feasible for the inclusion in optimization processes. FE-based techniques and analytical formulations have different characteristics which also depend on the kind of core under investigation. Restricting to corrugated cores, which are the target of the present dissertation, FE-based techniques were usually preferred to analytical formulations, since analytical formulations ware available only for some types of corrugation, thus restricting their applicability.

In this context, the main objective of the work presented in this dissertation is to propose tools for a simplified, yet accurate, modelling of the complex shaped core of corrugated core sandwich panels. In particular, a general analytical formulation, which can address all kinds of corrugations, is proposed to homogenize the core and represent it as an orthotropic material. All the elastic parameters for a complete description of the orthotropic material are given, including the in-plane and out-of-plane properties.

Moreover, this dissertation has a particular focus on sinusoidal core sandwich panels, which are one solution, proposed by Bombardier Transportation Sweden, for inner floors of train vehicles. In particular, given the absence in the literature of a satisfactory analytical formulation for such corrugation, a simplified version of the general formulation proposed is also given.

The accuracy of the proposed analytical formulation is then proved by means of a measurement campaign which involved both the static and dynamic behaviour of the sandwich structure with sinusoidal core. Moreover, the importance of accurately representing the corrugation profile is highlighted by the comparison of measurement data with results from the general analytical formulation and the specific sinusoidal formulation. Indeed, the greater accuracy of the general formulation is motivated by its capability to determine equivalent parameters for the real corrugation shape, which can differ considerably because of its manufacturing processes.

Finally, a MDO pilot study is presented to show the potentiality of the equivalent modelling in the real industrial design. The secondary aim of that pilot study is also to compare and assess different optimization algorithms in the presence of a complex acoustic constraint as the one defined for these structures.

1.3 Outline of the dissertation

This dissertation consists of seven chapters and two appendices. Chapter 2 gives a detailed overview of the state of the art. It will cover both analytical formulations for the homogenization of corrugated cores and relevant applications of optimization processes to sandwich structures. This serves as a motivation and a basis for the proposed general analytical formulation and application cases in the following chapters. Chapter 3 presents and explains the analytical formulation developed in this work and compares results with the authors introduced in Chapter 2 for several corrugation profiles. A particular core type, i.e. sinusoidal corrugated core, is deeply investigated in Chapter 4. For this particular shape, indeed, the general formulation can be simplified to overcome the lack of accurate formulations in the literature for this core shape. Chapter 5 has a twofold aim. First, it shows the great difference in equivalent parameters assuming either the shape of the real corrugation, which can be modelled only with the formulation in Chapter 3, or the supposed sinusoidal curve, modelled with the simplified formulation given in Chapter 4. The second objective of this chapter is to prove the accuracy of the proposed formulation by comparing the static and dynamic behaviour of the sandwich structure with experimental data. Finally, in Chapter 6, an application case of the proposed homogenized modelling is given. It consists in a multidisciplinary optimization applied to the sinusoidal corrugated core subjected both to mechanical and acoustic constraints.

In Chapter 7 general conclusions are made together with a discussion of possible improvements. Appendix A includes all the measured stress-strain curves for the tested specimens in Chapter 5. Finally, Appendix B contains the datasheets of the tested panels.

Chapter 2

State of the art

2.1 Introduction

The inclusion of MDO in the design process is an increasing need of the industry, especially the transportation industry. Indeed, the number of requirements constantly increases and more and more functional performance attributes have to be addressed. Nevertheless, to contemporarily include in the optimization process several disciplines, such as crashworthiness, interior and exterior acoustics, structural statics, etc., the performances in those fields must be computed in short times and with a very good accuracy. This need pushes the researchers to find proper tools to speed up simulations, especially in the very first stage of the design process, i.e. the concept stage, when a fast exploration of the design space is required.

The need of simplifying tools is particularly relevant for innovative structures as the all-metallic sandwich panels are. Indeed, the difference between the overall dimensions of these panels and the geometric characteristics of the core is very high. When modelling these structures with FE-based techniques, a proper representation of the typically complex shaped cores requires the element dimensions to reduce, drastically increasing the total number of elements needed to model the complete panel. Therefore, to include these structures in MDO processes, especially if they are not the only component to be optimized, a strong reduction of the number of elements is necessary.

In this regard, the current chapter treats the state-of-the-art techniques to reduce the complex shaped core of the corrugated core sandwich panels to an equivalent homogeneous layer, Section 2.2. Moreover, an insight in the literature regarding optimization processes applied to sandwich structure is given in Section 2.3.

Before going into the details of the state-of-the-art analysis, it is worth specifying the naming convention used in this dissertation and the way to determine the stiffness properties of the complete panel, starting from the three layers. This information will be useful to understand the present and following chapters.

2.1.1 Naming convention for stresses

Due to the different results found in the literature on some parameters of the homogenized core layer, it is worth to specify the convention used in the present dissertation for naming stresses and strains.

The author chose the naming convention for stress components on a 3D element that uses two subscripts: the first indicating the direction of the stress component and the second indicating the plane on which the stress component acts, i.e. the plane whose outward normal is in the indicated direction – see Figure 2.1.

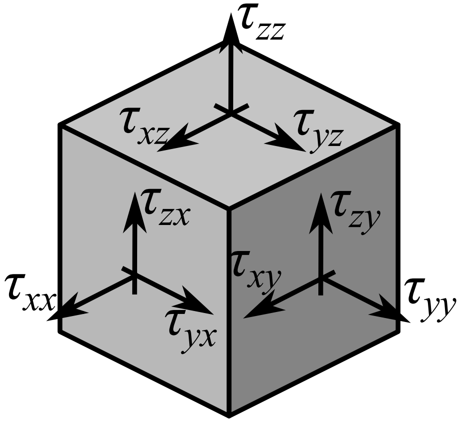

Figure 2.1: Stress component nomenclature.

Some authors used the opposite convention for the subscript meaning. Nevertheless, to have accordance in the notation, it is sufficient to switch subscripts when needed. Moreover, in this dissertation, when the parameters are introduced, the direction of the involved stresses is explicitly mention to avoid errors.

2.1.2 Classical lamination theory and extension

The Classical Lamination Theory (CLT) aims to relate the mechanical response of a layered plate to that of the individual constituent piles. This theory is an extension of the theory for homogeneous isotropic plates presented by Timoshenko and Woinowsky-Krieger [1] to thin laminated plates. The analysis is most appropriate for thin plates since this theory does not accommodate transverse shear deformation. Hence, CLT would be of limited applicability to sandwich panels since they often possess a thick, shear deformable core. Nevertheless, the first-order shear deformation model assumed in this dissertation combine the CLT for the in-plane properties with the addition of the transverse shear moduli for the inclusion of the out-of-plane shear behaviour. The assumption of *perfect bonding* is maintained from CLT, which implies:

1. the bonding itself is infinitesimally small (there is no flaw or gap between layers);

2. the bonding is non-shear-deformable (no lamina can slip relative to another);
3. the strength of bonding is as strong as it needs to be (the laminate acts as a single lamina with special integrated properties).

For the in-plane behaviour, the first step consists in writing the constitutive relations of each layer according to the material properties. In the cases presented in this dissertation, the skins are supposed to be isotropic, thus the constitutive relation, in stiffness form $\boldsymbol{C}$, can be written as:

$$\begin{Bmatrix} \sigma_{xx} \\ \sigma_{yy} \\ \sigma_{xy} \end{Bmatrix} = \frac{E}{1-\nu^2} \begin{bmatrix} 1 & \nu & 0 \\ \nu & 1 & 0 \\ 0 & 0 & \frac{1-\nu}{2} \end{bmatrix} \begin{Bmatrix} \epsilon_{xx} \\ \epsilon_{yy} \\ \gamma_{xy} \end{Bmatrix} \tag{2.1}$$

The core layer is supposed to have an orthotropic behaviour, thus the constitutive relation, still in stiffness form, for this layer, can be found as:

$$\begin{Bmatrix} \sigma_{xx} \\ \sigma_{yy} \\ \sigma_{xy} \end{Bmatrix} = \frac{1}{1-\nu_{xy}\nu_{yx}} \begin{bmatrix} E_x & \nu_{yx}E_y & 0 \\ \nu_{xy}E_x & E_y & 0 \\ 0 & 0 & G_{xy}(1-\nu_{xy}\nu_{yx}) \end{bmatrix} \begin{Bmatrix} \epsilon_{xx} \\ \epsilon_{yy} \\ \gamma_{xy} \end{Bmatrix} \tag{2.2}$$

Note that in both cases, γ_{xy} is the engineering shear strain related to the shear strain as $\gamma_{xy} = 2\epsilon_{xy}$.

Once these matrices are found, which means that the equivalent parameters for an orthotropic representation of the core layer are determined, the stiffness matrix of the complete panel can be obtained as:

$$\boldsymbol{C_{TOT}} = \frac{\boldsymbol{C_1} \cdot t_1 + \boldsymbol{C_c} \cdot H_0 + \boldsymbol{C_2} \cdot t_2}{t_1 + t_2 + H_0} \tag{2.3}$$

being $\boldsymbol{C_1}$ and $\boldsymbol{C_2}$ the stiffness matrices of the lower and upper face with thickness t_1 and t_2 respectively, while $\boldsymbol{C_c}$ is the stiffness matrix of the equivalent layer, representing the core, with thickness H_0.

Nevertheless, when dealing with CLT, it is most common to use the matrices $\boldsymbol{A}$, $\boldsymbol{B}$ and $\boldsymbol{D}$. These matrices can be defined considering resultants (forces $\boldsymbol{N}$ and moments $\boldsymbol{M}$) and the strains (strains $\boldsymbol{\epsilon}$ and curvatures $\boldsymbol{\kappa}$) in the constitutive relations, thus:

$$\begin{aligned} \begin{Bmatrix} N_{xx} \\ N_{yy} \\ N_{xy} \end{Bmatrix} &= \begin{bmatrix} A_{1,1} & A_{1,2} & A_{1,3} \\ & A_{2,2} & A_{2,3} \\ sym. & & A_{3,3} \end{bmatrix} \begin{Bmatrix} \epsilon_{xx} \\ \epsilon_{yy} \\ \gamma_{xy} \end{Bmatrix} + \begin{bmatrix} B_{1,1} & B_{1,2} & B_{1,3} \\ & B_{2,2} & B_{2,3} \\ sym. & & B_{3,3} \end{bmatrix} \begin{Bmatrix} \kappa_{xx} \\ \kappa_{yy} \\ 2\kappa_{xy} \end{Bmatrix} \\ \begin{Bmatrix} M_{xx} \\ M_{yy} \\ M_{xy} \end{Bmatrix} &= \begin{bmatrix} B_{1,1} & B_{1,2} & B_{1,3} \\ & B_{2,2} & B_{2,3} \\ sym. & & B_{3,3} \end{bmatrix} \begin{Bmatrix} \epsilon_{xx} \\ \epsilon_{yy} \\ \gamma_{xy} \end{Bmatrix} + \begin{bmatrix} D_{1,1} & D_{1,2} & D_{1,3} \\ & D_{2,2} & D_{2,3} \\ sym. & & D_{3,3} \end{bmatrix} \begin{Bmatrix} \kappa_{xx} \\ \kappa_{yy} \\ 2\kappa_{xy} \end{Bmatrix} \end{aligned} \tag{2.4}$$

Combining the above equations:

$$\begin{Bmatrix} \boldsymbol{N} \\ \boldsymbol{M} \end{Bmatrix} = \begin{bmatrix} \boldsymbol{A} & \boldsymbol{B} \\ \boldsymbol{B} & \boldsymbol{D} \end{bmatrix} \begin{Bmatrix} \boldsymbol{\epsilon} \\ \boldsymbol{\kappa} \end{Bmatrix} \tag{2.5}$$

The matrix $\boldsymbol{A}$ is called the extensional stiffness, $\boldsymbol{B}$ is the coupling stiffness, and $\boldsymbol{D}$ is the bending stiffness of the laminate. The components of these three matrices are defined as follows:

$$A_{i,j} = \sum_{k=1}^{N} \left(C_{i,j_{TOT}}\right)_k t_k \tag{2.6}$$

$$B_{i,j} = \sum_{k=1}^{N} \left(C_{i,j_{TOT}}\right)_k t_k \overline{z}_k \tag{2.7}$$

$$D_{i,j} = \sum_{k=1}^{N} \left(C_{i,j_{TOT}}\right)_k \left(t_k \overline{z}_k^2 + \frac{t_k^3}{12}\right) \tag{2.8}$$

where t_k is the thickness of the *k-th* layer and $\overline{z}_k$ is the distance from the mid-plan to the centroid of the *k-th* layer.

In the literature, sometimes the matrix $\boldsymbol{A}$ is given, but the matrix $\boldsymbol{C_{TOT}}$ can be easily obtained and consequently the various parameters of the equivalent orthotropic material for the complete panel.

For the out-of-plane properties, a series behaviour of the layers is supposed and the total shear modulus $G_{iz_{TOT}}$ can be found as

$$G_{iz_{TOT}} = \frac{t_1 + t_2 + H_0}{\frac{t1+t2}{G} + \frac{H_0}{G_{iz}}} \tag{2.9}$$

being G the shear modulus of the face material, G_{iz} the equivalent shear modulus of the corrugated core with $i = x, y$.

2.2 Homogenization techniques for corrugated cores

As already introduced, in order to limit model dimensions – and consequently the computational time – a standard procedure consist in reducing the complex shaped core of the sandwich structure to an equivalent homogeneous layer. The properties of this layer strongly depends on the core main characteristics, i.e. the constituent material and the geometry of the profile. The determination of the properties of the equivalent layer has been under investigation for the last decades with two main methodologies used: (i) FE based techniques and (ii) analytical formulations. The main advantage of analytical formulations over FE techniques is that the computation of the equivalent parameters is much quicker. Nevertheless, analytical formulation was developed in the past typically for only one type of core, as highlighted by Cheng et al. [2]: “the resulting complex expressions for one specific sandwich form cannot be applied to other types”.

Given the strong dependency of analytical techniques on the core geometry, several different studies were carried out in the past dealing with different core typologies, see Mackerle [3] for a deep bibliographic study up to 2001. In particular, honeycomb cores have been extensively investigated [4, 5, 6] even with particular sinusoidal-shaped cells [7, 8, 9, 10]. Moreover, increasing importance is given to lightweight cellular cores [11, 12]. For the sake of clarity, since this field is very extended, the following literature review is focused only on the corrugated core sandwich structures modelled analytically, which is the target of this dissertation.

As already mentioned before, the main drawback of analytical formulations, up to the method developed in this work, is the lack of generality, thus in the following each mentioned reference typically addresses only one corrugation geometry. It is important noting that, due to different definitions of the system of reference in the various papers, in the following review, parameter names are changed from the original published articles in order to harmonize results.

2.2.1 Triangular corrugation

For the triangular corrugation, the most important authors are Wang and Chung, who described in [13] the main parameters to homogenize that core and compared the accuracy with FE simulations. They developed an analytical formulation supposing that each inclined part of the corrugation behaves as a straight beam.

In their formulation, parameters E_y, G_{yx} an G_{yz} are derived from the pioneering study of Libove and Batdorf [14]. In determining the other equivalent moduli, they assume an Euler-Bernoulli beam behaviour, thus neglecting the shear deformation of the stiffeners. All the parameters for a representation of the core as an equivalent orthotropic homogenous solid layer are derived. Given the simplicity of the corrugation geometry it is possible to explicitly write the equations for the determination of the parameters as listed in Eqs. 2.10. It is important noting that in Eqs. 2.10, subscripts of the Poisson's ratios are switched from those of the paper, since there a different notation is used for these parameters. For example, the ν_{xy} parameter in [13] is associated with a loading in the *y-direction*, while in this work is considered associated with a loading in the *x-direction.*

$$\begin{aligned}
E_x &= \frac{E t_c^3 \cos\theta}{(H_0^2 - t_c^2\cos^2\theta)H_0} \\
E_y &= E\frac{t_c}{p\ \sin\theta} \\
E_z &= \frac{E t_c^3 \sin\theta}{p^3 - p t_c^2 \sin^2\theta} \\
\nu_{yx} &= \nu \\
\nu_{xy} &= \nu\frac{t_c^2\cos^4\theta}{p^2\sin^2\theta - t_c^2\cos^4\theta} \\
\nu_{zx} &= \frac{p^2\sin^2\theta + t_c^2\sin^2\theta\cos^2\theta}{-p^2\cos^2\theta + t_c^2\sin^2\theta\cos^2\theta} \\
\nu_{xz} &= \nu_{zx}\frac{E_x}{E_z} \\
\nu_{yz} &= \nu
\end{aligned} \tag{2.10}$$

$$
\begin{aligned}
\nu_{zy} &= \nu \frac{t_c^2 \sin^2 \theta}{p^2 - t_c^2 \sin^2 \theta} \\
G_{yx} &= G \frac{p t_c \sin \theta}{H_0^2} \\
G_{xz} &= \frac{E t_c \sin \theta \cos^2 \theta}{p} \\
G_{zy} &= G \frac{t_c \sin \theta}{p}
\end{aligned}
$$

where t_c is the thickness of the corrugated lamina, E and ν are the Young's modulus and Poisson's ratio of the constituent material, H_0 is the height of the corrugation amplitude, p is half the period of the corrugation, θ is the inclination angle of the side of the corrugation.

In that paper, validation of the formulation is carried out by comparing the bending behaviour of a 3D FE model of the panel with a simplified laminate plate panel that makes use of the developed equations to characterize the orthotropic material constituting the equivalent layer of the core. As expected, the equivalent model is slightly stiffer than the original 3D model. Nevertheless, no direct check on the single parameters is shown.

Another interesting research on sandwich panels with triangular corrugations was performed by Valdevit et al. [15], who analytically derived the bending behaviour both in longitudinal and transverse direction. In particular, existing models for core failure under bending conditions were compared and extended. As a consequence, critical loads for different failure mechanisms were determined analytically. Moreover, Valdevit et al. [16] studied the possible combination of different layers of triangular corrugations, obtaining the so called "diamond corrugations". Nevertheless, also this second work is focused on failure mechanism and the analytical modelling does not deal with equivalent material parameters.

2.2.2 Circular and arc-and-tangent corrugations

The first analytical formulation for circular corrugated plates is probably that by Briassoulis [17] in 1986. It is a very simple formulation which considers only the in-plane behaviour of the corrugated lamina and allows obtaining the extensional rigidities as a function of the constituent material and the geometric parameters. Nevertheless, when considering circular and arc-and-tangent profiles, the most recent and accurate work is that by Kress and Winkler [18] in 2010. In their work, they proposed an analytical formulation to derive, for the equivalent layer, the matrices $\boldsymbol{A}$ and $\boldsymbol{D}$ of the CLT – see Section 2.1.2. Also in this case, since the shape can be easily represented by a closed-form explicit formula, the deriving equations for the two equivalent matrices, called $\widetilde{\boldsymbol{A}}$ and $\widetilde{\boldsymbol{D}}$, are relatively simple and they are expressed as a function of the constituent material matrices $\boldsymbol{A}$ and $\boldsymbol{D}$. From the $\widetilde{\boldsymbol{A}}$ matrix, the equivalent parameters for the in-plane behaviour can be derived with inverse formulas of Eqs. 2.2 and 2.6.

The corrugation, both circular and arc-and-tangent type, is defined by the parameters P and c, respectively period and half amplitude of the corrugation.

The condition on c is

$$0 < c \leq \frac{2+\sqrt{3}}{4}P \tag{2.11}$$

Therefore the radius of the corrugation and the reference angle ψ_0 as defined in [18] can be found as

$$R = \frac{16c^2 + P^2}{32c} \tag{2.12}$$

$$\psi_0 = \begin{cases} \arcsin\left(\frac{P}{4R}\right), & c \leq \frac{P}{4} \\ \arccos\left(\frac{P}{4R}\right) + \frac{\pi}{2}, & c \geq \frac{P}{4} \end{cases} \tag{2.13}$$

Since the bending rigidities contained in $\widetilde{\boldsymbol{D}}$ are out of the scope of the present work, only the equations needed to obtain the matrix $\widetilde{\boldsymbol{A}}$ are listed in Eqs. 2.14. For more details on the formulation, the reader is referred to [18].

$$\begin{aligned} \widetilde{A}_{1,1} &= \frac{|\boldsymbol{A}|D\psi_0 + 4A_{1,2}^2\kappa^2 D_{2,2}\sin^2\psi_0}{\sin\psi_0 A_{2,2}D} \\ \widetilde{A}_{1,2} &= \frac{4A_{1,2}\kappa^2 D_{2,2}\sin\psi_0}{D} \\ \widetilde{A}_{2,2} &= \frac{4A_{2,2}\kappa^2 D_{2,2}\sin\psi_0}{D} \\ \widetilde{A}_{3,3} &= A_{3,3}\frac{\sin\psi_0}{\psi_0} \end{aligned} \tag{2.14}$$

where

$$D = 2\psi_0\left(A_{2,2}(2+\cos(2\psi_0)) + \kappa^2 D_{2,2}\right) + (-3A_{2,2} + \kappa^2 D_{2,2})\sin(2\psi_0) \tag{2.15}$$

In a parallel study of the same year, Winkler and Kress [19] also developed a formulation to obtain the equivalent deformation of the corrugated ply as a function of the constituent material limits. In 2011 [20], the same authors also developed a FE based technique to derive the equivalent stiffness matrices $\widetilde{\boldsymbol{A}}$ and $\widetilde{\boldsymbol{D}}$. The method is compared with the formulation developed in [18], but could be extended to other corrugation types. Finally, in 2012 [21] they also carried out an interesting study on the influence of geometrical changes of the corrugation shape on the stiffness matrices by using FE simulations.

A similar shape investigated in the literature is that by Yokozeki et al. [22], that is composed of circular semicircumferences with vertical segments that divide them. Yokozeki et al. [22] studied the structural performance of such corrugations and derived some of the equivalent parameters. Xia et al. [23] then deepened the investigation, deriving an accurate set of equations for the equivalent stiffness matrix $\widetilde{\boldsymbol{A}}$. When the half length of the vertical segment L, is set to zero, the formulation by Xia et al. [23] can also be used for circular corrugations. In Eq. 2.16 the developed equations are listed.

$$
\begin{aligned}
\widetilde{A}_{1,1} &= 2p \Bigg/ \left(\frac{I_1}{A_{1,1}} + \frac{I_2}{D_{1,1}} \right) \\
\widetilde{A}_{1,2} &= \frac{A_{1,2}}{A_{1,1}} \widetilde{A}_{1,1} \\
\widetilde{A}_{2,2} &= \frac{A_{1,2}\widetilde{A}_{1,2}}{A_{1,1}} + \frac{l}{p} \frac{A_{1,1}A_{2,2} - A_{1,2}^2}{A_{1,1}} \\
\widetilde{A}_{3,3} &= \frac{p}{l} A_{3,3}
\end{aligned}
\tag{2.16}
$$

where $l = \pi R + 2L$ is the half length of the corrugation and I_1 and I_2 are defined as follows:

$$
\begin{aligned}
I_1 &= \pi R \\
I_2 &= \frac{4L^3}{3} + 2\pi L^2 R + 8LR^2 + \pi R^3
\end{aligned}
\tag{2.17}
$$

2.2.3 Trapezoidal corrugation

The trapezoidal corrugated panel, often improperly addressed as “corrugated”, is the most investigated in the literature. The first study on this core profile was by Libove and Batdorf [14] in 1948 and the pioneering article by Libove and Hubka [24] in 1951. The latter was furthermore developed by Ko [25] in 1980 generalizing that approach to corrugated panels with non-constant thickness. These authors studied the behaviour of the complete panel, thus including the two skins.

Samanta and Mukhopadhyay [26] in 1999 derived the extensional rigidities, i.e. the components of the $\boldsymbol{A}$ matrix, for the sole core. They used an energetic approach based on the Castigliano’s theorem [27] to find the deflection of the corrugated beams constituting the trapezoidal geometry. A beam type representation of the corrugation is used, assuming unit width. The deriving equations are listed in Eq. 2.18, where formulas are re-arranged according to the notation by Xia et al. [23].

$$
\begin{aligned}
\widetilde{A}_{1,1} &= \frac{2p}{I_2} \frac{Et_c^3}{12} \\
\widetilde{A}_{1,2} &= \nu \widetilde{A}_{1,1} \\
\widetilde{A}_{2,2} &= \frac{l}{p} Et_c \\
\widetilde{A}_{3,3} &= \frac{p}{l} \frac{Et_c}{2(1+\nu)}
\end{aligned}
\tag{2.18}
$$

where the half length of the corrugation l and I_2 are defined as follows:

$$\begin{aligned} l &= \frac{2h}{\sin\alpha} + p - \frac{2h}{\tan\alpha} \\ I_2 &= \frac{4h^3}{3\sin\alpha} + 2h^2\left(p - \frac{2h}{\tan\alpha}\right) \end{aligned} \tag{2.19}$$

The same corrugation geometry was studied by Xia et al. [23], which improved that formulation obtaining the same formulas as in Eqs. 2.16, where the half length of the corrugation l and I_2 are still obtained as in Eqs. 2.19 and I_1 is defined in [23] as:

$$I_1 = \frac{4h\cos\alpha}{3\sin\alpha} + 2p - \frac{4h}{\tan\alpha} \tag{2.20}$$

Nevertheless, it is believed that an error is present in that paper, probably due to a clerical error, and the same coefficient should be:

$$I_1 = \frac{4h\cos^2\alpha}{\sin\alpha} + 2p - \frac{4h}{\tan\alpha} \tag{2.21}$$

The formulation proposed by Xia et al. [23] is claimed to be valid for every corrugation geometry. Nevertheless, the coefficients I_1 and I_2 are dependent on the geometry and closed-form formulas are given only for the two mentioned corrugation types. The general formulation for these two parameters defines them as

$$\begin{aligned} I_1 &= \int_0^{2l} \left(\frac{\mathrm{d}x}{\mathrm{d}s}\right)^2 \mathrm{d}s \\ I_2 &= \int_0^{2l} f^2(x)\mathrm{d}s \end{aligned} \tag{2.22}$$

where $f(x)$ is the function describing the corrugation geometry and s is the local coordinate defined by the tangent direction to the sheet in the xz plane.

It is important noting that, as in the previous corrugation types, only the in-plane behaviour was studied by the found authors.

Mentioning other papers that studied this kind of corrugation, Chang et al. [28] investigated the bending behaviour of the sandwich panel, deriving analytical formulas for the deflection of the structure under bending conditions. Moreover, Lok and Cheng [29] studied a truss-core sandwich panel which is similar to a trapezoidal corrugation. Nevertheless, the equivalent panel is derived for the total panel and in terms of equivalent bending rigidities, which are out of the scope of the present work of thesis.

Finally, Liew et al. [30] performed and interesting vibrational analysis of trapezoidal and sinusoidal corrugated plates, using a mesh-free Galerkin method to numerically solve the eigenproblem. Nevertheless, when considering an equivalent plate for the two corrugation types, results from previous formulations were used.

2.2.4 Sinusoidal corrugation

The study of homogenization techniques on sinusoidally corrugated core sandwich panels is mainly limited in the literature to cardboard panels. As already seen for the other corrugation types, both analytical and FE-based methodologies are used to derive the equivalent material properties. Nevertheless, since the field of investigation is restricted to panels whose constituent material is paper, some limiting assumptions are typically done. On the other hand, the transverse behaviour of such panels was the object of several papers.

The already cited work by Briassoulis [17] can be extended to this kind of corrugation, thanks to its simplicity, even though results could be used only to have a rough estimation of the order of magnitude of the parameters, as it will be proved in the following sections. Indeed, also Liew et al. [31] used the formulation by Briassoulis to have an approximated solution of the in-plane properties, while for the out-of-plane parameters the same results as for a trapezoidal corrugation were used by them.

Isaksson et al. [32] deeply investigated the out-of-plane parameters of a sinusoidally corrugated lamina and the E_y parameter, while for the in-plane shear modulus G_{xy} the Baum's approximation [33] is used. The Baum's approximation is based on measurements on several paperboard panels and from that data, an empirical formula was obtained as a function of the two in-plane Young's moduli. Results of the formulation proposed by Isaksson et al. [32] are listed in Eqs. 2.23, where the parameters are given for an infinitesimal arc of the corrugated shape ds, whose dimensions along x and z are dh and dx respectively.

$$
\begin{aligned}
E_y &= \frac{2Et_c}{2p}\frac{\mathrm{d}s}{\mathrm{d}h} \\
G_{xy} &= 0.387\sqrt{E_xE_y} \\
G_{xz} &= \frac{16ELp^2t_c^3}{\{4L^2t_c^2 + 3*H_0^2[4x+2p(\cos(\frac{\pi x}{p})-1)]^2\}[4p^2+2\pi H^2\sin(\frac{\pi x}{p})]}\frac{\mathrm{d}h}{\mathrm{d}x} \\
G_{yz} &= \frac{2t_cG}{2p}\frac{\mathrm{d}h}{\mathrm{d}s}
\end{aligned}
\tag{2.23}
$$

Other two papers that cite the Baum's approximation are those by Aboura et al. [34] and Talbi et al. [35], the latter being an improvement of the formulation given in the first one. The properties of the sole core are given as a function of the inclination angle of the corrugation $\theta(x)$, as listed in Eqs. 2.24. Please note that properties are given considering the infinitesimal arc of length dx along x. In the paper, an orthotropic constituent material is considered, while here equations are reduced considering an isotropic constituent material.

$$
\begin{aligned}
E_x &= \left(\frac{c^4+s^4}{E} + s^2c^2\left(\frac{1}{G} - \frac{2\nu}{E}\right)\right)^{-1} \\
E_y &= E \\
\nu_{yx} &= \nu \\
G_{xy} &= G \\
G_{xz} &= \left[4s^2c^2\left(\frac{2(1-\nu)}{E}\right) + \frac{(c^2-s^2)^2}{G}\right]^{-1} \\
G_{yz} &= G
\end{aligned}
\tag{2.24}
$$

where $c = \cos(\theta)$ and $s = \sin(\theta)$. Finally, Nordstrand et al. [36] studied the out-of-plane behaviour of corrugated cardboard in shear, G_{xz} and G_{yz} for the complete panel, but the rather complex formulation is not reported here, even though it will be used as comparison term in the following sections.

2.3 Optimization methods

2.3.1 Generalities

In general, optimization techniques are used to find a set of design parameters, $\boldsymbol{x} = \{x_1, x_2, ..., x_n\}$, that results in the optimal value of the Objective Function (OF), $g(\boldsymbol{x})$. In a simple case this might be the minimization or maximization of some system characteristic that is dependent on $\boldsymbol{x}$. In a more advanced formulation the objective function, $g(\boldsymbol{x})$, to be minimized or maximized, might be subject to constraints in the form of equality constraints, $G_i(\boldsymbol{x}) = 0$, inequality constraints, $G_i(\boldsymbol{x}) \leq 0$, and/or parameter bounds, $\boldsymbol{x}_l$, $\boldsymbol{x}_u$. Therefore, a general problem description is stated as

$$\min g(\boldsymbol{x}) \tag{2.25}$$

subject to

$$
\begin{aligned}
&G_i(\boldsymbol{x}) = 0 \quad i = 1, ..., m_e \\
&G_i(\boldsymbol{x}) \leq 0 \quad i = m_e + 1, ..., m \\
&\boldsymbol{x}_l \leq \boldsymbol{x} \leq \boldsymbol{x}_u
\end{aligned}
\tag{2.26}
$$

An efficient and accurate solution to this problem depends not only on the size of the problem in terms of number of constraints and design variables, but also on the characteristics of the objective function and constraints. When the constraints and the OF are linear or quadratic functions of the design variables, reliable solution procedures are readily available. More difficult to solve is the Nonlinear Programming (NP) problem in which the objective function and constraints can be nonlinear functions of the design variables. There are different solution approaches to the optimization process: heuristic approach, graphical method, experimental techniques and so on. They can be distinguished in two major categories.

Gradient-based (GB) methods, which have the following common features:

- the existence of continuous first – and possibly higher order – derivatives of the functions involved is required;
- compared to non-gradient-based methods, generally a much smaller number of design cycles is required to converge to an optimum;
- only convergence to a local minimum is guaranteed.

Non-GB methods:

- only OF evaluations are used to find the optimum point. Gradient and Hessian are not needed;
- the global minimum may be found, but a large number of design cycles is required;
- integer variables can be handled;
- OFs that do not have smooth first or second derivatives can be included.

It is not always straightforward to select the best technique for a given problem, as there is no single method or algorithm that works best on all or even a broad class of problems. In order to choose the best method for a given problem, one must first understand the type of design space that is being searched (type of the responses and number, type and range of the design variables). A design space can be characterized primarily in terms of its smoothness: smooth, rugged or discontinuous. In a smooth design space it is possible to calculate design sensitivity gradients, while solution gradients cannot be directly computed in rugged or discontinuous design spaces. In general, even if there are guidelines for the choice, the problem has to be explored rather thoroughly.

2.3.2 Optimization problems for sandwich panels

The problem of finding an optimal design for sandwich panels is being investigated since 1967 in the pioneering studies by Vinson and Shore [37, 38]. In their study, they gave formulas to obtain the minimum weight of corrugated core sandwich panel subjected to uniaxial compression. In particular, the solution of the problem is given as a function of the panel width and length and a function of the face materials, which can be isotropic or orthotropic. The work was further developed in 1986 by Vinson [39] giving the same closed-form analytical solutions for hex-cell and square cell honeycomb core sandwich panels.

One of the first optimization processes solved numerically, i.e. with an algorithm as those introduced in Section 2.3.1, and applied to sandwich panels is reported in [40]. As also mentioned in that paper, numerical optimization was previously possible only in big industries, such as the aircraft industry, due to the need of great computational potentiality. That study is particularly important because it considers a multidisciplinary process, in particular the structural-acoustic optimization, which is the aim of the last part of the present dissertation. Nevertheless, the preliminary nature of that study is obvious, and also admitted by the author, since only the thickness of an isotropic rectangular panel is considered as design variable. It is important noting that the acoustic constraint is chosen as the frequency averaged transmission loss, which is a smoother constraint than the one used in this work. The same authors improved in 1994 [41] that optimization process to account for variable thickness, variable mass distribution, and variable composite material property distributions. Both studies [40, 41] used a GB algorithm.

Another interesting study, which uses Genetic Algorithm instead, was performed by Coello and Christiansen in 2000 [42] on truss-cored sandwich structures. The problem defined in [42] is characterized by a multi-objective nature, although only structural parameters are considered.

One of the main authors in this field is Hutchinson, who has proposed several papers on the optimization of sandwich panels. In 2000 he studied the buckling of sandwich shells with foam cores together with He [43] considering face sheet thickness, core thickness and core density while minimizing the weight of the panels. In 2004 [44], with Xue, he studied three different sandwich panels, i.e. pyramidal truss, square honeycomb and folded plate cores, under impulsive blast loads. A minimization of the weight is also carried out as a preliminary analysis with respect to core and face sheet thickness, core member aspect ratios and relative density. In 2005 the same authors also considered pressure impulse as load condition [45].

An interesting multidisciplinary investigation of different core topologies was carried out by Gu et al. [46] including structural and heat transfer performance of such panels while minimizing their weight. By the same co-author, Lu, in 2004, a multi-ojective and multi-loading optimization is performed on ultra-lightweight truss cores [47]; nevertheless, only structural performances are considered.

Focusing on corrugated core sandwich panels, the literature is poor. Indeed, apart from the two initial works by Vinson and Shore [37, 38], only one other paper was found by Tian and Lu [48]. Nevertheless, as typically done in the literature, only structural constraints are considered, i.e. compression loadings.

The conclusion that can be drawn from this state-of-the-art analysis is that there is a lack of application of multi-disciplinary optimization to corrugated core sandwich panels, even though such structures could have great potentiality in terms of design tailored to predefined requirements.

Chapter 3

Homogenization of corrugated cores

3.1 Introduction

The small thicknesses of the corrugated core sandwich panels, compared to their overall dimensions, affect negatively their modelling, typically made with FE methods, since the simulation of the three-dimensional (3D) geometry of the core requires a large number of FE elements. In order to reduce the number of elements and consequently the computational time, the complex shaped cores are typically represented as a homogeneous orthotropic layer with equivalent mechanical properties. Therefore the mechanical parameters of the material of the equivalent layer must be derived accurately.

As already introduced in Section 2.2 and highlighted by several authors, the main drawback of analytical techniques for deriving equivalent parameters is their lack of generality, which implies a strong restriction in their applicability to real cases. Indeed, the core geometry strongly affects the mechanical properties of corrugated cores and thus those of the equivalent material. This is the main motivation that pushed researchers to use FE based techniques. Nevertheless, FE model creation and simulation setup are phases that can be extremely time consuming and not easily automatized.

In this regard, the aim of this chapter is to present an innovative analytical formulation for the determination of equivalent parameters for corrugated core sandwich structures.

As indicated in the state-of-the-art analysis, Chapter 2, in the majority of the corrugated shapes studied in previous works in the literature, only the in-plane behaviour of the equivalent layer is modelled, using a Love-Kirchhoff plate theory [49] or an Euler-Bernoulli theory [50, 51] in case of beams. Nevertheless, the out-of-plane properties are very important for this kind of panels, especially when analyzing their acoustic or dynamic behaviour. Therefore a general analytical technique cannot neglect the shear deformations through-the-thickness of a plate, i.e. at least the first-order shear effects must be taken into account (Reissner-Mindlin shell theory [52, 53] or Timoshenko beam theory [54]).

In light of this consideration, the proposed analytical formulation models the equivalent layer as an orthotropic material, whose constitutive relation can be written in compliance form as shown in Eq. 3.1.

$$\begin{Bmatrix} \epsilon_{xx} \\ \epsilon_{yy} \\ \epsilon_{zz} \\ \epsilon_{yz} \\ \epsilon_{zx} \\ \epsilon_{xy} \end{Bmatrix} = \begin{bmatrix} \frac{1}{E_x} & \frac{-\nu_{yx}}{E_y} & \frac{-\nu_{zx}}{E_z} & 0 & 0 & 0 \\ \frac{-\nu_{xy}}{E_x} & \frac{1}{E_y} & \frac{-\nu_{zy}}{E_z} & 0 & 0 & 0 \\ \frac{-\nu_{xz}}{E_z} & \frac{-\nu_{yz}}{E_y} & \frac{1}{E_z} & 0 & 0 & 0 \\ 0 & 0 & 0 & \frac{1}{2G_{yz}} & 0 & 0 \\ 0 & 0 & 0 & 0 & \frac{1}{2G_{zx}} & 0 \\ 0 & 0 & 0 & 0 & 0 & \frac{1}{2G_{xy}} \end{bmatrix} \begin{Bmatrix} \sigma_{xx} \\ \sigma_{yy} \\ \sigma_{zz} \\ \sigma_{yz} \\ \sigma_{zx} \\ \sigma_{xy} \end{Bmatrix} \tag{3.1}$$

Considering a Reissner-Mindlin plate representation of the material, the plate stress hypothesis is assumed, which implies the σ_{zz} stress to be neglected. Therefore, the matrix $\boldsymbol{C}$ in that case is reduced, erasing the third column and the third row. Considering this reduced matrix and imposing it to be symmetric implies that six parameters are needed to characterize the homogenized layer for a plate representation. In addition, the equivalent density is needed for dynamic purposes. The developed formulation applies only to the core, which is the focus of this work. Nevertheless, to compare with other authors the equivalent parameters for the complete structure, thus including the two faces, they are obtained as shown in Section 2.1.2. This choice is an approximation commonly done in the literature, that assumes perfect bonding between the core and the faces.

The accuracy of the proposed method is then validated by means of comparisons with a properly developed FE-based technique. Moreover, an extensive comparison with results from previous papers is given. Finally, an extension of the proposed formulation for a solid representation of the equivalent layer is given.

This chapter is organized as follows. The developed analytical formulation is first described in Section 3.2 for an equivalent plate representation and it is then extended to a solid representation in Section 3.4. In Section 3.5 the general formulation is validated by means of FE simulations, while comparisons with previous works is shown in Section 3.6 for the most common corrugation geometries in the literature. Finally, a discussion of results is given in Section 3.7.

3.2 Analytical formulation

Consider a generic shaped corrugated core sandwich panel with unit width $b = 1$ (*y-direction*) and set the reference system as in Figure 3.1. The corrugation can be considered periodic with period P_0 and height H_0. The corrugated lamina is supposed to have constant thickness t_c (Figure 3.2). In a general case, as that in Figure 3.2, the highest point of the core sample is not necessarily in correspondence of the half-period. Therefore, the curve is split in two parts having length along x p_1 and p_2 respectively.

As already introduced, one of the key points which makes the proposed method very appealing is its applicability to every corrugation geometry. This is done by means of a Fourier series representation of the corrugated profile. The non-symmetry of the corrugation would lead to a Fourier series in sines and cosines. To avoid this and have a simpler formulation, the two parts of the curve are processed separately and then their contributions are combined together.

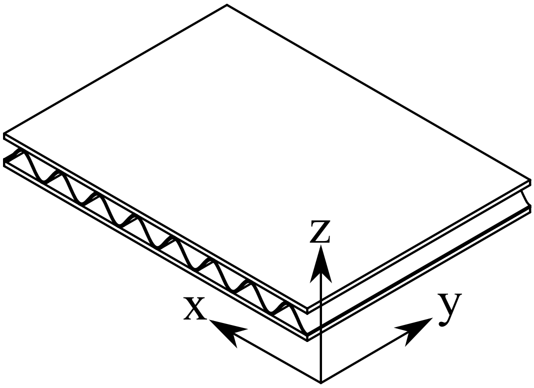

Figure 3.1: Global system of reference definition.

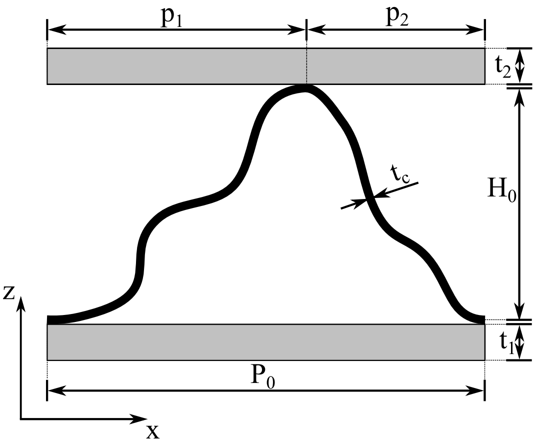

Figure 3.2: Sandwich panel with generic corrugated core shape: relevant parameters.

Therefore, the curves with periods $2p_1$ and $2p_2$ – obtained mirroring the two parts of the corrugation shape as shown in Figure 3.3 – are considered separately. This allows them to be represented in Fourier cosine series since they are even functions.

Each curve can be represented by the function

$$f_i(x) = a_{0i} + \sum_{k=1}^{n} a_{ki} \cdot \cos\left(\frac{k\pi x}{p_i}\right) \tag{3.2}$$

being n the number of terms used in the series, p_i is the half-period and a_{ki} are the Fourier coefficients for the *i-th* curve under examination ($i = 1, 2$). In the following sections, when numerical results are proposed, the number of terms has been chosen so that the excluded terms have a coefficient a_{ki} lower than 10^{-6}.

Another necessary function that will be used is the first derivative of the shape

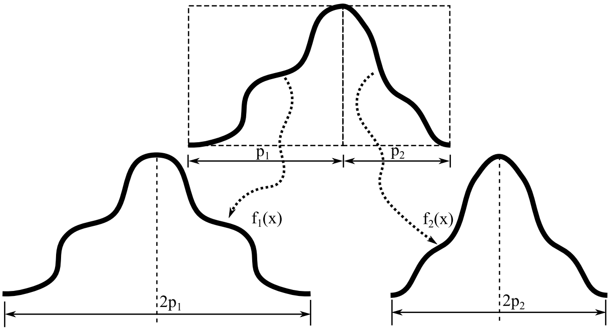

Figure 3.3: Mirroring process to obtain the two periodic curves.

function:

$$f_i'(x) = -\sum_{k=1}^{n} a_{ki} \frac{k\pi}{p_i} \cdot \sin\left(\frac{k\pi x}{p_i}\right) \tag{3.3}$$

In the following, each mechanical parameter of the equivalent formulation is described starting from the previous statements. Moreover, since supposing a unit width would limit the application of this formulation to sandwich beams, equivalent parameters which are likely to depend on the width of the specimen are adapted to represent also plate-like sandwich structures.

3.2.1 Transverse shear modulus G_{xz}

The first parameter of the equivalent material is the transverse shear modulus in the *xz-plane*. To determine the equivalent shear modulus, the horizontal displacement δ_H of the upper end due to a horizontal force H has to be determined. Other displacements and rotations of the upper end are denied to reproduce pure shear deformation, as schematically represented in Figure 3.4. Since the lower ends have both displacements and rotations fixed, the periodic nature of the corrugation is implicitly included in this model.

Consider separately the two parts of the corrugation with half-period p_1 and p_2. For each part, clamp the structures in correspondence of its lowest point (Figure 3.5) and apply a force H at the free end. In addition, a dummy moment M_0 and a vertical force V are applied to include proper boundary conditions (BCs), i.e. vertical displacement δ_V and rotation δ_{M_0} equal to zero.

The inner forces at a generic point x, as illustrated in Figure 3.5, are:

$$M = Hf_i(x) + Vx - M_0 \tag{3.4}$$

$$N = H\cos\varphi - V\sin\varphi \tag{3.5}$$

$$T = H\sin\varphi + V\cos\varphi \tag{3.6}$$

where φ is the angle between the tangent to $f(x)$ and the *x-axis*. The values of

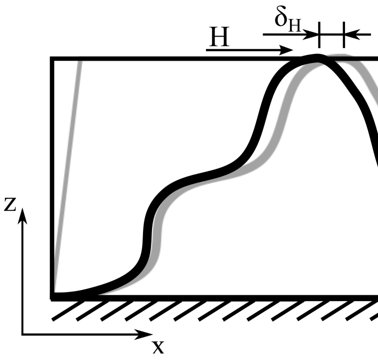

Figure 3.4: Deformation in pure shear conditions for the G_{xz} parameter.

$\cos\varphi$ and $\sin\varphi$ are obtained as

$$\begin{aligned}\cos\varphi &= \frac{1}{\sqrt{1+f_i'(x)^2}}\\ \sin\varphi &= \frac{f_i'(x)}{\sqrt{1+f_i'(x)^2}}\end{aligned} \tag{3.7}$$

where $f_i'(x)$ is defined as in Eq. 3.3.

The partial derivatives of the inner forces with respect to the applied loads can be computed as:

$$\begin{aligned}\frac{\partial M}{\partial H} &= f_i(x) & \frac{\partial M}{\partial V} &= x & \frac{\partial M}{\partial M_0} &= -1\\ \frac{\partial N}{\partial H} &= \cos\varphi & \frac{\partial N}{\partial V} &= -\sin\varphi & \frac{\partial N}{\partial M_0} &= 0\\ \frac{\partial T}{\partial H} &= \sin\varphi & \frac{\partial T}{\partial V} &= \cos\varphi & \frac{\partial T}{\partial M_0} &= 0\end{aligned} \tag{3.8}$$

Applying the Castigliano's theorem [27] allows obtaining the following equations,

$$\delta_{H_i} = \int_0^{p_i} \left(\frac{M\frac{\partial M}{\partial H}}{EI} + \frac{N\frac{\partial N}{\partial H}}{EA} + \frac{T\frac{\partial T}{\partial H}}{GA'} \right) \frac{\mathrm{d}x}{\cos\varphi} \tag{3.9}$$

$$\delta_{V_i} = \int_0^{p_i} \left(\frac{M\frac{\partial M}{\partial V}}{EI} + \frac{N\frac{\partial N}{\partial V}}{EA} + \frac{T\frac{\partial T}{\partial V}}{GA'} \right) \frac{\mathrm{d}x}{\cos\varphi} \tag{3.10}$$

$$\delta_{M_{0i}} = \int_0^{p_i} \left(\frac{M\frac{\partial M}{\partial M_0}}{EI} + \frac{N\frac{\partial N}{\partial M_0}}{EA} + \frac{T\frac{\partial T}{\partial M_0}}{GA'} \right) \frac{\mathrm{d}x}{\cos\varphi} \tag{3.11}$$

where $\frac{\mathrm{d}x}{\cos\varphi}$ is introduced to integrate along x instead of the length of the sine curve. The last equations result in the system:

$$\begin{bmatrix} \delta_{H_i} \\ \delta_{V_i} \\ \delta_{M_{0i}} \end{bmatrix} = \frac{1}{EA} \begin{bmatrix} C_{1,1} & C_{1,2} & C_{1,3} \\ & C_{2,2} & C_{2,3} \\ sym. & & C_{3,3} \end{bmatrix} \begin{bmatrix} H \\ V \\ M_0 \end{bmatrix} \tag{3.12}$$

being E the Young's modulus of the constituent material of the corrugation and A the area of the corrugated lamina cross-section, which is equal to the thickness of the lamina t_c, since the investigated specimen has unit width.

The elements of the matrix in Eq. 3.12 can be written as

$$\begin{aligned} C_{1,1} &= \frac{12}{t^2} F_1 + F_2 + \frac{2(1+\nu)}{\kappa} F_3 \\ C_{1,2} &= \frac{12}{t^2} F_4 + F_5 + \frac{2(1+\nu)}{\kappa} F_6 \\ C_{1,3} &= \frac{12}{t^2} F_7 \\ C_{2,2} &= \frac{12}{t^2} F_8 + F_9 + \frac{2(1+\nu)}{\kappa} F_{10} \\ C_{2,3} &= \frac{12}{t^2} F_{11} \\ C_{3,3} &= \frac{12}{t^2} F_{12} \end{aligned} \tag{3.13}$$

where κ is the shear factor of the corrugated lamina cross section ($\kappa = 5/6$) and the terms F_j are the integrals involved which depend on the approximated Fourier cosine series and its derivative – defined in Eqs. 3.2 and 3.3 – as listed in Eqs. 3.14.

$$
\begin{aligned}
F_1 &= \int_0^{p_i} \frac{(\partial M/\partial H)^2}{\cos\varphi}\,\mathrm{d}x \\
F_2 &= \int_0^{p_i} \frac{(\partial N/\partial H)^2}{\cos\varphi}\,\mathrm{d}x \\
F_3 &= \int_0^{p_i} \frac{(\partial T/\partial H)^2}{\cos\varphi}\,\mathrm{d}x \\
F_4 &= \int_0^{p_i} \frac{(\partial M/\partial H)(\partial M/\partial V)}{\cos\varphi}\,\mathrm{d}x \\
F_5 &= \int_0^{p_i} \frac{(\partial N/\partial H)(\partial N/\partial V)}{\cos\varphi}\,\mathrm{d}x \\
F_6 &= \int_0^{p_i} \frac{(\partial T/\partial H)(\partial T/\partial V)}{\cos\varphi}\,\mathrm{d}x \\
F_7 &= \int_0^{p_i} \frac{(\partial M/\partial H)(\partial M/\partial M_0)}{\cos\varphi}\,\mathrm{d}x \\
F_8 &= \int_0^{p_i} \frac{(\partial M/\partial V)^2}{\cos\varphi}\,\mathrm{d}x \\
F_9 &= \int_0^{p_i} \frac{(\partial N/\partial V)^2}{\cos\varphi}\,\mathrm{d}x \\
F_{10} &= \int_0^{p_i} \frac{(\partial T/\partial V)^2}{\cos\varphi}\,\mathrm{d}x \\
F_{11} &= \int_0^{p_i} \frac{(\partial M/\partial V)(\partial M/\partial M_0)}{\cos\varphi}\,\mathrm{d}x \\
F_{12} &= \int_0^{p_i} \frac{(\partial M/\partial M_0)^2}{\cos\varphi}\,\mathrm{d}x
\end{aligned}
\tag{3.14}
$$

where p_i is the half period of the *i-th* part ($i = 1, 2$) and the partial derivatives are those in Eq. 3.8.

Finally, applying the mentioned BCs and considering $H = 1$, the horizontal displacement for the *i-th* part can be found as

$$\delta_{H_i} = \frac{1}{EA}\,\frac{\det(C)}{\det(C_{red})} \tag{3.15}$$

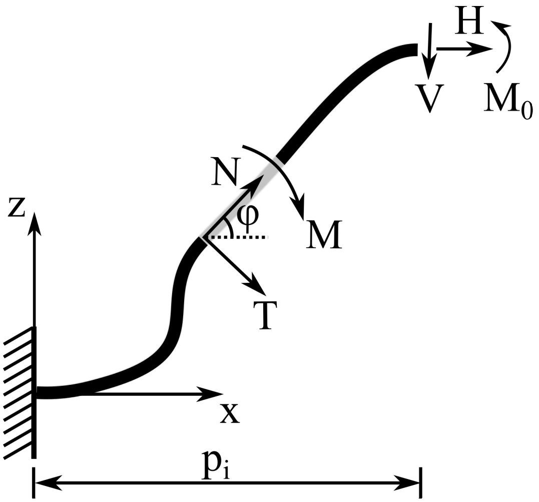

Figure 3.5: Loads and forces acting on the centre line of the corrugation: nomenclature.

where C_{red} is defined as follows:

$$[C_{red}] = \begin{bmatrix} C_{2,2} & C_{2,3} \\ C_{2,3} & C_{3,3} \end{bmatrix} \tag{3.16}$$

Once the horizontal displacement for the two parts, δ_{H_1} and δ_{H_2} respectively, are calculated at the free edge, the total displacement δ_H must be found to obtain the equivalent shear modulus of the general corrugated lamina.

Considering that the two parts must have the same displacement at the free end under a common force H, they can be handled as two springs in parallel. The effective spring constant is then the sum of the spring stiffnesses of the two parts, which are the inverse of the horizontal displacements since the applied forces are unitary:

$$K_{eq} = K_1 + K_2 = \frac{1}{\delta_{H_1}} + \frac{1}{\delta_{H_2}} = \frac{1}{\delta_H} \tag{3.17}$$

Finally, the shear modulus G_{xz} of the equivalent material is

$$G_{xz} = \frac{\tau_{xz}}{\gamma_{xz}} = \frac{F_x}{A_{xy}} \Big/ \frac{\delta_x}{l_z} = \frac{H_0}{P_0} \cdot \frac{1}{\delta_H} \tag{3.18}$$

where δ_H is again obtained as the inverse of the spring constant K_{eq}.

The explained theory uses a beam representation of the corrugated core. In order to find a parameter representative of a corrugated plate, it is sufficient to substitute the Young's modulus of the constituent material E with its plate modulus $E/(1-\nu^2)$.

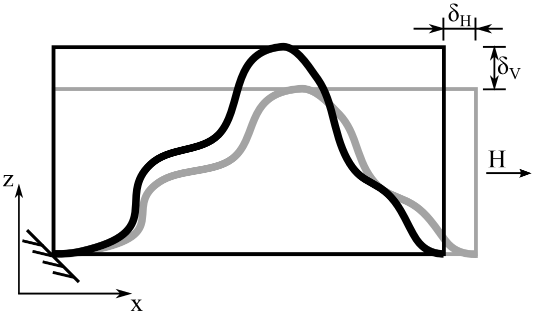

Figure 3.6: Deformation in tensile test for the E_x parameter.

3.2.2 Elastic modulus in x-direction E_x

The second parameter of the equivalent material is the modulus of elasticity in the longitudinal direction, also called machine direction (MD). Following the same procedure seen for G_{xz}, for the computation of E_x the two parts of the corrugated lamina are subjected to a unit horizontal force H and the related horizontal displacements δ_{H_i} are derived for both the parts.

The main difference between E_x and G_{xz} determination is that in this case no BC on the vertical displacement has to be applied to reproduce the tensile testing (Figure 3.6), since contraction in the *z-direction* is allowed during such testing. Nevertheless rotations are still not permitted at the free end assuring the periodicity of the corrugation to be included in the model. Since no BC on the vertical displacement is needed, the fictitious vertical force V can then be neglected. This implies that the forces acting at the generic point x in Figure 3.5 can be reduced to

$$M = Hf_i(x) - M_0 \tag{3.19}$$

$$N = H\cos\varphi \tag{3.20}$$

$$T = H\sin\varphi \tag{3.21}$$

and the partial derivatives become

$$\begin{aligned} \frac{\partial M}{\partial H} &= f_i(x) & \qquad \frac{\partial M}{\partial M_0} &= -1 \\ \frac{\partial N}{\partial H} &= cos\varphi & \qquad \frac{\partial N}{\partial M_0} &= 0 \\ \frac{\partial T}{\partial H} &= sin\varphi & \qquad \frac{\partial T}{\partial M_0} &= 0 \end{aligned} \tag{3.22}$$

Therefore, the system of equations can be obtained from Eq. 3.12 removing the second equation and the second column of the matrix C, giving

$$\begin{bmatrix} \delta_{H_i} \\ \delta_{M_0} \end{bmatrix} = \frac{1}{EA} \begin{bmatrix} C_{1,1} & C_{1,3} \\ C_{3,1} & C_{3,3} \end{bmatrix} \begin{bmatrix} H \\ M_0 \end{bmatrix} \tag{3.23}$$

where the coefficient are the same as in Eqs. 3.12. Imposing now the BC of $\delta_{M_0} = 0$ and considering unit applied force $H = 1$, δ_{H_i} is obtained as

$$\delta_{H_i} = \frac{1}{EA}\left(C_{1,1} - \frac{C_{1,3}^2}{C_{3,3}}\right) \tag{3.24}$$

The second difference from the G_{xz} determination consists in the combination of the results for the two semi-profiles. For the E_x parameter, once the horizontal displacements δ_{H_i} are found, it is sufficient to consider that the two parts behave like two springs in series. Therefore the total displacement δ_H is simply the sum of the two "partial" displacements δ_{H_1} and δ_{H_2}.

Finally, the Young's modulus E_x of the equivalent material is

$$E_x = \frac{\sigma_x}{\varepsilon_x} = \frac{F_x}{A_{yz}} \bigg/ \frac{\delta_x}{l_x} = \frac{P_0}{H_0} \cdot \frac{1}{\delta_H} \tag{3.25}$$

As already explained for the G_{xz} parameter, the theory assumes a corrugated beam. Also in this case, in order to have the parameter for a corrugated plate, it is sufficient to replace E with $E/(1 - \nu^2)$ in the system of equations.

It is worth noting that the supposed condition of allowed vertical displacement is valid only if the corrugation is symmetric. Indeed, an asymmetric profile may lead to different contractions in the *z-direction* for the two parts, which may result in the presence of shear forces at the upper edge to avoid discontinuity between the two parts. Nevertheless, typically the corrugations are symmetric and when they are not, the difference in the vertical displacements of the upper edges is very limited, thus allowing the assumption made to be considered a good approximation.

3.2.3 Elastic modulus in y-direction E_y

The third parameter is the modulus of elasticity in the lateral direction, or cross direction (CD). It can be computed scaling the Young's modulus of the constituent material E to the ratio between the actual section area of the corrugated core sheet A_y and the section area of the equivalent material A_{eq_y}, see Eq. 3.26.

When stretched in the *y-direction*, the corrugation contracts in the *x-direction* according to the constituent material Poisson's ratio. Therefore, the cross sections at the peaks and valleys of the corrugation remain parallel to the *yz-plane*, thus the periodicity of the geometry is implicitly accounted for.

$$E_y = E\frac{A_y}{A_{eq_y}} = E\frac{t_c(l_1 + l_2)}{H_0 P_0} \tag{3.26}$$

where l_1 and l_2 are the lengths of half a period of the two curves composing the corrugation. Each length can be computed as:

$$l_i = \int_0^{p_i} \sqrt{1 + |f_i'(x)|^2}\, \mathrm{d}x \tag{3.27}$$

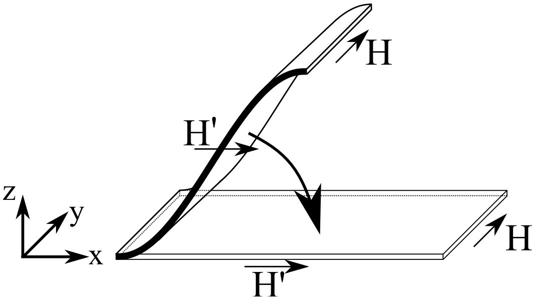

Figure 3.7: Core approximation for G_{yz} and G_{xy} calculation.

3.2.4 In-plane Poisson's ratio ν_{xy}

The in-plane Poisson's ratio ν_{xy} is obtained as

$$\nu_{xy} = \nu_{yx} \frac{E_x}{E_y} \tag{3.28}$$

assuming the other Poisson's ratio in the $xy - plane$ (ν_{yx}) to be equal to that of the constituent material, as typically done in the literature [17, 55].

3.2.5 Transverse shear modulus in yz-plane G_{yz}

The transverse shear modulus in the *yz-plane* G_{yz} can be derived for each of the two halves based on some considerations. The two corrugated curves representing the core are simplified. In the sample domain of half a period, the two parts of the core are stretched to a flattened panel with length l_1 and l_2 respectively, which are the lengths of half a period of the two curves composing the corrugation as in Section 3.2.3. The approximated geometry can be seen for a sinusoidal corrugation in Figure 3.7. This corresponds to create a local curved system of reference along the centre-line of the core sheet and integrate along that local coordinate. Therefore, this assumption does not introduce errors to the analytical modelling. Moreover, since both lower ends are supposed to be clamped, the investigated cell can also be part of a periodic structure.

The panel can then be considered a straight beam/panel with rectangular section and the displacement in *y-direction* due to a force H in the same direction can be computed as

$$\delta_{zy_{re}} = \frac{H\, l_i}{\frac{5}{6} G\, A} \tag{3.29}$$

where H is the force applied, G the shear modulus of the constituent material and A the area of the corrugated lamina cross-section, which is equal to the thickness of the lamina t_c.

The shear deformation of the volume occupied by the equivalent material in half a period of the corrugation, $\delta_{zy_{eq}}$, under the same conditions is

$$\delta_{zy_{eq}} = \frac{H\, H_0}{\frac{5}{6} G_{yz_i}\, p_i} \tag{3.30}$$

Imposing the two displacements $\delta_{zy_{re}}$ and $\delta_{zy_{eq}}$ to be equal for each of the two parts, the value of G_{yz_i} can be obtained as

$$G_{yz_i} = G\frac{H_0\, t_c}{p_i l_i} \tag{3.31}$$

As already assumed for the G_{xz} parameter, also in this case the two parts are supposed to work as two springs in parallel, since they must have the same displacement of the upper end. Skipping the step to obtain the spring stiffnesses, we can directly write the equivalent shear modulus as

$$G_{yz} = G_{yz_1} * V_1 + G_{yz_2} * V_2 \tag{3.32}$$

where V_i is the volume fraction occupied by the equivalent material for the two parts:

$$V_i = p_i/(p_1 + p_2) \tag{3.33}$$

Substituting Eqs. 3.31 and 3.33 in Eq. 3.32 gives

$$G_{yz} = G\frac{H_0 t_c}{P_0}\left(\frac{1}{l_1} + \frac{1}{l_2}\right) \tag{3.34}$$

3.2.6 In-plane shear modulus G_{xy}

The in-plane shear modulus G_{xy} is computed with the same assumptions made for the G_{yz} parameter. The only difference is that now the force, H' in Figure 3.7, is acting along the *x-direction.* The condition of pure shear deformation implicitly considers the displacement in the *x-direction* constant in the cross sections perpendicular to the *y-axis* and no other displacements or rotations are allowed. Therefore, the periodicity of the corrugation has no influence on the results.

With the assumption in Section 3.2.5, the cross-section perpendicular to the *y-axis* is approximated to a rectangle. Therefore, the shear factor can be assumed as 5/6 and the shear deformations computed for the approximated section $\delta_{xy_{re}}$ and for the equivalent sample section $\delta_{xy_{eq}}$ – for each of the two parts – as:

$$\delta_{xy_{re}} = \frac{H'\, b}{\frac{5}{6} G\, t_c l'} \tag{3.35}$$

$$\delta_{xy_{eq}} = \frac{H'\, b}{\frac{5}{6} G_{xy_i}\, H_0 p_i} \tag{3.36}$$

being b the width of the specimen.

Therefore, imposing $\delta_{xy_{re}}$ and $\delta_{xy_{eq}}$ to be equal, the equivalent shear modulus G_{xy_i} is obtained as

$$G_{xy_i} = G\frac{t_c\, l_i}{H_0 p_i} \tag{3.37}$$

Considering a parallel spring behaviour of the two parts and the deriving relation for the equivalent stiffness, the G_{xy} parameter is obtained as

$$G_{xy} = G\frac{(l_1 + l_2)t_c}{H_0 P_0} \tag{3.38}$$

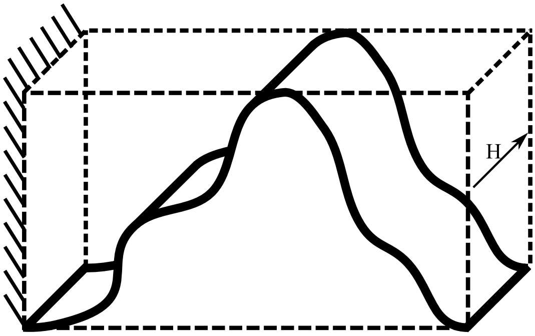

Figure 3.8: Shear scheme for the G_{yx} parameter.

3.2.7 Mass density ρ_{eq}

The density of the equivalent material is computed by scaling the density of the constituent material ρ proportionally to the occupied equivalent volume.

Due to the constant profile in *y-direction*, only the cross-sections can be involved, thus

$$\rho_{eq} = \rho \frac{t_c l'}{H_0 P_0} \tag{3.39}$$

3.3 Additional shear moduli

Due to the corrugated shape of the core lamina, a different behaviour is expected in the $x_1 x_2$-*plane* computing the shear moduli forcing the structure along the x_1 or the x_2 direction, thus $G_{xy} \neq G_{yx}$, and the same in the other planes, thus $G_{xz} \neq G_{zx}$ and $G_{zy} \neq G_{yz}$. Therefore, to have a full description of the core behaviour, the three "complementary" moduli are determined in the following and are then compared and discussed in Section 3.6. Typically, previous authors considered only one of them, as it is shown in Section 3.6. Nevertheless, no explanation on the choice of the computed value is given in the literature. Moreover, a more detailed investigation would be required on the choice of the shear modulus to be used for each main plane to properly represent the behaviour of the sandwich structure under different load conditions.

3.3.1 In-plane shear modulus G_{yx}

In this section the calculation of the G_{yx} parameter, associated with a loading along y, is computed. To obtain this parameter, a force H is applied in the *y-direction* at the end of the period of the corrugation while clamping the other end as shown in Figure 3.8. The displacement of the free end in the *y-direction* can then be found, in pure shear conditions, as

$$\delta_{yx_{re}} = \frac{H\, l'}{\frac{5}{6} G\, t_c b} \tag{3.40}$$

assuming that the curved shape does not affect the shear behaviour, which coincides with considering it as a straight beam with length along x equal to $l' = l_1 + l_2$ as defined in Eq. 3.27. Since only displacement in the *y-direction* is allowed for the free end, the model can be considered representative also of a periodic structure.

The shear deformation of the equivalent volume, i.e. the volume occupied by the equivalent material in the period P_0, can be derived as:

$$\delta_{yx_{eq}} = \frac{H\,P_0}{\frac{5}{6} G\,H_0 b} \tag{3.41}$$

Imposing these two displacements to be equal, the value of the G_{yx} parameter can be computed as

$$G_{yx} = G \frac{t_c}{H_0} \frac{P_0}{l'} \tag{3.42}$$

3.3.2 Transverse shear modulus in xz-plane G_{zx}

According to the convention used, the G_{zx} parameter is computed applying to the upper end of the two parts of the corrugation a force V along the *z-direction* and determining the displacement in the same direction. Other displacements and rotations of the upper edge are denied, while the lower edges are fully clamped. Once again, the periodic nature of the corrugation is implicitly considered by the imposed BCs.

Considering separately the two parts of the corrugation with half-period p_1 and p_2, with reference to Figure 3.5, the vertical force V is imposed to be unitary, while a dummy force H and dummy moment M_0 are included to impose the mentioned BCs, i.e. horizontal displacement δ_H and rotation δ_{M_0} equal to zero.

The same system of equations as in Section 3.2.1 can be obtained and the vertical displacement can be computed as

$$\delta_{V_i} = \frac{1}{EA} \frac{\det(C)}{\det(C^1_{red})} \tag{3.43}$$

where C^1_{red} is defined as follows:

$$[C^1_{red}] = \begin{bmatrix} C_{1,1} & C_{1,3} \\ C_{3,1} & C_{3,3} \end{bmatrix} \tag{3.44}$$

The total shear behaviour of a complete period P_0 can be seen as the combination of the two parts, which behave in this case, as two springs in series.

Once the vertical displacement for the two parts, δ_{V_1} and δ_{V_2} respectively, are calculated at the free edge, the total displacement δ_V is found as the sum of those values. Finally, the shear modulus G_{zx} of the equivalent material is

$$G_{zx} = \frac{\tau_{zx}}{\gamma_{zx}} = \frac{F_z}{A_{zy}} \bigg/ \frac{\delta_z}{l_x} = \frac{P_0}{H_0} \cdot \frac{1}{\delta_V} \tag{3.45}$$

As already done for other parameters, in order to have a parameter representative of a plate situation rather than a beam structure, the Young's modulus in Eq. 3.43 should be replaced by the plate modulus $E/(1-\nu^2)$.

3.3.3 Transverse shear modulus in yz-plane G_{zy}

The G_{zy} parameter can be found applying a force V along z in the *xz-plane* and calculating the deriving displacement. The procedure used is similar to the one shown for G_{xy}.

The specimen is considered as a cantilever beam of length b and subjected to pure shear deformations. The corrugated curve represents therefore the cross section of such beam and it is approximated as in Section 3.2.5 and 3.2.6 to a rectangular section. Therefore, the same relations can be found as for the G_{xy} parameter and the following relation is determined:

$$G_{zy} = G_{xy} \tag{3.46}$$

3.4 Additional parameters for a solid representation

As already explained, the parameters given in Section 3.2 are for a plate representation of the core. Nevertheless, in some cases it can be necessary to have a solid representation of the homogeneous layer. This is particularly true when effects through the thickness of the panel cannot be neglected. Therefore, to have a complete description of the equivalent material, in the following, the additional parameters needed are derived. These parameters are those shown in the third column and row of Eq. 3.1.

3.4.1 Elastic modulus in z-direction E_z

The Young's modulus in the *z-direction* can be found starting from the same system of equations of Section 3.2.1, Eq. 3.12. To reproduce a tensile condition in the through-thickness direction, it is necessary to apply a vertical force V and impose $\delta_{M_0} = 0$, while no BCs are needed on the horizontal direction, i.e. contraction along x is permitted. The vertical displacement can then be found as

$$\delta_{V_i} = \frac{1}{EA}\left(C_{2,2} - \frac{C_{2,3}^2}{C_{3,3}}\right) \tag{3.47}$$

To combine the contribution of the two parts, a parallel spring behaviour is considered as in Eq. 3.17, therefore

$$K_{eq} = K_1 + K_2 = \frac{1}{\delta_{V_1}} + \frac{1}{\delta_{V_2}} = \frac{1}{\delta_V} \tag{3.48}$$

Finally, the Young's modulus in the *z-direction* can be determined as:

$$E_z = \frac{\sigma_z}{\varepsilon_z} = \frac{F_z}{A_{xy}}\bigg/\frac{\delta_z}{l_z} = \frac{H_0}{P_0}\cdot\frac{1}{\delta_V} \tag{3.49}$$

Once again, a beam representation of the corrugated core is used. In order to find a parameter representative of a corrugated plate, the same substitution in the Young's modulus is needed.

3.4.2 Poisson's ratio in the *xz-plane* ν_{xz}

The Poisson's ratio ν_{xz} is the ratio of the strain along *z-direction* and the strain along *x-direction* for uniaxial loadings in *x-direction.*

Results for the E_x determination can be used to find the strain along the *x-direction* as

$$\varepsilon_x = \frac{\delta_x}{l_x} = \frac{\delta_H}{P_0} \tag{3.50}$$

while for the strain along z, ε_z, the following procedure can be followed.

Considering the system of equations for the G_{xz} parameter, Eq. 3.12, the same assumptions done for the E_x parameter are done, but a dummy load V is included and set to zero to determine the vertical displacement δ_{V_i} for each of the two parts. Once the system is solved as in Section 3.2.2, the vertical displacements can be found as:

$$\delta_{V_i} = \frac{1}{EA}\left(C_{2,1} - \frac{C_{2,3}C_{3,1}}{C_{3,3}}\right) \tag{3.51}$$

In the case of general corrugation, the δ_{V_i} for the two parts are not necessarily equal. Nevertheless, to have a good estimation of the actual vertical contraction, it is sufficient to compute the average of the two values. Then, the strain along z for uniaxial loadings in the *x-direction* is

$$\varepsilon_z = \frac{\delta_z}{l_z} = \frac{\delta_{V_1} + \delta_{V_2}}{2\ H_0} \tag{3.52}$$

Finally, the Poisson's ratio can be calculated as

$$\nu_{xz} = \frac{\varepsilon_z}{\varepsilon_x} \tag{3.53}$$

If the other Poisson's ratio in the *xz-plane* is needed, i.e. ν_{zx}, two equivalent ways are possible. The first one consists in deriving it from ν_{xz}, E_x and E_z as:

$$\nu_{zx} = \nu_{xz}\frac{E_z}{E_x} \tag{3.54}$$

Otherwise, a similar procedure to the one used for ν_{xz} can be implemented, simply considering the definition of this Poisson's ratio: ratio of the strain along *x-direction* and the strain along *z-direction* for uniaxial loadings in *z-direction.* In this case, the results for the E_z computation can be used to find the strain along z, while the strain along x under a vertical force V can be computed, for the two parts, as:

$$\delta_{H_i} = \frac{1}{EA}\left(C_{1,2} - \frac{C_{3,2}C_{1,3}}{C_{3,3}}\right) \tag{3.55}$$

The same approximation to the average value can be done as before, leading to:

$$\varepsilon_x = \frac{\delta_x}{l_x} = \frac{\delta_{H_1} + \delta_{H_2}}{2\ P_0} \tag{3.56}$$

Finally, the ν_{zx} parameter can be determined as

$$\nu_{zx} = \frac{\varepsilon_x}{\varepsilon_z} \tag{3.57}$$

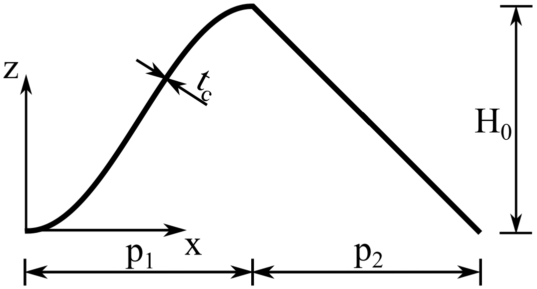

Figure 3.9: Shape and parameters of the validation case.

3.4.3 Poisson's ratio in the *yz-plane* ν_{zy}

To compute the Poisson's ratios in the *yz-plane*, it is sufficient to note that, as already done for the ratios in the *xy-plane*, while applying a load along y, the transverse behaviour is likely to depend only on the material properties, not on the geometry [55]. Therefore, contraction in the *z-direction*, as well as the *x-direction*, follows the constituent material Poisson's ratio, i.e. $\nu_{yz} = \nu$.

As a consequence, the other ratio, ν_{zy}, can be derived as

$$\nu_{zy} = \nu \frac{E_z}{E_y} \tag{3.58}$$

3.5 Comparison with FE models

In this section, the analytical formulation is validated by means of FE simulations. First, the models are described, then a comparison of the results obtained from the two methods is carried out. Basically, a FE-based formulation is developed to show the accuracy of the developed analytical formulation. The FE-based methodology can be applied to every corrugation geometry, but it needs careful manual labour to properly define constraints, BCs and forces. Therefore, to show the methodology in a clear fashion, a proper validation geometry was chosen. The corrugation shape investigated is composed of two parts which have analytical solutions available in the literature, see Figure 3.9 for characteristics. The dimensions of this shape are: $p_1 = p_2 = 4.25$ mm, thus $P_0 = 8.5$ mm, $H_0 = 4$ mm and $t_c = 0.3$ mm. The constituent material is a standard aluminum with $E = 71000$ MPa and $\nu = 0.33$.

The width of the specimen is unitary as in the analytical formulation, representing a corrugated beam. Therefore, in order to obtain equivalent parameters for a plate-like corrugation, additional conditions are going to be imposed on some parameters.

The aim of this section is twofold: to compare the equivalent parameters for the straight part with previous results [13], and to validate with FE simulations the combination of the contributions from the two parts.

The FE models are built using standard 8 node hexahedral elements instead

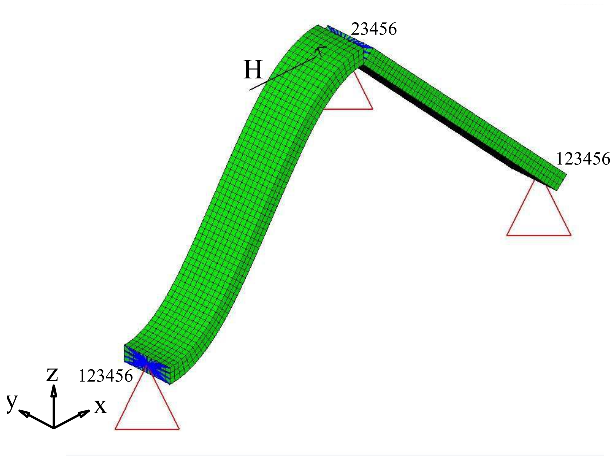

Figure 3.10: FE model for G_{xz} determination.

of the shell elements normally used in the literature, e.g. [2, 56], because solid elements are considered more appropriate to reproduce shear deformations.

3.5.1 G_{xz} model

The FE model for the determination of the first parameter can be seen in Figure 3.10. The lower ends are fully clamped, while the peak of the curve has only displacements in the *x-direction* allowed and a unit force H along x is applied to it. Rigid elements (thicker blue lines in Figure 3.10) are used to distribute constraints and forces on cross-section nodes; in addition, they allow relative movement in the *y-direction* to reproduce material contraction, i.e. the second degree of freedom (DOF) is not included in the rigid element definition. In other words, the constraints on the displacement along the *y-direction* are applied to prevent rigid body motion.

Given the width of the sample, this FE model is representative of the core of a sandwich beam. In order to model the core of a sandwich plate, additional BCs are needed on the faces perpendicular to the *y-direction*. In particular, the nodes of each of these sections must have the same displacement along y. This condition can be achieved including for each face a rigid element on the second DOF.

Once the displacement in the *x-direction* δ_x of the peak is computed, the equivalent shear modulus G_{xz} can be found as in Eq. 3.18.

3.5.2 E_x model

For this parameter the unit force along x is applied to the lower right edge which has only displacement δ_x along the *x-direction* allowed (Figure 3.11). The other lower edge is still fully clamped, while the line of contact with the upper bonding plate has both displacements along the x- and *z-direction* allowed – see Figure 3.11. As in the G_{xz} model, rigid elements allow relative movement in the

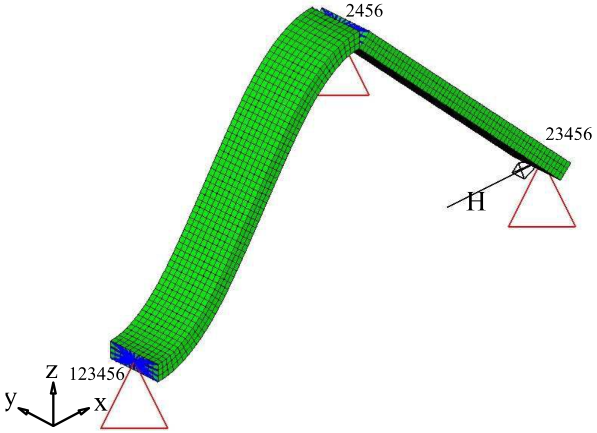

Figure 3.11: FE model for E_x determination.

y-direction to reproduce material contraction. From the deriving displacement δ_x, the Young's modulus can be computed as shown in Eq. 3.25.

As for the G_{xz} case, in order to reproduce a corrugated plate situation, the same rigid elements must be applied to the faces perpendicular to the *y-axis*.

3.5.3 E_y model

The FE model for this parameter is shown in Figure 3.12. The force acts along the *y-direction* and it is applied to an auxiliary node created as the centroid of the nodes in a cross section. A rigid element distributes the force to the cross-section nodes and imposes an equal displacement along the *y-direction* δ_y. The nodes of the other cross section are also linked to an auxiliary node with a rigid element which imposes the clamping of the second DOF (*y-direction*) of the auxiliary node to all the dependent nodes; for the sake of clarity, this latter rigid element is not shown in Figure 3.12.

The E_y parameter can be computed from the displacement δ_y as

$$E_y = \frac{\sigma_y}{\varepsilon_y} = \frac{H}{A_{xz}} \Big/ \frac{\delta_y}{l_y} = \frac{1}{H_0\ P_0\ \delta_y} \tag{3.59}$$

3.5.4 ν_{xy} model

The computation of the Poisson's ratio via FE analysis is performed with the model used in Section 3.5.2. The contraction δ_y of the loaded cross section must be extracted, so that

$$\nu_{xy} = \frac{\varepsilon_y}{\varepsilon_x} = \frac{\delta_y}{l_y} / \frac{\delta_x}{l_x} = P_0\ \frac{\delta_y}{\delta_x} \tag{3.60}$$

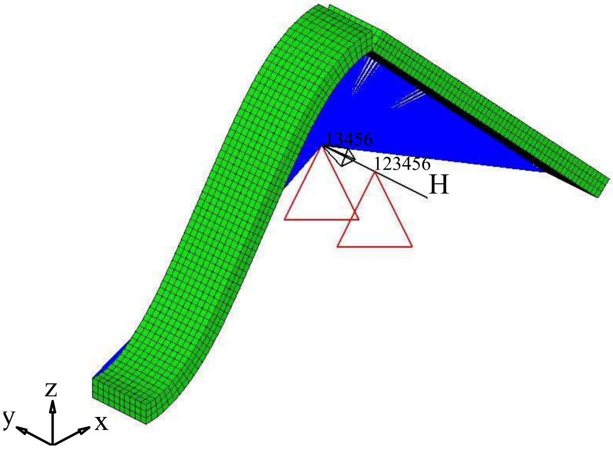

Figure 3.12: FE model for E_y determination.

Alternatively, this parameter can be derived starting from the two Young's moduli as in Section 3.2.4, Eq. 3.28.

3.5.5 G_{yz} model

The FE model for G_{yz} computation is derived from the one used in Section 3.5.1 (Figure 3.10) but the unit force on the upper edge is now acting along the *y-direction* and therefore the displacement of the upper point, now δ_y, is obtained in the same direction y. Moreover, to reproduce pure shear deformation, it is necessary to allow the movement of the nodes only in the *y-direction*: thus all the other DOFs of the nodes are constrained.

Once the displacement is computed, the equivalent parameter can be derived as

$$G_{yz} = \frac{\tau_{yz}}{\gamma_{yz}} = \frac{H}{A_{xy}} \Bigg/ \frac{\delta_y}{l_z} = \frac{H_0}{P_0\ \delta_y} \tag{3.61}$$

3.5.6 G_{xy} model

The model for the parameter G_{xy} can be obtained from the one used for E_y (Figure 3.12). The force is now acting in the *x-direction* and the displacement of the auxiliary node is computed in that direction, obtaining δ_x. The rigid element allows the cross section movements only in the *x-direction*. Moreover, all nodes not linked with rigid elements are constrained to have displacement only in the *x-direction* to reproduce pure shear conditions. From the displacement of the forced node, the equivalent shear modulus G_{xy} is

$$G_{xy} = \frac{\tau_{xy}}{\gamma_{xy}} = \frac{H}{A_{xz}} \Bigg/ \frac{\delta_x}{l_y} = \frac{1}{H_0\ P_0\ \delta_x} \tag{3.62}$$

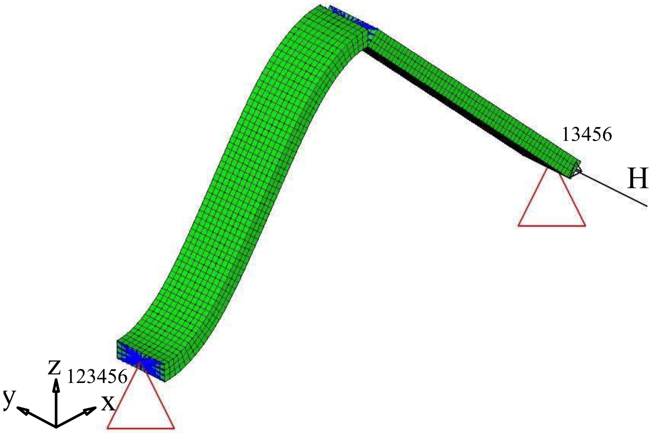

Figure 3.13: FE model for G_{yx} determination.

3.5.7 G_{yx} model

The FE simulation for this parameter is based on the model of Figure 3.13. The nodes of the lower-left edge are fully clamped, while all other nodes can translate only in the *y-direction* (in Figure 3.13, constraints are only shown for the initial and final cross sections).

Finally, the equivalent parameter G_{yx} can be obtained as

$$G_{yx} = \frac{\tau_{yx}}{\gamma_{yx}} = \frac{H}{A_{yz}} \Big/ \frac{\delta_y}{l_x} = \frac{P_0}{H_0\, \delta_y} \tag{3.63}$$

3.5.8 G_{zx} model

The FE model for the computation of this parameter is visible in Figure 3.14. A force along z is applied at the right lower edge, which has only z-displacement allowed, while the structure is fully clamped at the left lower edge. Moreover, the node in correspondence of the line of contact with the upper skin is allowed to translate along the *z-direction*, to ensure pure shear condition of the equivalent volume to be fulfilled.

Once the displacement δ_z of the loaded end is computed, the equivalent shear modulus G_{zx} is found as:

$$G_{zx} = \frac{\tau_{zx}}{\gamma_{zx}} = \frac{H}{A_{yz}} \Big/ \frac{\delta_z}{l_x} = \frac{P_0}{H_0} \frac{1}{\delta_z} \tag{3.64}$$

3.5.9 G_{zy} model

The model is similar to the one used for the G_{xy} parameter. The main difference is that the force is now acting in the *z-direction* and all nodes are allowed

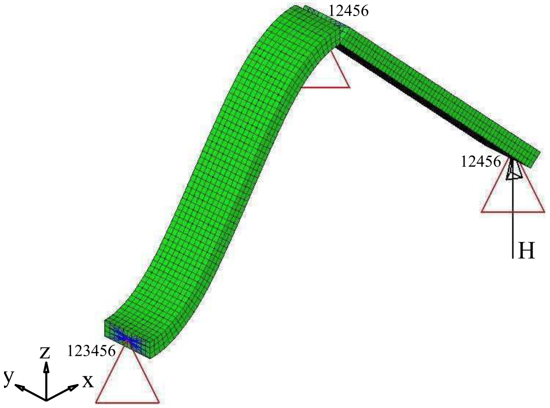

Figure 3.14: FE model for G_{zx} determination.

to move only in the *z-direction* to reproduce pure shear conditions. From the displacement of the forced node δ_z, the equivalent shear modulus G_{zy} is

$$G_{zy} = \frac{\tau_{zy}}{\gamma_{zy}} = \frac{H}{A_{xz}} \Big/ \frac{\delta_z}{l_y} = \frac{1}{H_0\ P_0\ \delta_z} \tag{3.65}$$

3.5.10 Elastic modulus in z-direction E_z

For the determination of the E_z parameter, the model in Figure 3.15 is used. The constraint conditions are basically the same as for the E_x determination. On the contrary, the force H, which acts along the *z-direction*, is now applied on the auxiliary node created on the cross-section in correspondence of the contact with the upper bonding plate. This auxiliary node is linked with a rigid element to the other cross-section nodes to equally distribute the force and the constraints. Indeed, this node is allowed only to translate along the x- and *z-direction.* Contraction along y is permitted since the rigid elements do not include the second DOF.

Once the displacement of the loaded node is determined in the *z-direction*, δ_z, the equivalent Young's modulus in that direction can be found as:

$$E_z = \frac{\sigma_z}{\varepsilon_z} = \frac{H}{A_{xy}} \Big/ \frac{\delta_z}{l_z} = \frac{H_0}{P_0}\frac{1}{\delta_z} \tag{3.66}$$

Once again, as for G_{xz} and E_x, this model shows a beam-like behaviour. To be representative of a plate situation, it is sufficient to add the already mentioned rigid elements – see Section 3.5.1.

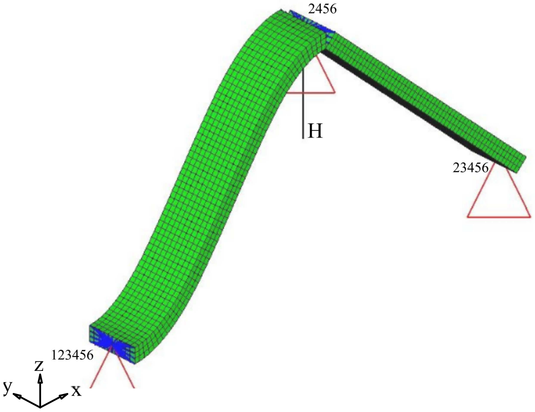

Figure 3.15: FE model for E_z determination.

3.5.11 Poisson's ratio in the *xz-plane* ν_{xz}

Starting from the model in Section 3.5.2, to determine this Poisson's ratio, the displacement in the *z-direction* of the auxiliary node on the upper cross section is extracted δ_z, together with the displacement along x of the loaded node, δ_x. From these values, the equivalent parameter can be computed as:

$$\nu_{xz} = \frac{\varepsilon_z}{\varepsilon_x} = \frac{\delta_z}{l_z} \Big/ \frac{\delta_x}{l_x} = \frac{P_0}{H_0}\frac{\delta_z}{\delta_x} \tag{3.67}$$

3.5.12 Poisson's ratio in the *yz-plane* ν_{yz}

To prove the validity of the assumption of this parameter being equal to the Poisson's ratio of the constituent material, the model used in Section 3.5.3 can be used. Contraction along z of the specimen must be derived, δ_z, together with the elongation in the *y-direction.* The equivalent Poisson's ratio can the be calculated as:

$$\nu_{yz} = \frac{\varepsilon_z}{\varepsilon_y} = \frac{\delta_z}{l_z} \Big/ \frac{\delta_x}{l_x} = \frac{P_0}{H_0}\frac{\delta_z}{\delta_x} \tag{3.68}$$

3.5.13 Comparison of results

In Table 3.1, the equivalent parameters for a Reissner-Mindlin plate representation of the validation geometry are reported. In the first row, results from the general formulation applied to the sinusoidal part of the investigated shape are shown. In the following three rows, results for the straight part of the shape, also called "T3", are given and compared. The comparison is done with results by Wang's formulation [13]. Finally, the results for the combined shape are shown and compared with FE results in the last three rows. Since the previous analytical formulation by Wang only addressed beam situations, the parameters are given for

Case	E_x [MPa]	E_y [MPa]	ν_{xy} [-]	ν_{yx} [-]	G_{xy} [MPa]	G_{yx} [MPa]	G_{xz} [MPa]	G_{yz} [MPa]
Sinusoidal part (Analyt.)	16.14	7.563E+3	7.044E-4	0.33	2.843E+3	1.410E+3	537.7	1.249E+3
Straight part “T3” (Analyt.)	21.56	7.314E+3	9.727E-4	0.33	2.750E+3	1.458E+3	1.824E+3	1.291E+3
Straight part “T3” (Ref. [13])	21.87	7.313E+3	9.873E-4	0.33	—	1.458E+3	1.821E+3	1.291E+3
Relative difference [%]	−1.42	0.01	−1.48	—	—	0.00	0.16	0.00
Sinusoidal-straight (Analyt.)	18.46	7.438E+3	8.190E-4	0.33	2.796E+3	1.433E+3	1.181E+3	1.270E+3
Sinusoidal-straight (FE)	18.94	7.437E+3	8.409E-4	0.33	2.790E+3	1.433E+3	1.183E+3	1.268E+3
Relative difference [%]	−2.59	0.02	−2.51	0.33	0.21	0.02	−0.18	0.17

Table 3.1: Comparison of equivalent parameters for the validation geometry – beam representation.

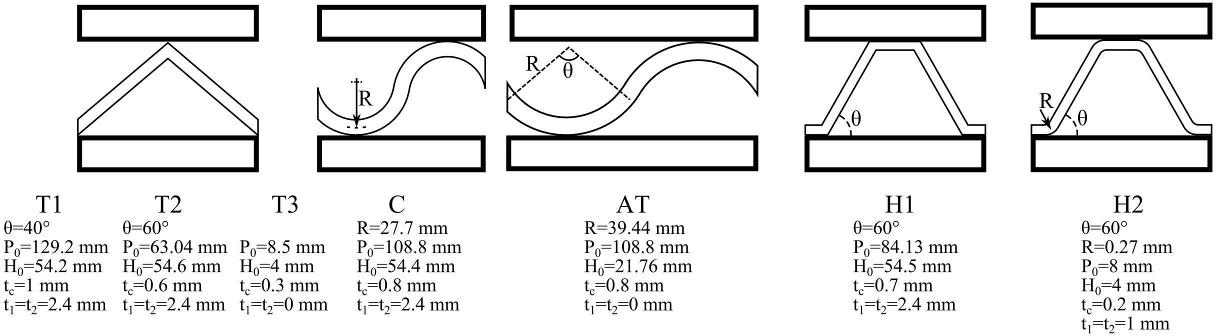
R
R θ
θ
R θ
T1 θ=40° P0=129.2 mm H0=54.2 mm tc=1 mm t1=t2=2.4 mm
T2 θ=60° P0=63.04 mm H0=54.6 mm tc=0.6 mm t1=t2=2.4 mm
T3 P0=8.5 mm H0=4 mm tc=0.3 mm t1=t2=0 mm
C R=27.7 mm P0=108.8 mm H0=54.4 mm tc=0.8 mm t1=t2=2.4 mm
AT R=39.44 mm P0=108.8 mm H0=21.76 mm tc=0.8 mm t1=t2=0 mm
H1 θ=60° P0=84.13 mm H0=54.5 mm tc=0.7 mm t1=t2=2.4 mm
H2 θ=60° R=0.27 mm P0=8 mm H0=4 mm tc=0.2 mm t1=t2=1 mm

Figure 3.16: Geometries and dimensions of the compared corrugated core structures.

Case	E_z [MPa]	ν_{xz} [-]	ν_{yz} [-]	G_{zx} [MPa]	G_{zy} [MPa]
Sinusoidal part (Analyt.)	19.67	0.8938	0.3300	8.350E+2	2.843E+3
Straight part “T3” (Analyt.)	16.92	1.123	0.3300	1.825E+3	2.750E+3
Straight part “T3” (Ref. [13])	17.16	-1.135	0.3300	—	—
Relative difference [%]	−1.40	−1.05	—	—	—
Sinusoidal-straight (Analyt.)	18.30	0.9918	0.3300	1.146E+3	2.796E+3
Sinusoidal-straight (FE)	18.78	0.9951	0.3291	1.156E+3	2.790E+3
Relative difference [%]	−2.56	−0.33	0.27	−0.85	0.21

Table 3.2: Comparison of additional equivalent parameters for the validation geometry – beam representation.

a corrugated beam, without loosing in generality. Results considering a corrugated plate for different shapes will be shown in the following section.

Since Wang et al. [13] is the only author found in the literature which gives also the values for a solid representation of the equivalent layer, in Table 3.2 the additional parameters are compared following the same row distribution of Table 3.1. In addition, in Table 3.2 also the other two additional shear moduli are given and compared only with FE simulations for the complete corrugation shape.

3.6 Comparison with previous results

In this section, an extensive validation of the proposed formulation is done by comparing its results with several authors for different shapes and constituent materials. Indeed, the most appealing peculiarity of this generalized formulation is that every kind of corrugation can be investigated, while typically previous authors developed specific solutions for each corrugation geometry. In case the proposed method gives different results from previous authors, FE simulations are set up to prove its validity and accuracy. The FE models are built using the same systems of forces and constraints shown in Section 3.5. The parameters are found for a plate situation according to the compared authors.

Several cases are analyzed (Figure 3.16): triangular, circular, arc-and-tangent and trapezoidal corrugations, while for a deeper investigation on sinusoidal profiles, please refer to Section 4. It is necessary to specify that in some cases only results for the whole panel are available in the literature, thus including the faces of the sandwich panels. For such cases, FE simulations are extended to the complete panel, where the faces are modelled as shell elements. Obviously, equivalent parameters need to be computed for the complete panel as well. This is done using the method explained in Section 2.1.2.

An important consideration on the literature results is that they typically consider only the in-plane behaviour of the sandwich construction, thus excluding the transverse shear moduli. In particular, no formulas for these parameters were found for the circular and arc-and-tangent core types, therefore the comparison of the two out-of-plane parameters for these geometries was not possible.

Case	Constituent material	E_x [GPa]	E_y [GPa]	ν_{xy} [-]	ν_{yx} [-]	G_{xy} [GPa]	G_{yx} [GPa]	G_{xz} [GPa]	G_{yz} [GPa]
T1 Buannic[57]	Steel	205.7	256.1	0.2409	0.3	89.94	—	—	—
T1 Proposed	Steel	205.6	256.4	0.2405	0.3	98.63	89.91	0.1240	7.407E-2
FE Simulation	Steel	—	—	—	—	98.63	89.96	0.1226	7.445E-2
T2 Buannic [57]	Steel	205.3	251.7	0.2447	0.3	82.47	—	—	—
T2 Proposed	Steel	205.3	252.0	0.2444	0.3	96.93	82.38	8.695E-2	0.1217
FE Simulation	Steel	—	—	—	—	96.92	82.43	8.507E-2	0.1220

Table 3.3: Comparison of equivalent parameters for triangular profile geometries – plate representation.

Case	Constituent material	E_x [GPa]	E_y [GPa]	ν_{xy} [-]	ν_{yx} [-]	G_{xy} [GPa]	G_{yx} [GPa]
C Buannic [57]	Steel	205.4	254.4	0.2423	0.3	85.76	—
C Kress [18]	Steel	205.4	254.4	0.2423	0.3	—	85.77
C Proposed	Steel	205.4	254.4	0.2423	0.3	97.84	85.77
C* Kress [18]	Steel	3.115E-4	4.851	1.926E-5	0.3	—	0.756
C* Proposed	Steel	3.114E-4	4.851	1.926E-5	0.3	1.866	0.756

Table 3.4: Comparison of equivalent parameters for circular profile geometries – plate representation. * indicates cases for which only the core is considered.

Case	Constituent material	E_x [GPa]	E_y [GPa]	ν_{xy} [-]	ν_{yx} [-]	G_{xy} [GPa]	G_{yx} [GPa]
AT* Kress [18]	Steel	6.582E-3	8.520	2.318E-4	0.3	—	2.691
AT* Proposed	Steel	6.580E-3	8.520	2.317E-4	0.3	3.277	2.691
FE simulation	Steel	6.582E-3	—	2.318E-4	—	—	—

Table 3.5: Comparison of equivalent parameters for arc and tangent profile geometries – plate representation. Only the core is considered.

3.6.1 Triangular-shaped cores

Two different papers were used as comparison for this shape, Buannic et al.[57] and Wang and Chung [13]. Buannic gives a general formulation valid also for other shapes as shown in the following sections. Nevertheless, that formulation is based on FE simulations and not easily implementable. Therefore, the two case studies presented there are used, namely "T1" and "T2" – see Figure 3.16. In [57], results are given for the total sandwich panel, thus including the faces, but considering that the equivalent layer has a thickness of 5 mm, i.e. the denominator of Eq. 2.3 is 5 mm instead of the total thickness, as well as the numerator of Eq. 2.9. The same assumption is made to compare results for such shapes.

The first geometry "T1", has the following features: $P_0 = 129.2$ mm, $H_0 = 54.2$ mm, $t_c = 1$ mm and $t_1 = t_2 = 2.4$ mm. The second geometry "T2" has: $P_0 = 63.04$ mm, $H_0 = 54.6$ mm, $t_c = 0.6$ mm and $t_1 = t_2 = 2.4$ mm. The constituent material is steel with $E = 210$ GPa and $\nu = 0.3$.

Results for the mentioned comparisons are shown in Table 3.3.

The second author, Wang, shows simple equations for the core, which are however only valid for triangular beam corrugations. Dimensions for this case are those already shown in Section 3.5, shape "T3" in Figure 3.16, and results are in Table 3.1. In this case, the parameters are not derived for a 5 mm equivalent layer, but considering the real thickness of the panel.

3.6.2 Circular-shaped cores

Two papers were compared also for the case of circular corrugations. The above-mentioned Buannic et al. [57], and Kress and Winkler [18]. The geometry by Buannic, namely "C", is fixed for the reason explained in Section 3.6.1 and the parameters are given for the whole panel (5 mm equivalent), while Kress gives an analytical formulation for the sole core. Therefore, the geometry has been chosen to be equal to that by Buannic with $P_0 = 108.8$ mm, $H_0 = 54.4$ mm, $t_c = 0.8$ mm and $t_1 = t_2 = 2.4$ mm. The corrugation consists of two semicircumferences in a period, therefore $R = 27.7$ mm, see Figure 3.16. The constituent material for this case study is steel. Results for this comparison are shown in Table 3.4, where the equivalent parameters are compared for both the whole panel and the sole core. As in Section 3.6.1, parameters for the only core do not consider an equivalent 5 mm layer.

3.6.3 Arc-and-tangent cores

The analytical formulation given by Kress an Winkler [18] allows to determine the equivalent parameters for a generalization of the circular shape, i.e. the arc and tangent profile (Figure 3.16). The geometric characteristics of this case study are: $P_0 = 108.8$ mm, $H_0 = 21.76$ mm, $t_c = 0.8$ mm. Therefore, in one period there are two arcs with radius $R = 39.44$ mm and angle $\theta = 87.21°$. The material is once again steel. Results of the obtained parameters for this core shape, called "AT", are shown in Table 3.5. Please note that only the core has been analyzed.

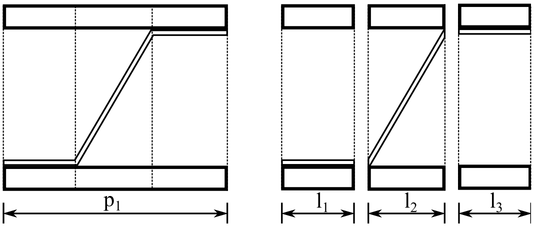

Figure 3.17: Split of the trapezoidal core sandwich panel and nomenclature.

3.6.4 Trapezoidal-shaped cores

For this core geometry, four authors were found to be relevant in the literature. Before introducing them, it is important to specify that the method proposed is specifically thought for corrugations with no horizontal parts. This is due to the fact that forces and constraints are applied to the extremities of the corrugation, which must coincide, for a proper modelling, with the conjunction points of the core with the faces. This does not happen for trapezoidal geometries. Nevertheless, the proposed method can still be used with a good accuracy for shapes with relatively short horizontal segments updating the derivation of the transverse shear moduli and the Young's modulus E_x when considering the complete panel. Indeed, it is necessary to split the sandwich structure in three parts as shown in Figure 3.17. The equivalent parameters E_x, G_{xz} and G_{yz} must be computed with the proposed method for the part No. 2. Hence the equivalent parameters of the trapezoidal corrugation can be derived as

$$E_x = p_1 / \left(\frac{l_1}{E_{x_1}} + \frac{l_2}{E_{x_2}} + \frac{l_2}{E_{x_2}} \right) \tag{3.69}$$

$$G_{xz} = G_{xz_1}\frac{l_1}{p_1} + G_{xz_2}\frac{l_2}{p_1} + G_{xz_3}\frac{l_3}{p_1} \approx G_{xz_2}\frac{l_2}{p_1} \tag{3.70}$$

$$G_{yz} = G_{yz_1}\frac{l_1}{p_1} + G_{yz_2}\frac{l_2}{p_1} + G_{yz_3}\frac{l_3}{p_1} \approx G_{yz_2}\frac{l_2}{p_1} \tag{3.71}$$

where the subscripts $1, 2, 3$ refer to the three parts in Figure 3.17 and $E_{x_1} = E_{x_2} = E(t_1 + t_2 + t_c)/(H_0 + t_1 + t_2)$.

The profile geometries investigated in this section are two (see Figure 3.16). One profile is proposed by Buannic et al. [57], namely "H1", which has the following dimensions: $H_0 = 54.5$ mm, $P_0 = 84.13$ mm, $t_c = 0.7$ mm, $t_1 = t_2 = 2.4$ mm and $\theta = 60°$. The other profile geometry, i.e. "H2", is based on the corrugation proposed by Libove and Hubka [24], and shows circular arcs of radius R between the horizontal and inclined segments. The dimensions of this profile are: $H_0 = 4$ mm, $P_0 = 8$ mm, $t_c = 0.2$ mm, $t_1 = t_2 = 1$ mm, $\theta = 60°$ and $R = 0.72$ mm. Results for this case study are given in Table 3.6. Since two authors derived formulas for the core only, without considering the faces, a comparison of the equivalent parameters for the core of the shape "H1" is also given. Please note that the com-

Case	Constituent material	E_x [GPa]	E_y [GPa]	ν_{xy} [-]	ν_{yx} [-]	G_{xy} [GPa]	G_{yx} [GPa]	G_{xz} [GPa]	G_{yz} [GPa]
H1 Buannic [57]	Steel	208.1	252.8	0.2469	0.3	84.54	—	—	—
H1 Libove [24]	Steel	205.4	253.0	0.2435	0.3	—	84.01	3.929E-3	1.052E-1
H1 Proposed	Steel	211.6	253.0	0.2509	0.3	97.31	84.01	7.616E-2	1.066E-1
FE simulation	Steel	210.7	—	0.2498	—	97.29	84.48	7.401E-2	1.043E-1
H1* Samanta [26]	Steel	3.454E-4	4.715	2.198E-5	0.3	0.5935	—	—	—
H1* Xia [23]	Steel	2.171E-4	4.715	1.382E-5	0.3	0.5935	—	—	—
H1* Proposed	Steel	2.169E-4	4.716	1.380E-5	0.3	1.814	0.5933	—	—
FE simulation	Steel	2.198E-4	—	1.397E-5	—	1.813	0.5960	—	—
H2 Libove	Aluminum	24.02	27.31	0.2902	0.33	—	9.476	0.1092	1.301
H2 Proposed	Aluminum	24.45	27.31	0.2954	0.33	10.27	9.476	0.4991	1.477
FE simulation	Aluminum	24.41	—	0.2950	—	10.27	9.491	0.4822	1.542

Table 3.6: Comparison of equivalent parameters for trapezoidal profile geometries – plate representation. * indicates cases for which only the core is considered.

parison for the core and for the "H2" geometry are carried out without considering the equivalent 5 mm thick layer.

3.7 Discussion

Analyzing the results obtained in the first comparison using FE simulations as reference, a very good accuracy is provided by the developed analytical formulation. For the validation geometry presented in Section 3.5, the relative difference between the two methodologies shows a maximum of about 2.6% on the E_x and the E_z parameters. This can be mainly attributed to the approximation of the straight part in Fourier series. Nevertheless, such a difference can be considered a very good result.

Moreover, comparing results for the sole straight part with the analytical formulation proposed by Wang et al. [13], a very good matching is found. The main difference consists in the ν_{xz} Poisson's ratio, which seems to be negative in Wang's formulation. Nevertheless, negative Poisson's ratios imply expansion when the material is stretched, which does not happen for the corrugation examined – easily verifiable with FE simulations. Probably an error on the sign is present in their formulation, since the absolute value is comparable with results from the formulation proposed in this dissertation.

Moving to the comparison with previous authors for different corrugation geometries, the proposed approach has shown a very good accuracy in all cases. If the previous comparison was carried out considering a beam-like structure, in these cases a plate representation was used, since typically previous authors derived equivalent parameters for plate-like situations. Therefore, the parameters which are supposed to be influenced by the width of the specimen were updating – see Section 3.2 for details.

For triangular corrugations, two different geometries were investigated in addition to the already introduced comparison with Wang et al. [13]. The comparison with Buannic et al. [57] showed a good agreement in the values of the various parameters both for the "T1" and "T2" shapes. Nevertheless, it is possible to observe an inversion in the results for the in-plane shear moduli. This is probably due to the different nomenclature convention used for the definition of the shear stresses and strains. On the other hand, the compared author does not explicitly mention the convention used, making the hypothesis impossible to be verified.

Also for circular-shaped cores, a very good agreement is found with results by Buannic et al. [57] for the complete panel, apart from the same inversion in the in-plane shear moduli. Moreover, the present formulation has shown an almost perfect matching also with the modelling by Kress and Winkler [18]. These authors gave a formulation valid for the sole core of the panel, thus comparison was possible both in the complete sandwich case and in the sole core situation. The same authors, Kress and Winkler [18], were the only ones to give an analytical description of the arc-and-tangent profile. Indeed, in their modelling, the circular corrugation is simply a particular case of the arc-and-tangent geometry. Therefore, the same considerations done for circular core can be done, proving the two analytical formulations to give almost the same results.

For the trapezoidal-shaped cores, results for the E_x parameter are slightly overestimated if compared to results from Buannic et al. [57]. Nevertheless, FE simulations showed results in between the two values. The difference in the E_x results between the proposed formulation and the FE method is probably due to the influence of the horizontal segments typical of this shape. Indeed, as already explained in Section 3.6.4, the present approach is thought for corrugations linked to each face of the panel only by a line in the crest and the valley of the geometry. Therefore, the application to trapezoidal cores is an extension of its applicability and the accuracy of the formulation is then obviously influenced by this. Indeed, to represent the behaviour of the complete panel with this corrugation shape, the formulation for the E_x parameter was slightly changed. For the same reason, also the two out-of-plane shear moduli were modified for this shape to account for horizontal segments when analyzing the complete panel. In the "H1" case, the accuracy for the G_{xz} parameter is very good and much better than that of Libove and Hubka [24], which is the only other author found to have determined this parameter. On the other hand, the proposed G_{yz} parameter shows a worse accuracy than Libove, but still the relative error with FE simulation is around 2%. In the "H2" case study, the proposed formulation shows a greater accuracy than Libove also on the G_{yz} parameter, but the relative error with FE simulation is now around 4%.

While investigating the sole core of the "H1" panel, no correction is now needed on the formulation, since no condition on the linking between core and faces is needed. Results from the present approach were comparable with those by Xia et al. [23] and in agreement with FE results. On the contrary, Samanta and Mukhopadhyay [26] gave higher values of the E_x parameter – and consequently the ν_{xy} ratio.

3.8 Conclusions

A general formulation to reduce a 3D corrugated core of a sandwich structure to an equivalent layer is presented. In particular, the properties of an equivalent orthotropic homogenous material are derived both in beam- and plate-like sandwich structures. The main feature of this analytical approach is that it allows to overcome the typical drawback of previous analytical formulations, i.e. their applicability only to a specific core geometry. Indeed, the proposed method allows obtaining the properties of the equivalent material for every kind of corrugation, since it starts from a representation of its shape as an approximated Fourier series. Moreover, the proposed formulation can be applied also to non-symmetric corrugations, which have never been investigated before. In addition, both in-plane and out-of-plane properties are derived, which allows to represent the equivalent layer with a Love-Kirchhoff or a Reissner-Mindlin theory. Finally, also a solid representation of the equivalent layer is possible, allowing to consider also thickness reduction of the core.

The accuracy of the proposed methodology was proven by means of a comparison with several authors and with different formulations. Four core profiles were investigated: triangular, circular, arc-and-tangent and trapezoidal cores – please note that investigation on sinusoidal cores is carried out in Chapter 4. For every corrugation, equivalent parameters were derived for different geometric characteristics, e.g. heights, periods and thicknesses, based on available results in the literature. The accuracy of the proposed methodology was proven to be comparable to, or even greater than, those of previous authors. Moreover, given the non-existence of non-symmetric shapes in the literature, a case study was obtained by the extreme combination of a sinusoidal half-period and a straight part, i.e. half of a triangular profile. Results were compared with FE simulations showing a very good accuracy with a maximum relative error of about 2.6%.

Chapter 4

A specific case: Sinusoidal corrugations

4.1 Introduction

The importance that corrugated cardboard has in the modern society is known to everybody, since it is a stiff, strong and light-weight material. Nevertheless, the constituent material, i.e. paper, is characterized by poor mechanical properties and a high variability, so that the best way to determine the properties of such structures is mainly based on experimental techniques.

Moving to structural sandwich panels, the substitution of paper with aluminum has led to the innovative sandwich panels with sinusoidal corrugated cores. The main feature of these structures is a high stiffness-to-mass ratio, especially under bending conditions, with a very limited overall thickness. Typical applications are for example in the railway industry as inner floors since they are able to withstand high loads, both point and distributed [58, 59]. The greater mechanical characteristics of aluminum respect to paper, allows a better accuracy in manufacturing the designed sinusoidal corrugation geometry, justifying an effort in describing analytically the performances of the obtained sandwich panels.

In Chapter 3, the analytical formulation to derive equivalent properties for generic corrugated cores was presented. Nevertheless, a lack of accurate formulations was found in the literature regarding sinusoidal cores. The proposed analytical formulation, given its versatility, can also be applied to this kind of corrugations. However, taking into consideration the characteristics of such profiles allows strongly simplifying the general formulation. In particular, if two functions were required to describe the two parts, now, thanks to the symmetry of the shape, only one is needed and the geometric parameters can be reduced, i.e. $p_1 = p_2 = p$.

This chapter is organized as follows. In Section 4.2 the simplified analytical formulation is shown. The validation with FE models and previous authors is carried out in Section 4.3. In addition, parametric validations are carried out in Section 4.4 concerning the bending stiffness of the panels and in Section 4.5 addressing the transmission loss properties. Finally, a discussion of the results is given in Section 4.6.

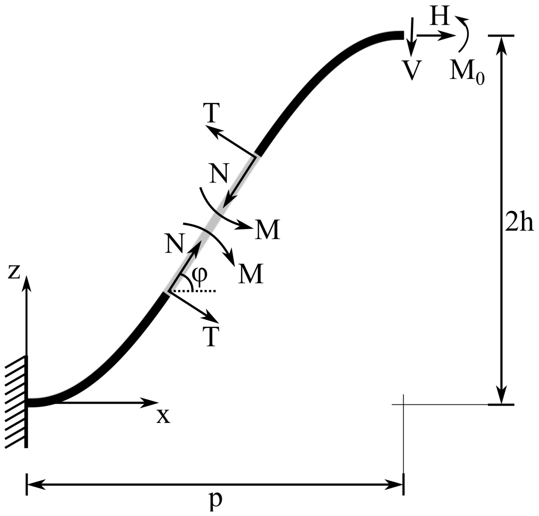

Figure 4.1: Loads and forces acting on the centre line: nomenclature.

4.2 Analytical simplified formulation

The formulation shown in Chapter 3 can be simplified when considering perfectly sinusoidal cores. Indeed, the shape is symmetric and the corrugation geometry can be described by a simpler function, which can be written as:

$$f(x) = \left(h - h \cos \frac{\pi x}{p} \right) \tag{4.1}$$

where h is the amplitude and p is the half-period of the sine curve. In addition, the first derivative can be expressed as,

$$f'(x) = \frac{hx}{p} \sin \frac{\pi x}{p} \tag{4.2}$$

Nevertheless, since the Fourier series is able to describe a sinusoidal function without introducing approximation errors, the two formulations are supposed to give the same results.

In the following paragraphs, the simplified formulation to determine equivalent parameters for sinusoidal corrugations is proposed.

4.2.1 Transverse shear modulus G_{xz}

Consider half a period of the sinusoidal corrugated sheet represented by its centre line, having thickness t_c and unitary width in *y-dir.*, $b = 1$. The origin of the reference system is set in correspondence of the lowest point and there the structure is clamped (Figure 4.1).

According to Figure 4.1, and assuming the inner forces as indicated in Eqs. 3.4–3.6, the partial derivatives of the inner forces with respect to the applied loads can be computed as:

$$\begin{aligned}
&\frac{\partial M}{\partial H} = h - h\cos\frac{\pi x}{p} && \frac{\partial M}{\partial V} = x && \frac{\partial M}{\partial M_0} = -1 \\
&\frac{\partial N}{\partial H} = cos\varphi && \frac{\partial N}{\partial V} = -sin\varphi && \frac{\partial N}{\partial M_0} = 0 \\
&\frac{\partial T}{\partial H} = sin\varphi && \frac{\partial T}{\partial V} = cos\varphi && \frac{\partial T}{\partial M_0} = 0
\end{aligned} \tag{4.3}$$

Therefore, applying the Castigliano's theorem [27], the vertical and horizontal displacements of the free end and its rotation can be found as:

$$\delta_H = \int_0^p \left(\frac{M\frac{\partial M}{\partial H}}{EI} + \frac{N\frac{\partial N}{\partial H}}{EA} + \frac{T\frac{\partial T}{\partial H}}{GA'} \right) \frac{\mathrm{d}x}{\cos\varphi} \tag{4.4}$$

$$\delta_V = \int_0^p \left(\frac{M\frac{\partial M}{\partial V}}{EI} + \frac{N\frac{\partial N}{\partial V}}{EA} + \frac{T\frac{\partial T}{\partial V}}{GA'} \right) \frac{\mathrm{d}x}{\cos\varphi} \tag{4.5}$$

$$\delta_{M_0} = \int_0^p \left(\frac{M\frac{\partial M}{\partial M_0}}{EI} + \frac{N\frac{\partial N}{\partial M_0}}{EA} + \frac{T\frac{\partial T}{\partial M_0}}{GA'} \right) \frac{\mathrm{d}x}{\cos\varphi} \tag{4.6}$$

Substituting Eq. 4.2 in the expressions for $\cos\varphi$ and $\sin\varphi$ (Eqs. 3.7), Eqs. 4.4–4.6 can be rewritten including Eqs. 3.4–3.6 as

$$\begin{bmatrix} \delta_H \\ \delta_V \\ \delta_{M_0} \end{bmatrix} = \frac{1}{EA} \begin{bmatrix} C_{1,1} & C_{1,2} & C_{1,3} \\ & C_{2,2} & C_{2,3} \\ sym. & & C_{3,3} \end{bmatrix} \begin{bmatrix} H \\ V \\ M_0 \end{bmatrix} \tag{4.7}$$

where

$$\begin{aligned}
C_{1,1} &= \frac{12}{t^2}F_1 + F_4 + \frac{2(1+\nu)}{\kappa}F_6 \\
C_{1,2} &= \frac{12}{t^2}F_2 - F_5 + \frac{2(1+\nu)}{\kappa}F_5 \\
C_{1,3} &= -\frac{12}{t^2}F_3 \\
C_{2,2} &= \frac{12}{t^2}F_7 + F_6 + \frac{2(1+\nu)}{\kappa}F_4 \\
C_{2,3} &= -\frac{12}{t^2}F_8 \\
C_{3,3} &= \frac{12}{t^2}F_9
\end{aligned} \tag{4.8}$$

being κ the shear factor of the beam ($\kappa = 5/6$) and F_i the integrals involved.

These integrals, listed in Eqs. 4.9, can be easily solved numerically, but not analytically, since they include elliptic integrals of the second kind.

$$\begin{aligned}
F_1 &= \int_0^p \left(h - h\cos\frac{\pi x}{p}\right)^2 \sqrt{1 + k^2 \sin^2\frac{\pi x}{p}}\,\mathrm{d}x \\
F_2 &= \int_0^p x\left(h - h\cos\frac{\pi x}{p}\right) \sqrt{1 + k^2 \sin^2\frac{\pi x}{p}}\,\mathrm{d}x \\
F_3 &= \int_0^p \left(h - h\cos\frac{\pi x}{p}\right) \sqrt{1 + k^2 \sin^2\frac{\pi x}{p}}\,\mathrm{d}x \\
F_4 &= \int_0^p \frac{1}{\sqrt{1 + k^2 \sin^2\frac{\pi x}{p}}}\,\mathrm{d}x \\
F_5 &= \int_0^p \frac{k\sin\frac{\pi x}{p}}{\sqrt{1 + k^2 \sin^2\frac{\pi x}{p}}}\,\mathrm{d}x \\
F_6 &= \int_0^p \frac{k^2\sin^2\frac{\pi x}{p}}{\sqrt{1 + k^2 \sin^2\frac{\pi x}{p}}}\,\mathrm{d}x \\
F_7 &= \int_0^p x^2 \sqrt{1 + k^2 \sin^2\frac{\pi x}{p}}\,\mathrm{d}x \\
F_8 &= \int_0^p x \sqrt{1 + k^2 \sin^2\frac{\pi x}{p}}\,\mathrm{d}x \\
F_9 &= \int_0^p \sqrt{1 + k^2 \sin^2\frac{\pi x}{p}}\,\mathrm{d}x
\end{aligned} \tag{4.9}$$

where

$$k^2 = \frac{h^2\pi^2}{p^2} \tag{4.10}$$

Imposing the same BCs of Section 3.2.1, allows obtaining the horizontal displacement as

$$\delta_H = \frac{1}{EA}\,\frac{\det(C)}{\det(C_{red})} \tag{4.11}$$

Therefore, the equivalent G_{xz} can be obtained as:

$$G_{xz} = \frac{\tau_{xz}}{\gamma_{xz}} = \frac{F_x}{p}\Big/\frac{\delta_x}{2h} = \frac{2h}{p}\cdot\frac{1}{\delta_H} \tag{4.12}$$

As already seen in the general formulation, this parameter is derived for a beam-like structure. To have a plate behaviour of the corrugation, it is sufficient to substitute the constituent material Young's modulus E with $E/(1-\nu^2)$ in Eq. 4.7.

4.2.2 Elastic modulus in x-direction E_x

With the same methodology proposed in Section 3.2.2, the horizontal displacement under tensile conditions can be found as

$$\delta_H = \frac{1}{EA}\left(C_{1,1} - \frac{C_{1,3}^2}{C_{3,3}}\right) \tag{4.13}$$

and the equivalent Young's modulus E_x is obtained as:

$$E_x = \frac{\sigma_x}{\varepsilon_x} = \frac{F_x}{A_{yz}} \Big/ \frac{\delta_x}{l_x} = \frac{p}{2h} \cdot \frac{1}{\delta_H} \tag{4.14}$$

The same substitution in the Young's modulus is needed for plate-like structures.

4.2.3 Elastic modulus in y-direction E_y

The modulus of elasticity in the lateral direction can be found as:

$$E_y = E\frac{t_c l'}{2hp} \tag{4.15}$$

where l' is the length of half a period of the sine curve and can now be computed as:

$$l' = \int_0^p \sqrt{1 + |f'(x)|^2}\, \mathrm{d}x = \int_0^p \sqrt{1 + \frac{h^2\pi^2}{p^2}\sin^2\frac{\pi x}{p}}\, \mathrm{d}x \tag{4.16}$$

4.2.4 In-plane Poisson's ratio ν_{xy}

The Poisson's ratio ν_{xy} does not change from the general formulation, because it is derived from E_x and E_y.

4.2.5 Transverse shear modulus in yz-plane G_{yz}

The transverse shear modulus G_{yz} can be found with the same hypothesis done in Section 3.2.5. In the sinusoidal case it becomes:

$$G_{yz} = G\frac{2h\, t_c}{p\, l'} \tag{4.17}$$

4.2.6 In-plane shear modulus G_{xy}

Simplifying once again the general formulation in Section 3.2.6, the G_{xy} parameter can be obtained as

$$G_{xy} = G\frac{t_c\, l'}{2h\, p} \tag{4.18}$$

4.2.7 In-plane shear modulus G_{yx}

The simplified expression for G_{yx} is

$$G_{yx} = G\frac{t_c}{2h\,l'} \tag{4.19}$$

4.2.8 Transverse shear modulus G_{zx}

According to the simplifications done for the G_{xz} and E_x parameters, the system of equations 4.7 can be used as the starting point to compute the G_{zx} parameter. Imposing a unit vertical force V and the BCs $\delta_H = \delta_{M_0} = 0$, it is possible to compute the vertical displacement δ_V as in Eq. 3.43 and consequently the transverse shear modulus as

$$G_{zx} = \frac{\tau_{zx}}{\gamma_{zx}} = \frac{F_z}{A_{zy}}\Bigg/\frac{\delta_z}{l_x} = \frac{p}{2h}\cdot\frac{1}{\delta_V} \tag{4.20}$$

4.2.9 Transverse shear modulus G_{zy}

The same considerations done for a generic shaped core lead to the relation $G_{zy} = G_{xy}$.

4.2.10 Elastic modulus in z-direction E_z

The same procedure of Section 3.4.1 can be used. Only one half of the corrugation is considered now to find

$$\delta_V = \frac{1}{EA}\left(C_{2,2} - \frac{C_{2,3}^2}{C_{3,3}}\right) \tag{4.21}$$

and the Young's modulus in the *z-direction* as:

$$E_z = \frac{\sigma_z}{\varepsilon_z} = \frac{F_z}{A_{xy}}\Bigg/\frac{\delta_z}{l_z} = \frac{2h}{p}\cdot\frac{1}{\delta_V} \tag{4.22}$$

Once again, to have a parameter representative of a plate-like structure, substitute E with $E/(1-\nu^2)$.

4.2.11 Poisson's ratio in the *xz-plane* ν_{zx}

The same procedures shown in Section 3.4.2 can be used here, but no average value is needed on the contraction values, since the two halves of the corrugation are equal. Moreover, the various coefficient in the matrix $\boldsymbol{C}$ are updated according to Eqs. 4.7–4.9.

4.2.12 Poisson's ratio in the *yz-plane* ν_{zy}

As for ν_{xy}, the computation of this parameter does not change, being derived from E_z and E_y.

4.3 Comparison with FE models and previous authors

Compared with the other corrugation profiles, a deeper investigation is carried out for sinusoidal shapes, since these innovative panels are the main target of the present work. For this corrugation geometry, parametric studies were carried out to compare the parameters obtained from the analytical formulation with those from FE simulations for different values of the design variables. A beam representation is considered in the following.

A routine was developed to scale the FE models in order to define the updated configuration and to automatically compute the equivalent parameters. To validate the analytical formulation and compute relative errors, FE results were taken as reference. For the parametric studies, all but one parameters were kept constant and equal to the values of a typical commercial panel, i.e. $t = 0.3$ mm, $p = 4.25$ mm and $h = 2$ mm. Parameter ranges were chosen on the basis of typical manufacturing limitations for standard applications. In addition, results from previous works are included in the graphs. Since E_y and G_{yz} are obtained analytically in the same way as previous authors, they are plotted only once. Moreover, only one shear modulus is compared for each plane.

In particular, the following authors are compared (see Section 2.2.4 for more details):

- G_{xz}: two papers by Isaksson et al. [32] and Nordstrand et al. [36] were compared;
- E_x: Briassoulis [17] is compared, since he gives a similar derivation of this parameter. The main difference is that in the present work the inclination angle φ is computed as a function of the derivative of $f(x)$, whereas in [17] is considered constant and equal to $\frac{p}{l'}$;
- E_y: it is calculated by several authors, e.g. [32, 35], since it can be obtained simply scaling the constituent Young's modulus; comparison was then carried out only with FE simulations;
- G_{yz}: Isaksson et al. [32] gave the same relation as the one proposed in Section 4.2.5, improving Nordstrand's results [36], thus comparison is only with FE results;
- G_{xy}: the Baum's approximation is included together with results by Briassoulis [17];
- ν_{xy}: is usually derived from E_x and E_y, thus only the author compared in those cases, Briassoulis [17], is included in the comparison.

A first parametric study was performed varying the thickness of the core corrugated lamina t from 0.2 mm to 2 mm with a step of 0.1 mm. Results are shown in Figure 4.2 for the first six parameters. The equivalent density was not compared, since its determination is quite trivial with result differences solely due to the core shape approximation of the FE model.

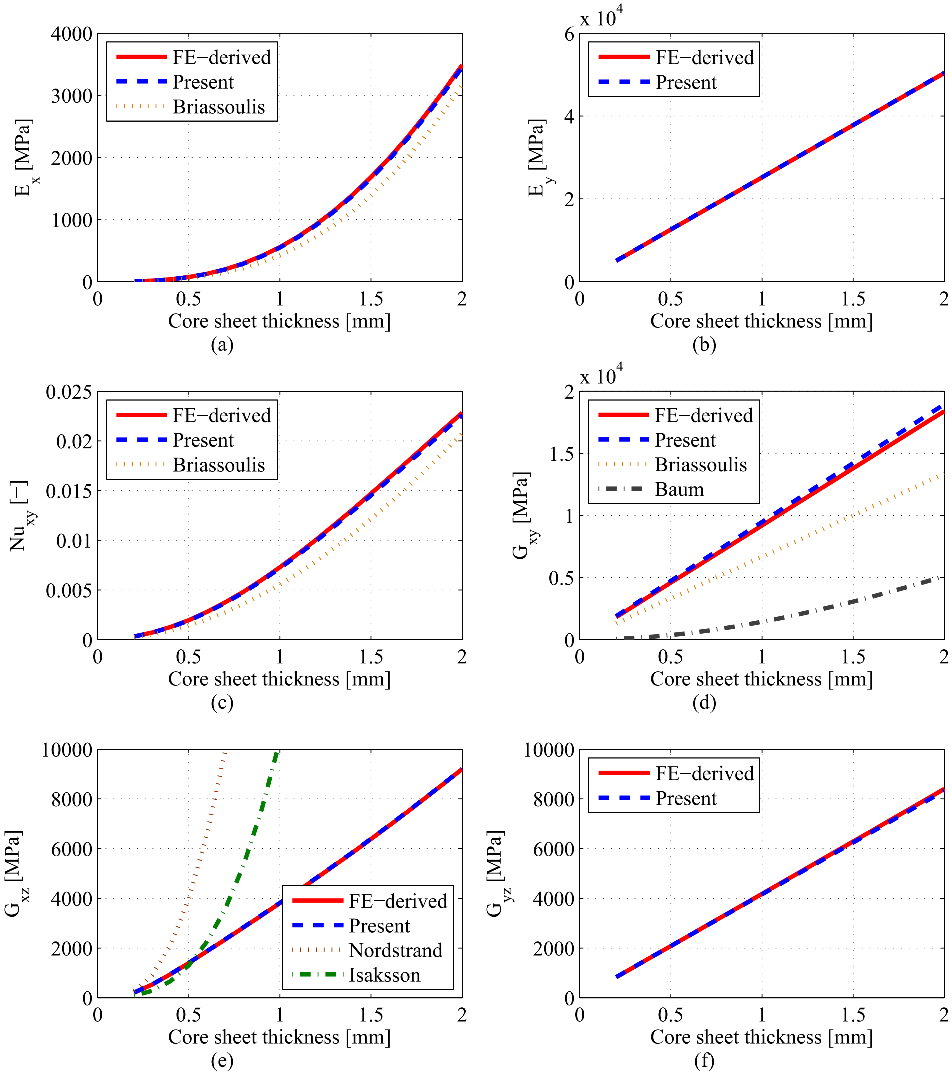

Figure 4.2: Parameter comparison varying the core sheet thickness:(a) Young's modulus in *x-direction* (b) Young's modulus in *y-direction*(c) In-plane Poisson's ratio (d) In-plane shear modulus (e) Transverse shear modulus in *xz-plane* (f) Transverse shear modulus in *yz-plane*. In (b) and (f) results from previous authors coincide with "Present".

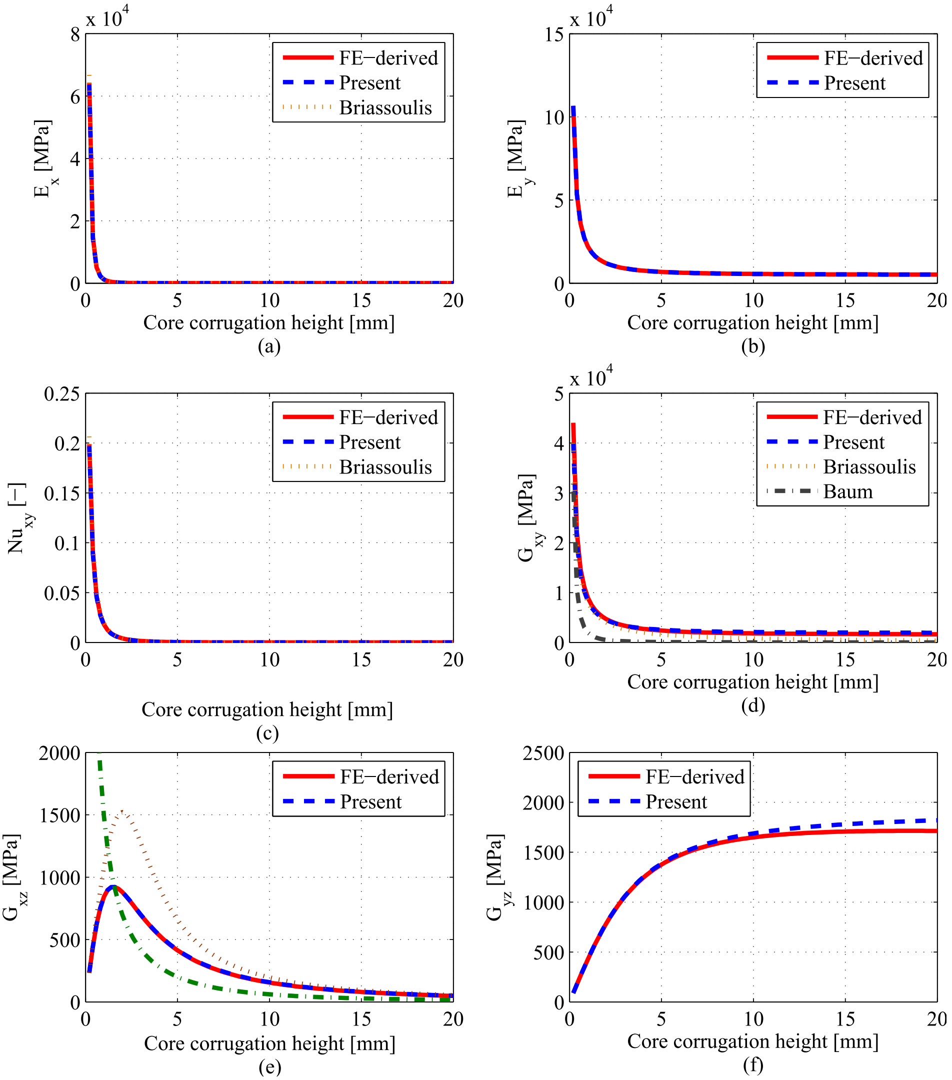

Figure 4.3: Parameter comparison varying the core height:(a) Young's modulus in *x-direction* (b) Young's modulus in *y-direction*(c) In-plane Poisson's ratio (d) In-plane shear modulus (e) Transverse shear modulus in *xz-plane* (f) Transverse shear modulus in *yz-plane*. In (b) and (f) results from previous authors coincide with "Present".

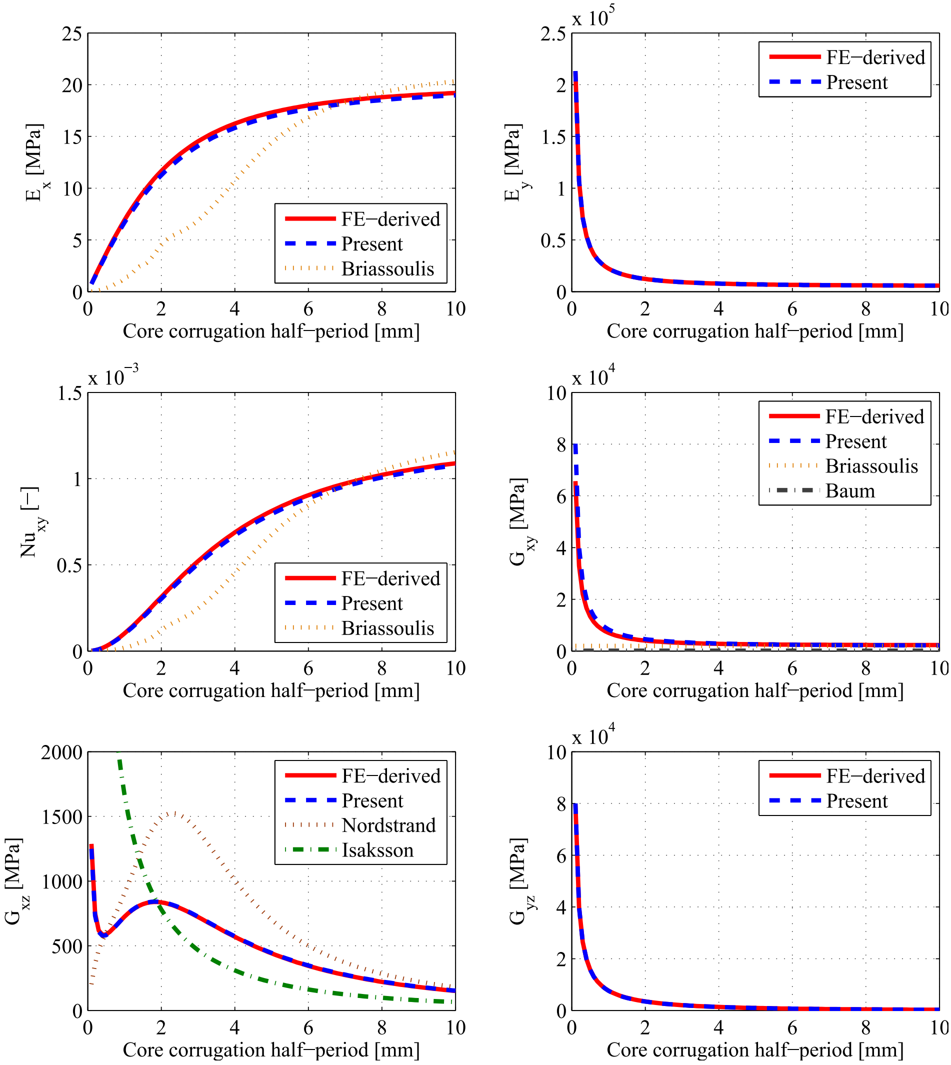

Figure 4.4: Parameter comparison varying the corrugation period:(a) Young's modulus in *x-direction* (b) Young's modulus in *y-direction*(c) In-plane Poisson's ratio (d) In-plane shear modulus (e) Transverse shear modulus in *xz-plane* (f) Transverse shear modulus in *yz-plane*. In (b) and (f) results from previous authors coincide with "Present".

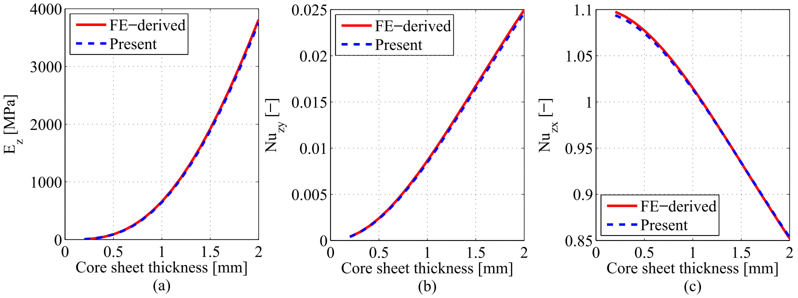

(a) (b) (c)

Figure 4.5: Additional parameter comparison varying the core sheet thickness: (a) Young's modulus in *z-direction*, (b) Poisson's ratio in *yz-plane*, (c) Poisson's ratio in *xz-plane*.

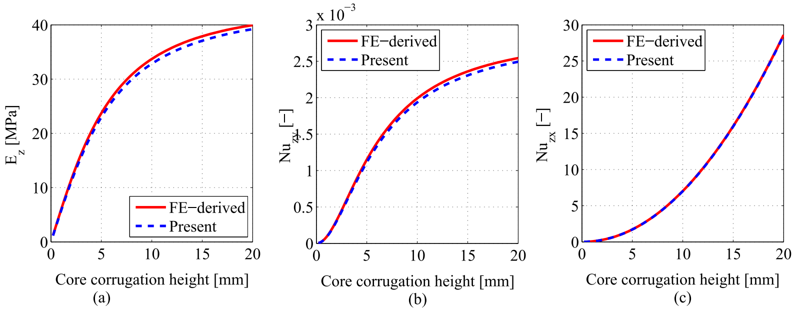

(a) (b) (c)

Figure 4.6: Additional parameter comparison varying the core height: (a) Young's modulus in *z-direction*, (b) Poisson's ratio in *yz-plane*, (c) Poisson's ratio in *xz-plane*.

In the second study the total height of the core $2h$ was varied from 0.2 mm to 20 mm in 0.2 mm steps. Results are shown in Figure 4.3.

In the last study the period of the corrugation p was varied in 0.1 mm steps from 0.1 mm to 10 mm. Results are plotted in Figure 4.4.

The same three parametric studies are set up for the additional parameter for the solid representation of the equivalent core layer. Results are shown in Figure 4.5 varying the thickness of the core lamina, in Figure 4.6 varying the amplitude of the sine curve and in Figure 4.7 varying the period of the sinusoid.

4.4 Static validation for sinusoidal cores

In this section, a comparison is carried out for the validation of the equivalent model in bending. The complete sandwich panel was investigated, including the two 1 mm face sheets.

Three models were compared: (i) "3D model", with fully detailed 3D geometry represented; (ii) "Layered panel-An", a multilayered representation with the

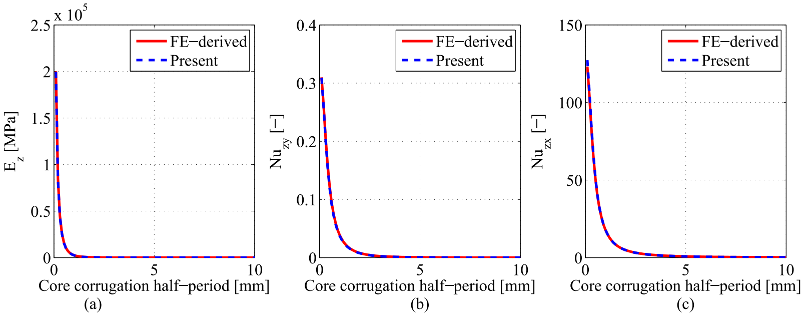

(a) (b) (c)

Figure 4.7: additional parameter comparison varying the corrugation period: (a) Young's modulus in *z-direction*, (b) Poisson's ratio in *yz-plane*, (c) Poisson's ratio in *xz-plane*.

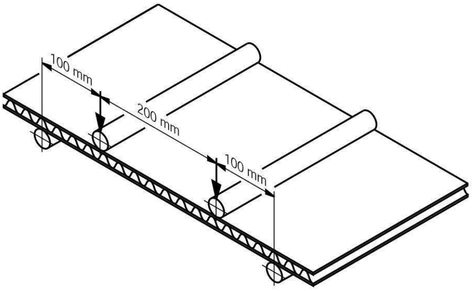

Figure 4.8: Scheme of the bending test and used distances.

equivalent core material characterized by the parameters analytically derived in Section 4.2; (iii) "Layered panel-FE", as the previous one, but with FE-derived core parameters as in Section 3.5. In the last two models, the equivalent core was included in a multilayered representation of the panel together with the two faces: the coupling is modeled assuming perfect bonding between layers (PCOMP card [60]).

The bending FE simulation was set up according to DIN 53293 [61], reproducing the 4-point bending test with the bending moment applied around the *y-axis* to obtain the bending stiffness in the transverse direction. In Figure 4.8, the general layout of the test and an indication of the distances used are given. From this simulation the bending stiffness per unit width D was obtained.

Again, a parametric study was performed with the same variables and ranges as in Section 4.3. Results are presented in Figure 4.9. The constant parameters were taken from baseline configuration, i.e. $t = 0.3$ mm, $p = 4.25$ mm and $h = 2$ mm.

Please note that, varying the period of the corrugation, the FE simulations for the 3D model were done only for a reduced set of p values (Figure 4.9 (c)). In fact, to keep forces and constraints applied in correspondence of the sine crests and to

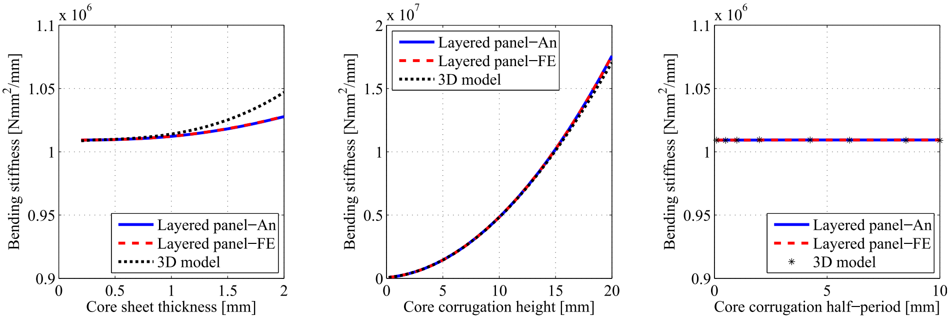

(a) (b) (c)

Figure 4.9: Parametric study on bending stiffness. Variables: (a) Thickness of the core sheet, (b) Height of the corrugation, (c) Half-period of the sinusoidal core.

maintain distances between them constant, only models with certain periods could be created.

4.5 Acoustic validation for sinusoidal cores

The last validation of the equivalent orthotropic material representation involved the acoustic performance of the panel. As in Section 4.4, the complete sandwich panel, including face sheets, is analysed here. The transmission loss (TL) spectrum in the frequency range $100 - 3150$ Hz was calculated in one-third-octave bands for the three models. The numerical computation was done using the Periodic Subsystem method [62], taking advantage of the periodic nature of the structure. In fact, to represent the typical dimensions of panel samples for acoustic testing, i.e. 1.40×1.35 m, a reduced panel (127.5×112.5 mm) was considered as the base cell to be repeated 11 times along the x- and 12 times along the y-*direction*.

A parametric study was undertaken to determine TL spectra in the parameter ranges previously introduced. Results are shown in Figures 4.10–4.12.

For the sake of brevity, only two spectra for each parameter are shown, but similar results were obtained for all configurations. The constant parameters are throughout taken from the values of the standard configuration. In Tables 4.1 and 4.2, differences between the layered and the 3D models are shown for different sheet thicknesses and core heights, averaged over the frequency range considered.

As for the static validation, given the difficulty to build a model of the panel with predetermined dimensions while varying the period of the core corrugation, only the configurations already shown in Figure 4.12 were considered for the parameter p.

Note that the time needed to compute the TL spectrum of the 3D model is about 14 hours on a standard PC while the layered model is solved in less than 2 minutes, see Table 4.3 for system specifications.

Taking advantage of the efficiency of the layered model, a comprehensive para-

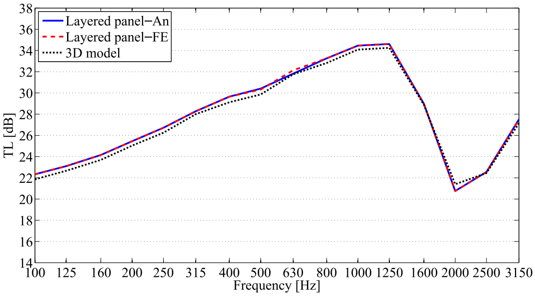

(a) Core thickness 0.6 mm

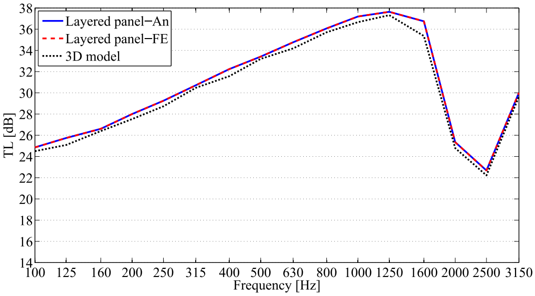

(b) Core thickness 1.6 mm

Figure 4.10: TL comparison for different core thicknesses.

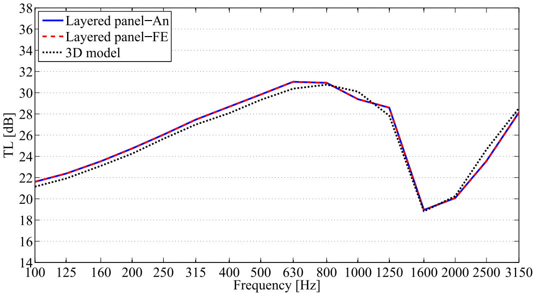

(a) Core height 6 mm

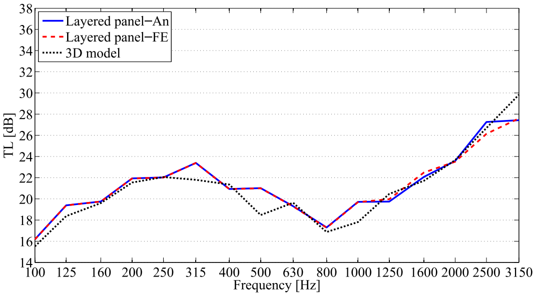

(b) Core height 16 mm

Figure 4.11: TL comparison for different core heights.

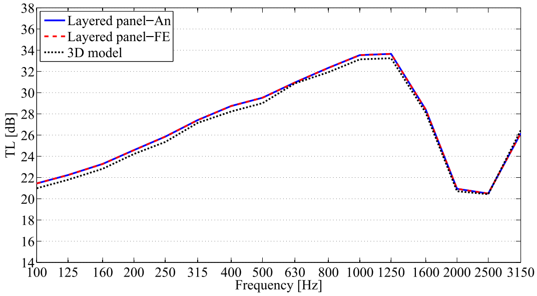

(a) Core half-period 3.75 mm

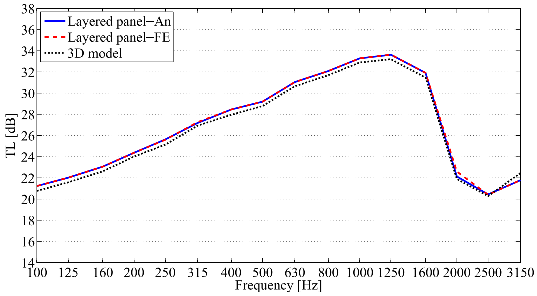

(b) Core half-period 6.375 mm

Figure 4.12: TL comparison for different corrugation periods.

	Mean error [dB]	
t [mm]	Layered panel-An	Layered panel-FE
0.2	0.467	0.465
0.4	0.398	0.372
0.6	0.377	0.391
0.8	0.659	0.659
1.0	0.664	0.664
1.2	0.758	0.758
1.4	0.529	0.529
1.6	0.495	0.495
1.8	0.580	0.580
2.0	0.509	0.509

Table 4.1: TL difference in dB, averaged over the frequencies, varying the core sheet thickness.

metric study of the panel acoustic performance was carried out by computing the TL spectra in smaller steps than in Tables 4.1 and 4.2: 0.02 mm for t, 0.1 mm for h and p. Results are plotted in Figures 4.13, 4.14 and 4.15.

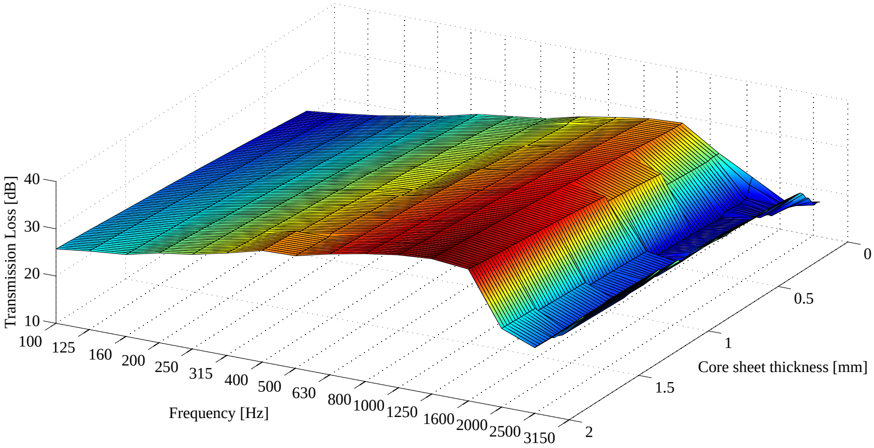

Figure 4.13: Variation of sound TL with the core sheet thickness t.

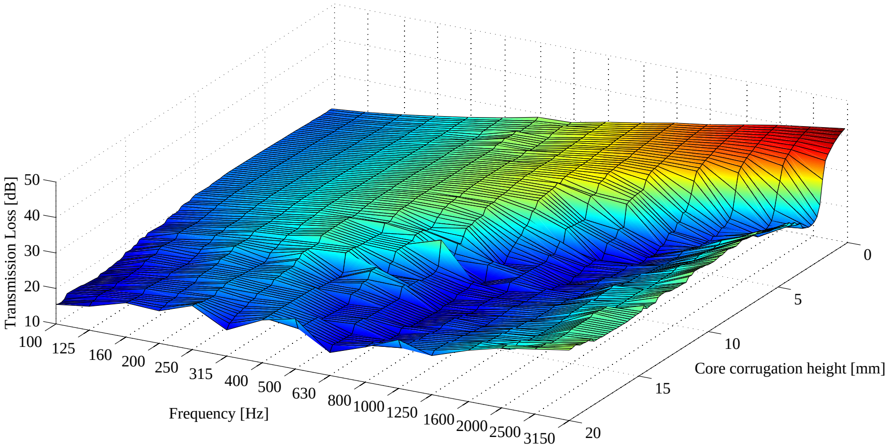

Figure 4.14: Variation of sound TL with the core corrugation height $2h$.

Mean error [dB]		
2*h [mm]	Layered panel-An	Layered panel-FE
2	0.584	0.584
4	0.369	0.368
6	0.493	0.496
8	0.993	1.000
10	0.503	0.611
12	1.206	1.356
14	1.158	1.146
16	0.852	0.853
18	1.093	1.104
20	1.496	1.470

Table 4.2: TL difference in dB, averaged over the frequencies, varying the core height.

Hardware properties	
Processor	AMD Athlon II X4 630
No. cores	4
Clock speed	2.80 GHz
Operating system	Windows XP 64-bit
RAM	8 GB

Table 4.3: Characteristics of the used hardware.

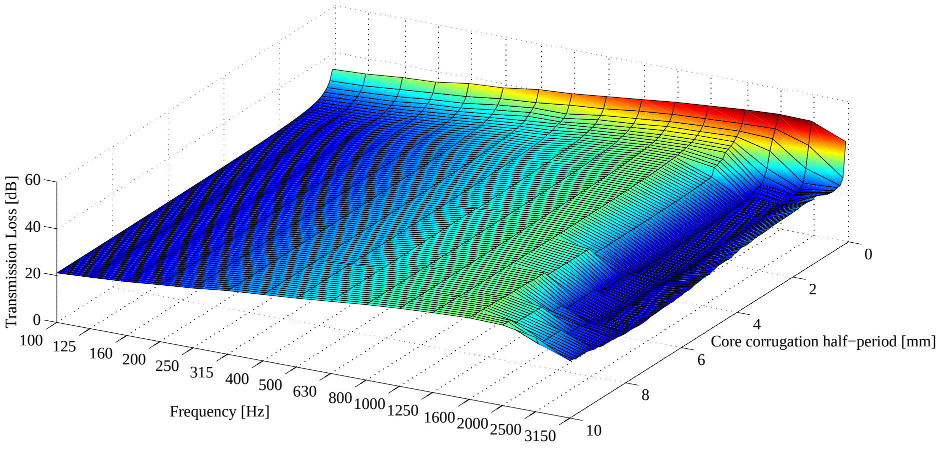

Figure 4.15: Variation of sound TL with the core corrugation half-period p.

4.6 Discussion

4.6.1 Comparison with FE models and previous authors

The comparison of the proposed analytical technique with FE models has shown a very good agreement between the two formulations, as expected from results in Chapter 3. Nevertheless, the additional parametric studies proposed for the sinusoidal shape has shown that the dependence on the three geometric parameters of the sinusoidal shape is well represented by the analytical formulation. On the contrary, parameters obtained from previous works give a good approximation of the FE-derived ones only for some restricted ranges of core configurations.

Minor differences are visible in the graphs between the present analytical approach and FE-derived parameters. When varying the thickness of the core sheet, a small difference (less than 3% in the investigated range) is observed in the in-plane shear modulus G_{xy} (Figure 4.2 (d)). Similarly, for the core height variation (Figure 4.3), around 6% difference is observed in the transverse shear modulus G_{yz} for thick panels (high $2h$ values). Nevertheless, these differences can be considered a good approximation of the parameters, given the wide ranges investigated. On the other hand, for very small corrugation lengths ($p \approx 0.1$) the analytical formulation for G_{xy} overestimates by up to 20% (Figure 4.4 (d)).

The differences for calculated G_{xy} probably depend on the approximation of the shear coefficient to 5/6. However, this parameter is likely to have a small influence on the bending and acoustic behaviour of the panel, which is mainly dominated by the transverse moduli. Moreover, the errors are observed for extreme corrugation lengths, i.e. $p \approx 0.1$, which are not relevant to real applications as such small periods are not practically feasible.

4.6.2 Static validation for sinusoidal cores

The static validation has proved that the bending stiffness of the sandwich panel is well represented when varying both the height of the core and the corrugation period – Figure 4.9 (b) and Figure 4.9 (c). Nevertheless, some aspects need to be considered for the other parametric study, thus varying the thickness of the corrugation.

According to Figure 4.9 (a), the panel bending is reproduced with a good approximation but a slight difference is visible when increasing the core sheet thickness. A deeper investigation on this behaviour could be of interest. Nevertheless, the error of the equivalent layered models remains smaller than 2% for the maximum thickness value of 2 mm, which was chosen to be the limit since the amplitude of the sinusoid is $h = 2$ mm. Moreover, these differences are depending on the layered model definition used and not on the formulation of the equivalent parameters. Indeed, both the analytical formulation and the FE-based methodology give the same accuracy on the wide range of configurations investigated.

4.6.3 Acoustic validation for sinusoidal cores

Also in the determination of the acoustic performance of sandwich panels, the two formulations, analytical and FE-based, yield almost identical results (Figures 4.10 – 4.12). The equivalent layered model reproduces the TL spectrum of the fully detailed 3D model with very good accuracy in the whole investigated range with a maximum mean error, as defined in Section 4.5, being around 1.5 dB.

Finally, the parametric studies show that changing the corrugation thickness t and period $2p$ has limited effect on the panel coincidence frequency, as it lies in the frequency bands centered at 2000 or 2500 Hz for the entire range analysed. In fact, the main effect is a shift of the TL spectrum due to mass variation: the acoustic performance increases when t increases or p decreases, see Figure 4.13 and Figure 4.15. On the other hand, the core height h has a strong influence also on the coincidence frequency, as visible in Figure 4.14.

4.7 Conclusions

The present chapter has shown an analytical formulation to reduce a sinusoidal core of sandwich structures to an equivalent layer. The general analytical formulation proposed in Section 3 was therefore simplified considering the main features of the sinusoidal shape, i.e. symmetric corrugation and easier function to describe the core profile.

The present analytical technique proposed for deriving the properties of the equivalent homogenous material has shown an accuracy comparable to that of FE-based techniques in calculating all relevant structural parameters to characterize the sandwich panel. Moreover, it is quicker and easier to use, especially in processes that involve several different configurations like parametric studies and optimization schemes. The proposed analytical technique has been compared also with previous formulations, showing the great improvement this work gives in modelling the equivalent layer for sinusoidal cores.

Furthermore, the layered representation of the sandwich panel has shown a good accuracy in describing the bending and acoustic performance compared to results from a detailed 3D model while drastically reducing the solving time. For acoustic transmission computations, the 14 hours needed for the 3D model were reduced to less than 2 minutes for the layered plate.

Chapter 5

Experimental validation

5.1 Introduction

It is well know since the origin of the scientific method, that theory and experiments are strictly related one to each other. In particular, experimental activities are often used to prove the validity of assumptions and analytical methodologies. Nowadays, it is always more and more often that experimental tests are replaced by FE simulations. Nevertheless, FE models are built modelling the structures based on some, even strict, hypotheses.

In order to investigate the accuracy of the homogenization techniques developed in the analytical part of this dissertation, Chapters 3 and 4, an experimental campaign was performed on available panels to better understand the peculiarities of the proposed formulations. Both the main static and dynamic characteristics of these structures are considered by means of a modal analysis and two different tensile tests.

Four different panels are available, whose main characteristics are listed in Table 5.1. It is important noting that, depending on the panel, the geometric features of the sinusoidal corrugation, i.e. amplitude and period, can vary a lot. These dimensions are fundamental to determine the equivalent properties of the core and therefore the overall behaviour of the sandwich panel. Typically, the amplitude of the sine curve is supposed to be half the core height ($h = H_c/2$), thus excluding the thickness of the corrugated lamina, while the period must be measured and is reported in the last column of Table 5.1. The aim of this chapter is therefore to compare results obtained from the multi-layer equivalent model with experimental data for these four configurations.

Panel denomination	Thickness face 1 [mm]	Core sheet thickness [mm]	Thickness face 2 [mm]	Total height [mm]	Period [mm]
05_02_05 H6	0.5	0.2	0.5	6.0	2.50
08_02_05 H6	0.8	0.2	0.5	6.0	4.24
10_03_10 H6	1.0	0.3	1.0	6.0	4.25
10_03_10 H11.5	1.0	0.3	1.0	11.5	7.14

Table 5.1: Main dimensions of the available panels.

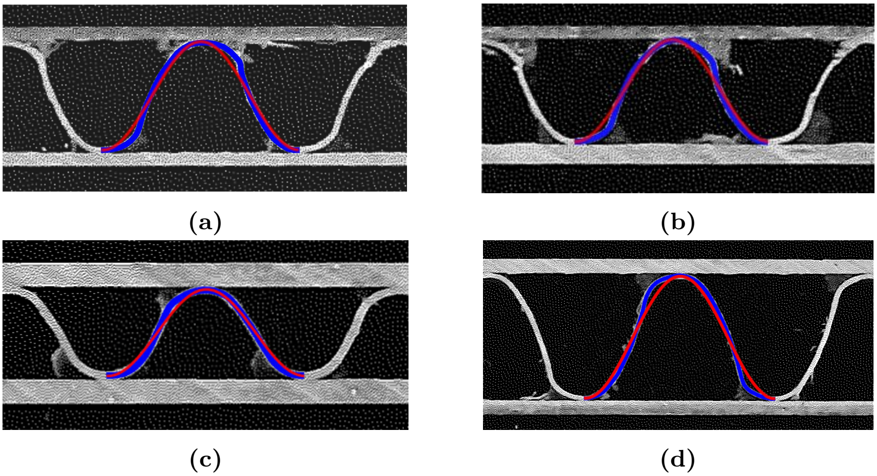

Figure 5.1: Comparison of theoretical sine (red lines) and real curves (blue lines) on the scanned images.

This chapter is organized as follows. Section 5.2 introduces the problem of the differences between real corrugation and supposed sinusoidal profiles. The modal analysis is presented in Section 5.3, with a proper explanation of the methodology, comparison between FE and test data, and discussion of results. Finally, in Section 5.4 a tensile testing is performed to determine experimentally the equivalent Young's moduli in the x- and y-*direction* of the complete sandwich structure.

5.2 Real shape of the corrugated cores

When observing the cross sections of the panels, it is evident that the real shape of the corrugation differs from the theoretical sinusoidal profile. In Figure 5.1, the comparison between sinusoidal and real shape is shown. As visible in the figure, the real corrugation shows also a strongly non-symmetric profile. Therefore, in order to compute the parameters for the equivalent material, it is necessary to use the general formulation proposed in Chapter 3. To represent the shapes with sufficient accuracy, the expression in Fourier series is extended to all terms whose coefficient is greater than 10^{-6}. As an example, to represent each of the two parts of the core profile of the "10_03_10 H11.5" panel, the first 34 series terms are needed. Moreover, to accurately represent the behaviour of the core, the real amplitude of the sinusoid must be considered, thus $H_0 = H_c - t_c$, while the equivalent layer for the core has thickness H_c.

To have an idea of the influence of the real corrugation shape on the equivalent parameters, values obtained from the theoretical sinusoidal shape are compared to those from the real corrugation in Table 5.2. Please note that a plate representation is assumed and only one shear modulus for each plane is considered. To obtain the real geometry of the corrugation, a scan of the panel cross section were made and the image obtained were processed to obtain the midplane curve, as already

Case	E_x [MPa]	E_y [MPa]	ν_{xy} [-]	G_{yx} [MPa]	G_{zx} [MPa]	G_{zy} [MPa]
05_02_05 H6 – Alu 5182-H48						
Sinusoidal	2.757	4.351E+3	2.091E-4	6.697E+2	2.493E+2	1.636E+3
Real	2.326	4.570E+3	1.680E-4	6.376E+2	8.185E+1	1.718E+3
Difference [%]	−15.6	+5.03	–19.7	–4.79	–67.2	+5.01
08_02_05 H6 – Alu 5754-H48						
Sinusoidal	3.450	4.517E+3	2.520E-4	7.447E+2	2.721E+2	1.698E+3
Real	2.972	4.723E+3	2.077E-4	7.124E+2	9.006E+1	1.775E+3
Difference [%]	–13.9	+4.56	–17.6	–4.34	–66.9	+4.53
10_03_10 H6 – Alu 5754-H48						
Sinusoidal	21.44	7.221E+3	9.800E-4	1.447E+3	8.252E+2	2.715E+3
Real	18.33	7.490E+3	8.076E-4	1.395E+3	3.946E+2	2.816E+3
Difference [%]	–14.5	+3.73	–17.6	–3.59	–52.2	+3.72
10_03_10 H11.5 – Alu 5754-H48						
Sinusoidal	1.276	3.752E+3	1.122E-4	4.938E+2	1.611E+2	1.411E+3
Real	1.094	3.926E+3	9.191E-5	4.719E+2	5.259E+1	1.476E+3
Difference [%]	–14.3	+4.64	–18.1	–4.43	–67.4	+4.61

Table 5.2: Comparison of equivalent parameters for theoretical and real corrugation profiles.

Material	Young's modulus [MPa]	Poisson's ratio [ad.]	Density [kg/m^3]
Alu 5754-H48	70300	0.33	2670
Alu 5182-H48	69600	0.33	2670

Table 5.3: Aluminum properties used.

shown in Figure 5.1. Two different constituent materials were considered for the corrugated laminas according to manufacturer's datasheets – see Appendix B. The properties of such materials are given in Table 5.3.

It is evident from Table 5.2 that the most relevant differences are on E_x and G_{zx} which are likely to have a strong influence both on the static and the dynamic behaviour of the structure. In particular, the real shape implies a reduction of about 60% in the G_{zx} parameter and a reduction of about 14% on the E_x parameter. The changes on the other moduli are mainly due to the different length of the corrugation and vary in the range ±4/5%.

It is then obvious that, in order to properly reproduce the behaviour of the real panels, it is important to build the FE equivalent models using the parameters shown in Table 5.2.

5.3 Modal analysis

Modal analysis can be defined as the study of the dynamic characteristics of a mechanical structure. The comparison of predicted structural dynamic behaviour with experimentally measured data is fundamental in validating the modelling of a complex structure as the sandwich panels investigated here. Indeed, if the

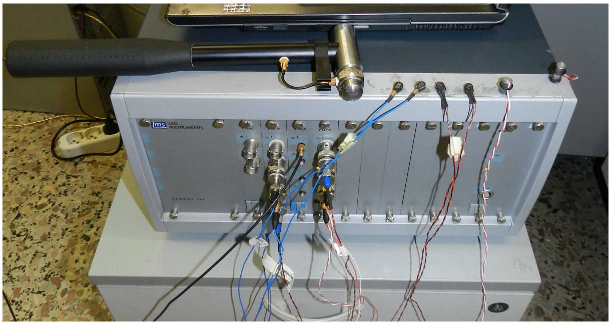

Figure 5.2: Instrumentation for the modal testing.

influence of the core can be usually neglected in static bending conditions, the elastic moduli of the core have a strong influence on mode shapes and frequencies. Moreover, since the developed analytical formulation for the homogenization of the core is based on a static equivalence, it is interesting to investigate the accuracy in reproducing the dynamic behaviour of the structures.

5.3.1 Modal test method

Thanks to the light damping of the structure, an impact testing can be considered a good methodology to obtain the modal characteristics of the panel. The specimen has been subjected to impulses through a hard tipped hammer, Bruel & Kjaer type 8202. The Impact Hammer Type 8202 is an instrumented hammer provided with a built-in Force Transducer Type 8200 with a sensitivity of 0.98 pC/N. The response has been measured through four piezoelectric uniaxial accelerometers. In particular:

- 2 PCB Model 352C22;
- 2 ENDEVECO Model 2250AM1-10.

The sensitivity of the accelerometers is 10 mV/g (1.0 mV/(m/s^2)) and the mass is approximately 0.5 g. The impulse and the responses are acquired with an LMS SCADAS III SC-310 acquisition system and data are pre- and post-processed with LMS Test.Lab. In Figure 5.2, the various instruments used are shown.

A roving hammer technique is used. In this type of testing, the accelerometers are fixed at some DOFs, and the structure is impacted at as many DOFs as desired to define the mode shapes of the structure. The choice of the excitation stations was made by a preprocessing of the FEM models, specifically computing the AutoMAC of the structure to check if the mode shapes defined at the chosen DOFs well represent the mode shapes of the complete FEM model (the first 15 modes were considered). In Figure 5.3 it is shown an example of the results obtained for the set of 16 stations chosen. In Figure 5.4, a scheme with the selected points for the acquisition is shown. Nevertheless, given the rather simple overall geometry of the panel, i.e. a rectangle, the modal testing is more focused on determining

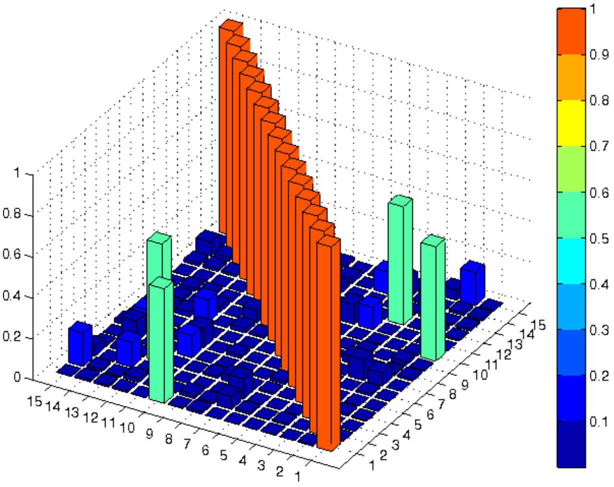

Figure 5.3: AutoMAC matrix for measurement point selection.

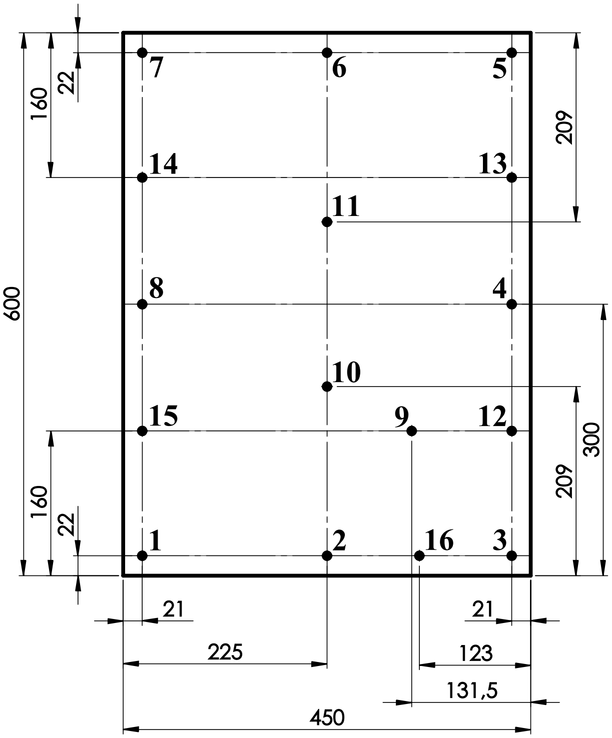
7
6
5
14
13
11
8
4
10
15
9
12
1
2
16
3
22
160
600
160
22
209
209
300
21
21
225
123
131,5
450

Figure 5.4: Positions of stations for the modal testing.

the eigenfrequencies, rather than the eigenmodes of the structures. Finally, the measurement stations were identified by using the Driving Point Residues (DPR):

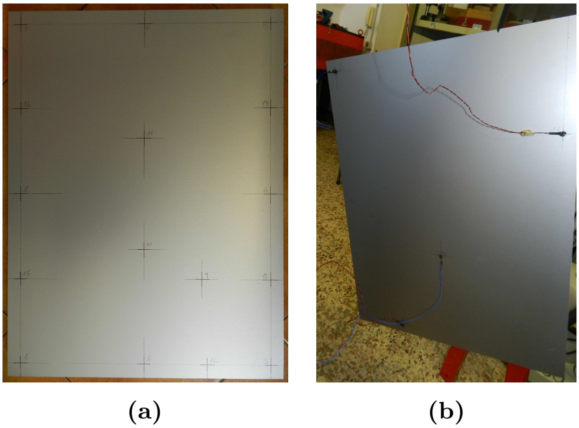
(a) (b)

Figure 5.5: Panel marked and equipped: (a) Front face – excitation points, (b) Rear face – measurement points.

this technique allows determining the more influent points for a given set of modes. The response has been measured by placing the accelerometers at stations 5, 10, 14 and 16 – see Figure 5.4 for point identification. FRFs are computed between each impact DOF and the fixed response DOFs. In order to reduce the statistical variance of a measurement, an averaging process was implemented by repeating 5 times each acquisition. Finally, the estimation of the modal parameters is done by using the LMS PolyMAX tool, which is a method for the identification and selection of poles.

5.3.2 Specimen details

The four panels have an overall dimension of 450 × 600 mm. Each of them was marked in order to easily identify the excitation points, Figure 5.5a. Measurement stations were chosen on the opposite side of the panel, see Figure 5.5b. Free boundary conditions for the modal testing was chosen. The free condition would mean that the structure is, in effect, floating in space with no attachments to ground and exhibits rigid body behaviour at zero frequency. Physically, this is not realizable, so the structure was suspended as depicted in Figure 5.6, using a very soft spring. By doing this, the structure will be constrained to a degree and the rigid body modes will no longer have zero frequency. However, if a sufficiently soft support system is used, the rigid body frequencies will be much lower than the frequencies of the flexible modes and thus have negligible effect. The rule of thumb for free supports is that the highest rigid body mode frequency must be less than one tenth that of the first flexible mode. If this criterion is met, rigid body modes will have negligible effect on flexible modes. In order to modify as less as possible the panel, and consequently its dynamic characteristics, the connection with the springs is done by inserting a very light string in a small hole close to the edge of the panel.

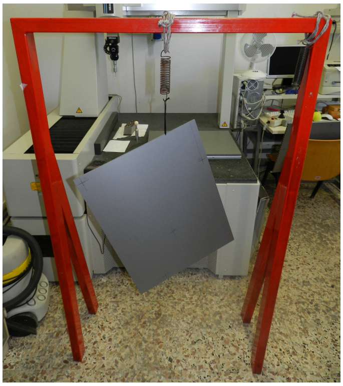

Figure 5.6: Support of the panel for modal testing.

5.3.3 FE models

The FE models to be validated are built using a multi-layer description in Nastran [60] by means of the PCOMP card, which allows defining layers of different material, thickness and/or orientation. This information is then used by the software to compute, assuming perfect bonding between layers, an equivalent shell property. Three layers are considered to represent the two skins and the equivalent layer for the core, whose material properties are derived as shown in Section 5.2. The FE mesh is properly built to have nodes in correspondence of the measurement points of the panel. The first 15 modes are then computed by the standard Lanczos method.

An important note must be done on the shear moduli of the equivalent material for the core layer. It has been shown in Chapters 3 and 4 that the shear moduli in a plane, due to the complex shape of the corrugation, are not equal, e.g. $G_{xz} \neq G_{zx}$. Nevertheless, the FE model requires a unique value in the orthotropic material card MAT8, namely `G12`, `G1Z` and `G2Z`. Therefore, it is important to specify which parameters are used in the following modelling. For the *xz*- and *yz-plane*, G_{zx} and G_{zy} are used respectively, since in the notation used (Section 2.1.1) these parameters are computed by deriving the displacements in the *z-direction*, which is the direction where vibrations are measured by the accelerometers. Consequently, the G_{yx} parameter is chosen for the *xy-plane* to maintain accordance with subscript notation.

Finally, since the total mass is a very important parameter on the values of the natural frequencies, a non structural mass is added to the FE models in order to meet the measured mass of the tested panels. Typically, the difference in the total mass is between 0.1 and 0.2 kg and it can be mainly attributed to the presence of the glue, which is not accounted for in the modelling.

5.3.4 Results

Comparison of results is made by computing the MAC between the experimental and the FE results. Indeed, MAC values are a useful indicator of the similarity between test and analysis mode shapes. It is defined as a scalar constant relating the degree of consistency (linearity) between one modal and another reference modal vector as follows:

$$\mathrm{MAC}(A,X) = \frac{\left|\{\psi_X\}^{\mathrm{T}}\{\psi_A\}\right|^2}{(\{\psi_X\}^{\mathrm{T}}\{\psi_X\}) \cdot (\{\psi_A\}^{\mathrm{T}}\{\psi_A\})} \tag{5.1}$$

where ψ_X and ψ_A are the experimental and FE-based eigenvectors respectively. The value of the MAC is proportional to the correlation of the two mode shapes with a maximum of 1.

Moreover, in order to check the accuracy of the FE models, a comparison of the eigenfrequencies is performed. In the following, results for the four tested panels are shown and compared with FE models built assuming, in the analytical formulation, either the sinusoidal shape – usually referred to as *theoretical* and abbreviated in *"th."* – or the real corrugated profile – usually abbreviated in *"real"*.

05_02_05 H6

MAC comparison for this first panel is shown in Figure 5.7. It is important noting that the FE model which implements the general formulation for real corrugated profiles shows a better behaviour than the sinusoidal corrugated model. Indeed, the mode switch between modes 11 and 12, which can be seen for the sinusoidal shape in Figure 5.7a, is not present in the comparison with the real corrugated core panel, in Figure 5.7b.

Even more relevant to prove the importance of accurately modelling the core profile is the comparison of the eigenfrequencies. In Table 5.4, the experimentally derived values are compared to FE model results. It is important noting that frequencies are listed and sorted according to the experimentally determined values. The FE model with the real shape homogenized core shows an evident greater accuracy than the sinusoidal one. To quantify this difference, a relative error is reported in percentage in the same table, taking the experimental data as reference. Nevertheless, to have an estimation of the overall accuracy for the analyzed modes, the average of the absolute values of such errors is computed. The model with supposed sinusoidal core has mean absolute error of about 6.93%, while for the model with real shaped corrugations this value is 2.39%.

08_02_05 H6

The same procedure was also used for the second panel. The resulting MAC comparison is shown in Figure 5.8. Also in this case a better agreement is found between the experimental results and real corrugated model. The same mode inversion is visible in the sinusoidal case, Figure 5.8a, and avoided in the real corrugation case, Figure 5.8b. Indeed, this panel has a dynamic behaviour quite similar to the previous panel (05_02_05 H6), as it can be seen comparing modal frequencies in Table 5.5 with the previous Table 5.4. Nevertheless, FE models for this panel better predict the modal frequencies. Indeed, computing the average

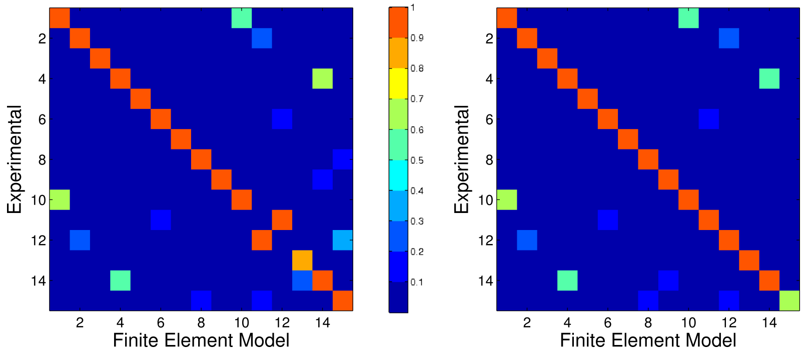

(a) **(b)**

Figure 5.7: 05_02_05 H6 panel. MAC comparison between experimental data and FE models with: (a) Theoretical core, (b) Real core.

Mode No.	Exp. [Hz]	FE th. [Hz]	Th. err. [%]	FE real [Hz]	Real err. [%]
1	91.4	99.4	+8.69	97.2	+6.37
2	121.8	124.4	+2.08	123.5	+1.32
3	212.2	222.2	+4.75	215.2	+1.42
4	219.4	235.4	+7.28	227.9	+3.87
5	269.7	287.0	+6.44	277.7	+2.96
6	349.8	362.1	+3.52	357.9	+2.30
7	426.5	453.3	+6.29	439.0	+2.95
8	434.0	471.8	+8.69	448.3	+3.29
9	542.3	586.8	+8.21	539.3	−0.54
10	600.1	655.7	+9.26	602.7	+0.43
11	658.7	721.3	+9.50	678.3	+2.97
12	673.2	695.9	+3.37	690.0	+2.50
13	728.4	777.0	+6.66	742.5	+1.93
14	773.6	849.5	+9.82	789.6	+2.08
15	957.6	1047.3	+9.37	948.3	−0.97

Table 5.4: Comparison of eigenfrequencies for the 05_02_05 H6 panel.

absolute error as done before, the sinusoidal model leads to a value of 4.48% against the 1.59% of the real core model.

10_03_10 H6

The third panel has thicker faces than the previous ones, 1 mm for each skin, being equal the total thickness of the panel. This implies that the core has a weaker influence on the overall behaviour, even though it is made of a thicker lamina than previous cases, i.e. 0.3 mm. Therefore, the difference between supposed sinusoidal and real shape is less noticeable. This consideration is evident looking both at

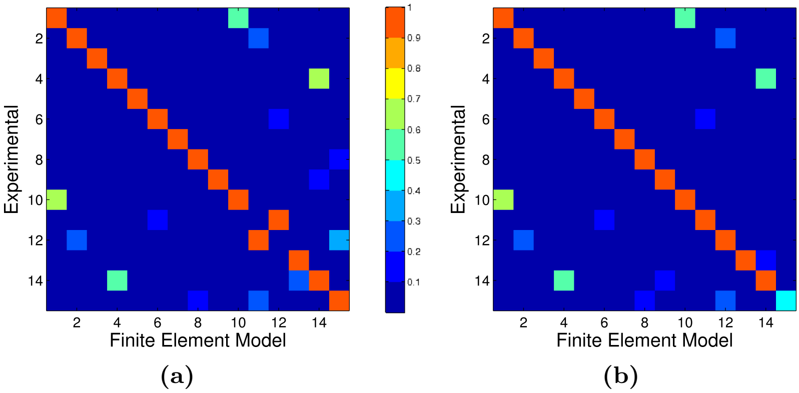

(a) (b)

Figure 5.8: 08_02_05 H6 panel. MAC comparison between experimental data and FE models with: (a) Theoretical core, (b) Real core.

Mode No.	Exp. [Hz]	FE th. [Hz]	Th. err. [%]	FE real [Hz]	Real err. [%]
1	90.5	95.7	+5.78	94.5	+4.48
2	118.6	119.5	+0.73	119.7	+0.86
3	209.1	214.0	+2.37	209.1	−0.01
4	216.1	226.4	+4.78	221.1	+2.30
5	265.5	276.2	+4.04	269.5	+1.49
6	342.6	347.9	+1.55	346.8	+1.22
7	419.7	435.5	+3.78	425.3	+1.34
8	428.1	453.8	+6.01	434.6	+1.52
9	535.8	564.5	+5.36	522.1	−2.56
10	593.0	630.6	+6.34	583.3	−1.64
11	650.8	693.2	+6.52	656.5	+0.88
12	655.7	668.0	+1.88	668.1	+1.90
13	714.2	746.1	+4.47	718.4	+0.58
14	763.1	816.4	+6.98	763.8	+0.10
15	942.4	1005.6	+6.71	914.8	−2.93

Table 5.5: Comparison of eigenfrequencies for the 08_02_05 H6 panel.

the MAC comparison in Figure 5.9 and at the frequency comparison in Table 5.6. From Figure 5.9, almost no difference can be seen in the two graphs and the improvement in the average error is reduced: 0.73% for the real shaped model against the 1.58% of the sinusoidal cored model.

10_03_10 H11.5

The fourth and last panel tested is the most challenging. Indeed, even though the lamina thicknesses are the same (1 mm for the faces and 0.3 mm for the corrugated core), the height of the core layer is much bigger, i.e. 9.5 mm, leading to

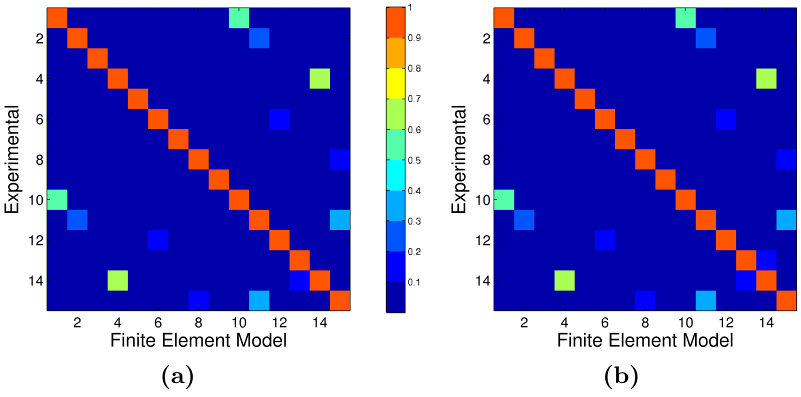

Figure 5.9: 10_03_10 H6 panel. MAC comparison between experimental data and FE models with: (a) Theoretical core, (b) Real core.

Mode No.	Exp. [Hz]	FE th. [Hz]	Th. err. [%]	FE real [Hz]	Real err. [%]
1	92.0	93.9	+2.02	93.5	+1.59
2	116.7	115.6	−0.93	115.7	−0.86
3	210.7	211.4	+0.34	210.2	−0.27
4	219.3	222.6	+1.50	220.8	+0.68
5	268.6	272.0	+1.26	270.2	+0.62
6	337.9	338.0	+0.03	337.7	−0.06
7	422.2	427.3	+1.19	423.9	+0.39
8	439.0	449.9	+2.48	444.3	+1.20
9	560.2	567.1	+1.23	555.0	−0.92
10	621.6	633.4	+1.89	619.7	−0.31
11	644.8	647.7	+0.45	648.0	+0.50
12	670.5	689.4	+2.82	678.0	+1.12
13	720.9	732.8	+1.65	726.7	+0.80
14	796.3	819.3	+2.90	800.9	+0.58
15	973.6	1002.6	+2.98	983.3	+0.99

Table 5.6: Comparison of eigenfrequencies for the 10_03_10 H6 panel.

a very weak core. According to the same comparison of MAC values, Figure 5.10, it is now clear that both the sinusoidal and the real corrugated models are less accurate in predicting the dynamic behaviour of the real panel if compared with previous thinner structures. Nevertheless, the improvement in the accuracy that can be achieved with a proper modelling of the core profile can be seen comparing MAC values for the supposed sinusoidal shape, Figure 5.10a, with the values from the real corrugated model, Figure 5.10b. This consideration is also confirmed by the eigenfrequency comparison, Table 5.7, where a general bigger error in predicting the values can be noticed, especially at higher frequency. Nevertheless, the average error for the real shaped model is 3.49%, drastically reducing the 12.51%

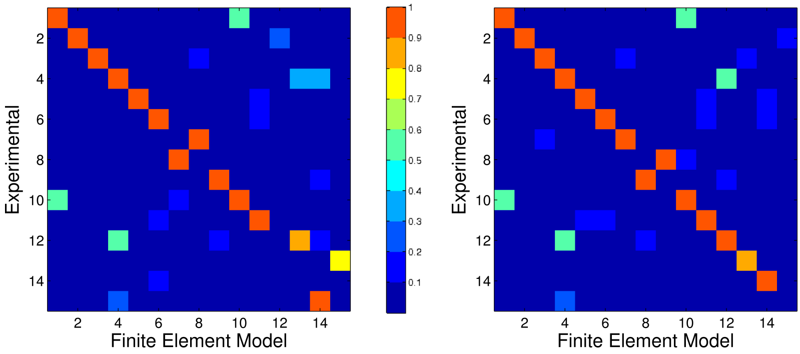

(a) **(b)**

Figure 5.10: 10_03_10 H11.5 panel. MAC comparison between experimental data and FE models with: (a) Theoretical core, (b) Real core.

Mode No.	Exp. [Hz]	FE th. [Hz]	Th. err. [%]	FE real [Hz]	Real err. [%]
1	175.7	185.0	+5.29	177.5	+1.04
2	239.0	237.9	−0.47	237.7	−0.55
3	377.6	407.5	+7.91	365.3	−3.26
4	402.0	428.1	+6.50	397.4	−1.15
5	476.0	519.2	+9.08	464.6	−2.38
6	669.3	680.5	+1.68	674.5	+0.78
7	727.9	820.0	+12.66	708.2	−2.69
8	770.9	818.2	+6.14	763.2	−0.99
9	799.9	962.9	+20.38	738.7	−7.66
10	897.4	1071.6	+19.41	843.3	−6.03
11	1078.9	1223.2	+13.37	1057.1	−2.02
12	1116.2	1327.0	+18.88	1062.1	−4.84
13	1227.3	1608.3	+31.04	1116.9	−9.00
14	1318.4	1688.4	+28.06	1202.4	−8.80
15	1342.5	1432.6	+6.71	1358.0	+1.16

Table 5.7: Comparison of eigenfrequencies for the 10_03_10 H11.5 panel.

of the sinusoidal core model. Please note that, to compute relative differences for the 15th experimental mode, the 16th mode of the FE models is used, since a mode inversion is present between these two modes. It is finally important noting that the thicker the panel, the greater the error is in modelling it as a bidimensional component.

5.3.5 Conclusions

From the above presented comparisons, the importance of a proper modelling of the core shape is pointed out. Even though the accuracy of the equivalent model varies from panel to panel, depending on its characteristics – e.g. weak or strong core – modelling the equivalent core layer starting from a reproduction of the real core profile allows drastically improving the accuracy from a supposed perfectly sinusoidal corrugation. The mentioned differences between the tested panels and FE models can be partially attributed to the hypothesis of perfect bonding between equivalent core layer and panel skins. This assumption, implicitly made when using the PCOMP property in Nastran, leads to a smeared model which is only an approximation. Finally, neglecting of the through thickness effects, such as thickness reduction of the core layer, which are not represented by the FE model, could introduce errors. Nevertheless, other sources of error should be investigated, e.g. the influence of the glue on the overall dynamic characteristics.

5.4 Tensile testing

Testing of average (homogenized) mechanical properties for the sole corrugated core is a very difficult task. The typical properties which are usually “directly” measured are the tension and compression characteristics in the through-thickness direction according to ASTM C297 [63] and ASTM C365 [64] respectively. Moreover, the out-of-plane shear moduli can be determined following test procedure in ASTM C273 [65]. Nevertheless, even for such cases, they are not real *direct* measurements, since the core must be adhesively bonded to two steel blocks which reproduce the coupling and constraint of the core from the skins of the sandwich panel.

Moving to the in-plane properties, typically testing is performed on the complete sandwich structure, even though some example on small corrugated composite lamina exists in the literature, e.g. the tensile test in [22]. Even more often, for tensile testing in the in-plane directions, only face sheets are included, since these elements give the main contribution to the total stiffness. This is true for particularly weak cores, but cannot be stated a priori on all-metal corrugated sandwich structures.

In this section, the tensile testing performed on the sinusoidal corrugated core sandwich panels available is presented and discussed. Please note that the analytical values of the total panel were obtained from those of the different layers by using relations from the CLT, Section 2.1.2.

5.4.1 Methodology

The tensile testing was performed on a servohydraulic testing system, the *MTS810 Material Test System*. The force applied by the machine to the specimen ranges from 25 kN to 500 kN. Nevertheless, due to an amplification factor, for these tests, the full scale value was chosen to be 50 kN. The tests were performed with a displacement-controlled technique and the velocity was approximately 0.067 mm/s. The acquisition was made with a frequency of 20 Hz, thus data were acquired every 0.05 seconds. The value of the applied force was measured from the load cell, while strain was measured by a static strain gauge extensometer (*MTS 632.11F-20*) with a full scale displacement of 3.75 mm. The acquisition was con-

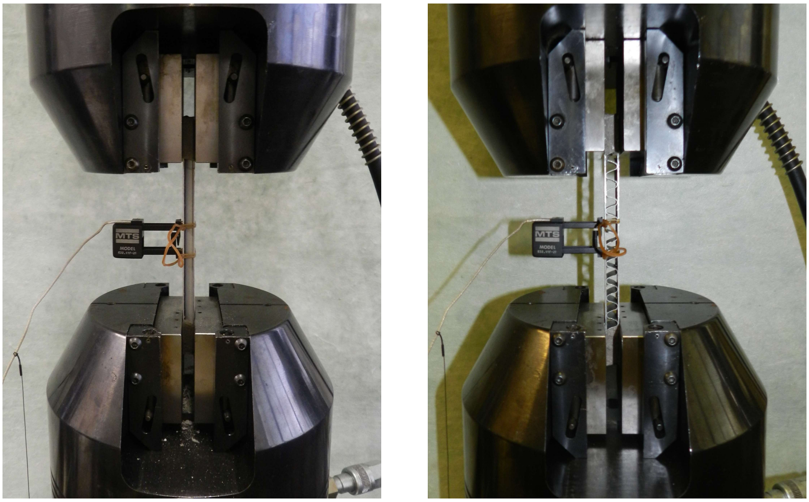

(a) **(b)**

Figure 5.11: Tensile test setup for testing along the: (a) *y-direction*, (b) *x-direction*.

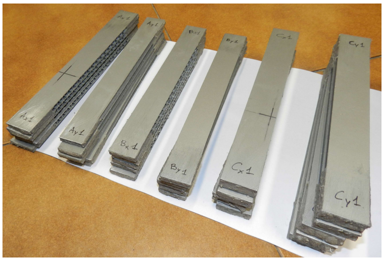

Figure 5.12: Tensile test specimens.

trolled by the control unit *MTS 458.20 Micro Console*. In Figure 5.11 an example is shown of mounted and instrumented specimens for tensile testing in both x- and *y-directions*.

Tests were performed until fracture happened. Nevertheless, the extensometer was removed after a certain displacement was reached (approximately 2.5 mm). Indeed, since the purpose of the tensile testing is to compare the equivalent Young's modulus, only the initial part of the test is needed, i.e. the elastic part. Finally, for each panel, the test was carried out on 5 specimens to account for uncertainties and statistical variance of the measurements – see Figure 5.12 for a view of some specimens.

5.4.2 Specimen details

There is no specific standard which rules the tensile testing for metallic sandwich panels. Therefore, according to the standard ASTM E8 [66], which is valid

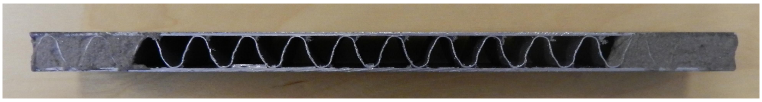

Figure 5.13: Resin reinforced specimens.

for tensile testing of metallic materials, the specimen for the these panels should have a reduced cross-section in the gage area, relative to that of the remainder of the specimen, so that deformation and failure will be localized in this region. Nevertheless, the presence of the corrugation makes the preparation of such a specimen very difficult. Moreover, in the transition area, the corrugated core would be cut in diagonal, so that the forces could be improperly transferred in the core from the grip section to the gage area. For these reasons, in the present test campaign, rectangular specimens are chosen. For this kind of specimens, sometimes it is required the use of tabs in the gripping area with a bevel to ensure a successful introduction of the load into the specimen and the prevention of premature failure due to a significant discontinuity. Nevertheless, ASTM D3039 [67] specifies that the introduction of tabs, either friction or bonded type, is not always required and it suggests to evaluate the need to use tabs by the end results. In this regard, in the present experimental activity, some preliminary tests were carried out to check an acceptable failure location. Therefore, the specimen created has the following dimensions: length of 200 mm in the tensile direction and approximately 25 mm width. The width varies from panel to panel, because specimens for testing in the *y-direction* are built to include a finite number of corrugation periods in their width: 3 periods for the 6 mm thick panels and 2 periods for the 11.5 mm thick panel.

Since the panel is subjected to strong compression in the gripping areas, the core may be crushed in that area, resulting in possible slips and ineffective testing. To avoid this phenomenon, wedge action grips were used and the core corrugations in the gripping areas were filled with a hybrid resin reinforced with Portland cement[1] – see Figure 5.13 for a side view of the reinforced gripping sections.

5.4.3 Results

Comparison of results is shown in Figures 5.14 and 5.15 by plotting the average experimental Young's modulus (black cross in the figures) with the related confidence interval (blue lines) and overlapping the analytical result supposing a perfectly sinusoidal core (magenta circle) and the analytical result computed considering the real shape of the corrugations (red asterisk). In Figure 5.14, the comparison is shown for the four panels in the *x-direction*, while in Figure 5.15, Young's modulus in the *y-direction* is considered. Even though the confidence interval was computed on small data groups, only 5 specimens for each kind of panel in each direction, these graphs are useful for a first understanding. Nevertheless, it is worth noting that experimental values are rather scattered, as it can be seen

---

[1] Fisher. T-Bond Chemical Fixing – ***http://www.fischeritalia.it/prodotti/t-bond***

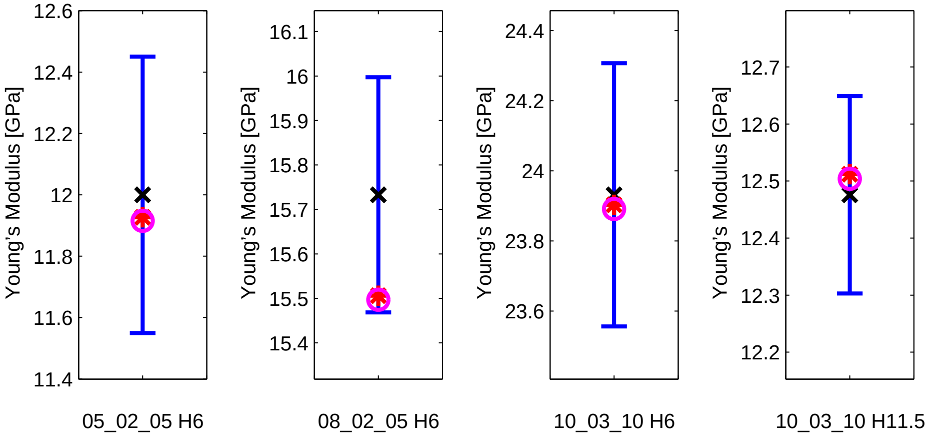

Figure 5.14: Comparison between experimental Young's modulus and analytical values in the *x-direction*.

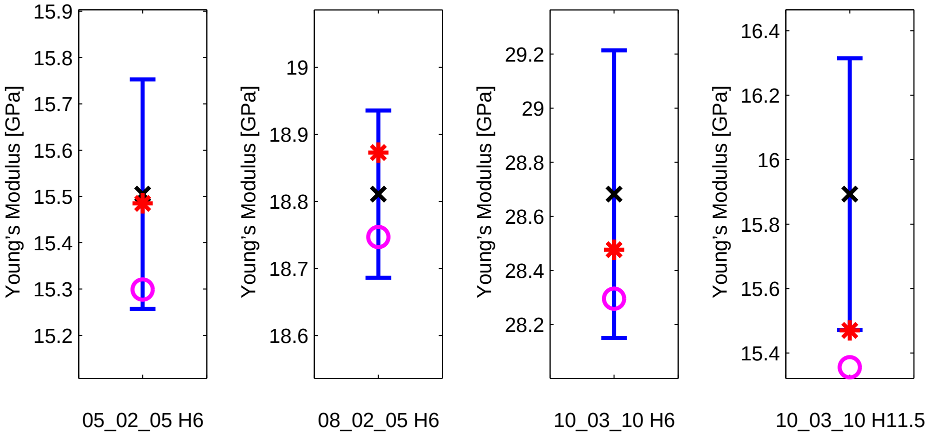

Figure 5.15: Comparison between experimental Young's modulus and analytical values in the *y-direction*.

Panel type and direction	Min. value [GPa]	Ave. value [GPa]	Max. value [GPa]	Std. Dev. [MPa]
05_02_05 H6(x)	11.45	12.00	12.42	324.69
08_02_05 H6(x)	15.51	15.73	16.07	190.36
10_03_10 H6(x)	23.59	23.93	24.30	270.66
10_03_10 H11.5(x)	12.32	12.48	12.70	124.54
05_02_05 H6(y)	15.19	15.89	16.38	178.56
08_02_05 H6(y)	18.67	18.81	18.92	89.94
10_03_10 H6(y)	28.15	28.68	29.20	383.06
10_03_10 H11.5(y)	15.53	15.89	16.38	303.79

Table 5.8: Summary of measured Young's moduli.

looking at Table 5.8 where experimental results are summarized and an estimation of the variability is given by means of the standard deviation parameter.

As it can be seen from the two figures, a very good agreement is found between experimental and analytical values. This observation is validated by computing the percentage errors between analytical and average experimental results, assuming the latter as reference, which are listed in Table 5.9. It is worth noting that, as already visible in Figures 5.14 and 5.15, a slightly greater accuracy is provided by assuming in the analytical formulation the real shape of the corrugation ("Real core" in Table 5.9) respect to a theoretical sinusoidal core ("Th. core" in Table 5.9). In particular, in one case, the 10_03_10 H11.5 panel, the analytical Young's modulus in the *y-direction* supposing sinusoidal shape is out of the confidence interval determined by measurements. Nevertheless, the relative errors are usually comparable. This can be attributed to the smaller influence the real corrugation has on the equivalent Young's moduli of the core layer as shown in Table 5.2, respect to the influence on the shear moduli, which were the main drivers of the differences in the modal analysis. Moreover, the difference between the two corrugations is greater in the *y-direction*. This is mainly due to the fact that in the *y-direction*, the Young's modulus of the complete panel is more contributed by the equivalent core modulus than in the *x-direction*. Indeed, although the main contribution is that of the skins – last column of Table 5.9 – the core has a particular relevance in the *y-direction*, even though it cannot be disregarded even in the *x-direction*.

Finally, errors in the *y-direction* are generally higher than in the *x-direction*. One reason for this behaviour is the influence of the glue, which in that direction gives a non-negligible structural contribution.

5.4.4 Conclusions

The tensile test performed on the available panels has proved the analytical formulation to be an accurate method to estimate the stiffness properties of corrugated core sandwich panels. In general the accuracy of the analytical formulation considering the real shaped core is higher than that of the theoretical sinusoidal corrugation. Nevertheless, the difference between the two core shapes is now less evident, compared to the previous modal analysis, since it results in

Panel type (direction)	Exp. ave. [GPa]	Th. core [GPa]	Th. core Err. [%]	Real core [GPa]	Real core Err. [%]	Skins [GPa]
05_02_05 H6(x)	12.00	11.92	−0.71	11.93	−0.61	11.60
05_02_05 H6(y)	15.51	15.30	−1.33	15.49	−0.13	11.60
08_02_05 H6(x)	15.73	15.50	−1.50	15.51	−1.44	15.17
08_02_05 H6(y)	18.81	18.75	−0.34	18.87	+0.33	15.17
10_03_10 H6(x)	23.93	23.89	−0.17	23.90	−0.12	23.43
10_03_10 H6(y)	28.68	28.30	−1.35	28.48	−0.72	23.43
10_03_10 H11.5(x)	12.48	12.50	+0.23	12.51	+0.29	12.23
10_03_10 H11.5(y)	15.89	15.36	−3.38	15.47	−2.66	12.23

Table 5.9: Comparison equivalent Young's moduli for the complete tested panels.

a smaller difference in the Young's moduli of the complete panels. This is due both to the smaller influence of the shape on the core Young's moduli, compared to shear moduli, and to the smaller influence of the equivalent core to the total panel behaviour. Moreover, the error in the *y-direction* is bigger than that in the *x-direction*. The reason behind this phenomenon has probably to be found in the effect of the presence of the glue.

5.5 Concluding remarks

The present chapter has shown the results of an experimental campaign set up on available aluminium sandwich panels with sinusoidally corrugated cores.

The first observation on the core of those panels has shown a corrugation shape which differs from the supposed theoretical sinusoid. The effect of this difference has been investigated and it has been shown that the real corrugation implies a reduction of several parameters with a particular influence on one transverse shear modulus, which is decreased by around 60%. Therefore, in the following comparison with experimental results, both the sinusoidal shape and the real corrugation are assessed.

The first test consists in a modal analysis of the four different available panel configurations. The first 15 modes have been extracted and compared with results from FE models where the complex shaped core was represented as an equivalent homogeneous layer, according to Sections 3 and 4. Results have shown the model built with the analytical formulation to be very representative of measurement data. Moreover, the importance of the general analytical modelling proposed in Section 3 is proved by the greater accuracy this formulation may achieve thanks to the modelling of the real shape of the corrugated core.

The second test is a tensile testing on the complete panels in the two main directions of the panel plane. In both directions, the analytical formulation has shown a good accuracy in predicting the mechanical properties of the panel. In particular, the analytical formulation for the real shape has provided a better accuracy than the theoretical sinusoidal profile, even though the importance of the real shape is lower than in the modal analysis.

Further development of the present experimental analysis would require more specimens to be tested in the tensile testing, in order to be able to statistically analyze data and achieve more significant results. Indeed, the variability of available tensile data was sometimes too high to have a good comparison term for the analytical modelling. Moreover, the specimens for tensile tests are obtained, for each configuration, from only one panel, which is the only one available and already used for the experimental modal analysis. Therefore, it could be interesting to investigate the variability of the mechanical and modal characteristics among different panels. Finally, the presence of the glue, both on the static and modal behaviour should be investigated more deeply, since it is likely to influence the global properties.

Chapter 6

Multidisciplinary optimization

6.1 Introduction

Nowadays, the transportation industry is increasingly striving to reduce the weight of products in order to reduce fuel consumption and consequently emissions. The innovative materials applied include sandwich panels with cores in foam, honeycomb materials or other complex structures. However, when using such structures in vehicles, for example in train car bodies, different functional requirements have to be respected in the design – structural, crash, acoustic, thermal, etc. The conventional consequential design cycle in which the draft design is assessed versus all relevant functional requirements one after another, is still an industry standard, but is time-consuming, in particular when complex design solutions in compound materials are being developed and assessed. One important reason is that different functional requirements are frequently in conflict with each other [68, 69]. In this context, a robust and reliable Multi-Disciplinary Optimization (MDO) technique is very attractive to simultaneously account for several critical design requirements. At present, numerical optimization techniques are frequently used in structural design, but their application to multidisciplinary problems is still very limited in the industrial practice, even for relatively simple structures as the sandwich panel analyzed here. This can be partially attributed to two requisites that are needed while dealing with optimization:

- all relevant design requirements must be given in a mathematical form which represents the physics of the problem in a correct way;
- the design parameters needed can be calculated with reasonable computational effort.

Fulfilling these requisites is rather easy when dealing with static load simulations, but not when more complex simulations are needed, e.g. crash, fatigue and acoustic simulations. Indeed, in acoustics, it is not straightforward to choose a model that both represents the physics well enough and at the same time is quick to solve. Moreover, some of the optimization methods at hand require the constraint parameter to have certain properties, e.g. continuity or smoothness in the design space. To fulfil these requirements, the acoustic parameter chosen to

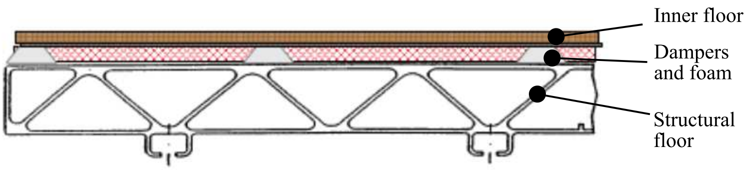

Figure 6.1: Typical train floor structure.

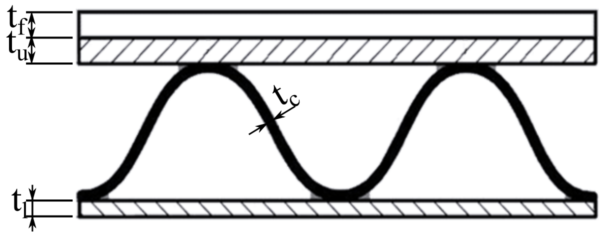

Figure 6.2: Inner floor cross section and optimization variables.

evaluate constraints in an optimization process is sometime different from what is typically used in the industrial practice. Nevertheless, acoustic constraints are usually difficult to handle and the behaviour of the optimization method is strongly influenced by their presence.

The main aim of this chapter is to show how a properly set-up optimization process can lead to a desired design of a corrugated core sandwich panel with predefined requirements. The use of optimization processes, because of their iterative nature, is possible only thanks to the homogenized model proposed in Chapters 3 and 4. Indeed, as shown in Section 4.5, to compute the Transmission Loss (TL) of each panel configuration represented with a 3D FE geometry would require about 14 hours, while the simplified model is solved in less than 2 minutes on a standard PC.

The system investigated in this chapter is the upper part of a built-up train floor, denoted inner floor, as shown in Figure 6.1, which is composed of an aluminum sandwich structure – with a sinusoidal corrugated core – and a rubber layer, denoted floor cover (FC), as shown in 6.2.

Moreover, this chapter aims at comparing and assessing different approaches in handling problems with a chosen acoustic constraint with particular attention to the required number of iterations and consequently the computational time.

To do that, an MDO process is applied to an industrial case problem. The mass per unit area of the floor component, i.e. the inner floor, is minimized while both static and acoustic constraints are applied. A maximum deflection is imposed as mechanical constraint under point and distributed loads. The acoustic constraint applied is the minimum weighted sound reduction index (R_w): an integer value typically stipulated for this kind of structures in view of its simplicity, even though it originates from building acoustics. A parametric study on the acoustic constraint parameter is needed to effectively set up the optimization problem and choose the optimization algorithms. Finally, the optimal structure configurations obtained with the different algorithms are compared and discussed.

The chapter is organized as follows. In Section 6.2 the used optimization methodologies are introduced. The optimization process setup is explained in Section 6.3, while results obtained with the various methodologies are shown in Section 6.4 and discussed in Section 6.5.

6.2 Methodology

The performance of both GB and non-GB methods is benchmarked in the presence of a complex acoustic constraint. Moreover, different constraint handling approaches are considered. The methods used in this paper are based on MATLAB algorithms and will be briefly described in the following sections.

6.2.1 Active-set optimization

The GB method used here is included in the FMINCON function [70]. This function attempts to find a constrained minimum of a scalar function of several variables starting at an initial estimate. Three different methods are available in the function:

1. Trust-region-reflective optimization: does not allow using inequality constraints; it uses the preconditioned conjugate gradients (PCG) algorithm [71];

2. Interior-point optimization: mainly developed for convex problems [72];

3. Active-set optimization: uses a sequential quadratic programming (SQP) algorithm [73]. In this method, the function solves an approximate quadratic programming (QP) sub-problem at each iteration. An optimization problem is called quadratic when there is a quadratic objective function that is linearly constrained.

The third method has been used in this work, since the investigated problem involves inequality constraints and convexity is not ensured, due to the presence of acoustic constraints. The approximation of the problem at each sub-step is performed using a quasi-Newton method, in particular the Broyden-Fletcher-Goldfarb-Shanno (BFGS) method [74]. A more detailed explanation of all techniques and algorithms can be found in [75]. Constraints are handled in this algorithm with the Karush-Kuhn-Tucker (KKT) equations [76, 77]. Without going into detail, it is sufficient to mention that these equations add conditions (necessary conditions) to the derivatives of the functions involved. In particular, the stationarity condition, Eq. 6.1, is a generalization of the method of Lagrange multipliers, which was developed only for equality constraints. In case of no inequality constraints, the KKT conditions turn into the Lagrange conditions, and the KKT multipliers μ_i, are called Lagrange multipliers.

$$\nabla g(\boldsymbol{x}^*) + \sum_{i=1}^{m} \nabla G_i(\boldsymbol{x}^*) = 0 \tag{6.1}$$

In case of non-convex problems, GB methods assure the convergence only to a local minimum. Therefore, to extend their usage and increase the probability of finding a global optimum, different approaches have been developed. One of the simplest is the Multi-Start (MS) method, which consists in performing the optimization with a GB approach from multiple starting points randomly generated in the design space. Finally, the local minimum with the smallest OF value is considered as the global minimum.

6.2.2 Genetic Algorithm optimization

For the non-GB class of methods, Genetic Algorithm (GA) has been chosen to solve the optimization problem. GA seeks the solution of a problem in the form of multiple design variable vectors (individuals) by applying operators inspired on biological evolution: mutation, crossover, recombination and selection.

There are different ways to include the constraints in GA; in this work two methodologies have been used.

- Penalty Function Method (PFM) [78]. It replaces the constrained problem by a series of unconstrained ones. Constraints are directly included in the OF by adding a term that consists of a penalty parameter σ_i and a measure of the constraint violation (Eq. 6.2). Penalty parameters can be static or dynamic over the generations [79, 80]. Thanks to incorporating the constraints in the OF, no special handling technique is needed. On the other hand, its main drawback is the lack of automation in defining penalty factors.

$$\Phi(\boldsymbol{x}) = f(\boldsymbol{x}) + \sum_{i=1}^{m} \sigma_i \max(0, G_i(\boldsymbol{x}))^2 \tag{6.2}$$

- Augmented Lagrangian Genetic Algorithm (ALGA) [81, 82] is able to solve nonlinear optimization problems and it is the default method to handle constraints in MATLAB for GA. The ALGA method is a combination of GA and Augmented Lagrangian Method (ALM). ALM is a method to include constraints in the OF similar to Penalty Method (PM) in that it also replaces a constrained problem by a series of unconstrained problems, but adding an additional term designed to mimic a Lagrange multiplier.

Typically, these methods are considered one of the solutions for global optimization problems. It means that they are supposed to be able to find the global minimum of the problem. Additionally, they are claimed to not depend on the type of objective and constraint functions. Nevertheless, several criticism are arising regarding their features. In particular, GAs may have a tendency to converge towards local optima or even arbitrary points rather than the global optimum of the problem [83, 84]. Moreover, their main drawback is a relatively poor convergence rate compared to GB methods. Therefore, when the calculations involved

Parameter	Value [mm]
Floor cover thickness (tf)	2
Glue thickness	≈1
Upper face thickness (tu)	1
Lower face thickness (tl)	1
Core sheet thickness (tc)	0.3
Total height	6
Sinusoid period	8.5

Table 6.1: Inner floor dimensions.

	t_f	t_u	t_c	t_l
Min values	0.10	0.10	0.10	0.10
Commercial values	2.00	1.00	0.30	1.00
Max values	5.00	5.00	1.00	5.00

Table 6.2: Design variable ranges.

are time consuming, like for crash and acoustic simulations, it cannot be stated that non-gradient-based methods are the best choice.

6.3 Optimization set-up

As already mentioned in the introduction, the investigated structure consists of an aluminum sandwich panel with sinusoidal corrugated core and a rubber layer glued on the top. The typical dimensions of the commercial panel, which is typically used in this railway application, are listed in Table 6.1 – see Figure 6.2 as reference.

On this structure, the set-up optimization process consists of a mass minimization with both structural and acoustic constraints. In particular, the process has the following features:

- Objective function: mass per unit area of the panel [kg/m^2];
- Structural constraint: imposed maximum deflection, 2.5 mm, under a distributed load w, 5000 N/m^2, and a point load P equal to 750 N (high heels load case);
- Acoustic constraint: weighted sound reduction index $R_w \geq 30$ dB;
- Variables: thicknesses of the four layers, t_l, t_c, t_u, t_f (see Figure 6.2). The bounds for the chosen variables are listed in Table 6.2, together with the commercial configuration values.

The preliminary nature of this study is evident since only some of the possible constraints and variables are included in the process. The choice of types and values of the constraints has been made based on standard railway design specifications for these components.

In the following section, the imposed constraints are discussed into detail.

6.3.1 Structural constraints

For the computation of the structural constraints, an analytical method was chosen to determine the displacement of the floor in the two load cases. With this kind of loads it is very easy to analytically determine the maximum deflection, representing the structure as a beam with the classical Euler-Bernoulli beam theory, simply computing the bending stiffness per unit width D (safe approach, since D for beams is lower than for plates). Nevertheless, this theory neglects transverse shear deformations, since for standard beams, with relatively high shear stiffness, their contribution to the total deformation can be disregarded. For sandwich beams this is not always true and it is necessary to account for these deformations, using the Timoshenko beam theory. The present analytical modelling of the static behaviour takes into account also the transverse shear stiffness per unit width S of the structure. The equations for the maximum deflection are listed in Table 6.3. Please note that the point load of 750 N was scaled to 1.5 N to consider the reduced width of the beam – 1 mm – instead of the 500 mm of the commercial panel.

To determine the parameters needed, it has been considered the real application situation for the inner floor:

- Beam length: 750 mm. It is the distance between the rubber elements on which the inner floor is supposed to rest;
- Orientation: the beam is oriented with the length along the extrusion direction. This is important because of the strong orthotropic behaviour of the core;
- Boundary conditions: clamped edges, to ensure continuity between two adjacent regions of the inner floor.

Moreover, knowing the sinusoidal shape of the corrugated core, it is possible to compute both the bending and the shear stiffness, respectively D and S. The limit for the maximum deflection under these two load cases has been set on 2.5 mm.

6.3.2 Acoustic constraints

The model used for computing the acoustic constraint has a length of 1.4 m in the *x-direction* and 1.3 m in the *y-direction*, reproducing the typical test panel dimensions. The periodic theory has been applied as in Section 4.5 thanks to the properties of the panel, using VA One [85] with its Periodic Subsystem Tool, allowing its reduction to a smaller sample: 127.5 mm by 111.1 mm.

The inner floor is represented as a multilayer panel using results from Chapter 4. The FE model for the equivalent layered plate is built with shell elements

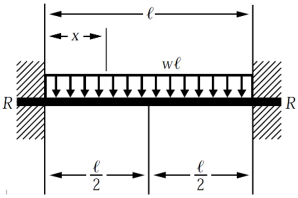	For $x = l/2$ and distributed load w: $\delta_{max} = \frac{wl^4}{384D} + \frac{wl^2}{8S}$
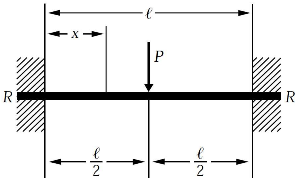	For $x = l/2$ and point load P: $\delta_{max} = \frac{Pl^3}{192D} + \frac{Pl}{4S}$

Table 6.3: Analytical deflection formulas using Timoshenko beam theory.

using the standard PCOMP card in Nastran [60] with three layers representing respectively: the lower face of the sandwich panel, the equivalent core layer and the upper face. Due to the extremely low stiffness property of the rubber floor cover, this layer has been included in the model as an additional non-structural mass (NSM). The NSM also compensates the absence in the model of the glue between the sandwich panel and the rubber coating.

As acoustic constraint for this structure, the commercially most common parameter for panels is used, i.e. the weighted sound reduction index R_w [86]. This parameter, first defined for the use in buildings, is quite common also in the railway industry, because it describes with a single number the acoustic performance of a panel, i.e. the frequency-dependent airborne sound insulation spectrum. It is defined as the integer value, in dB, of a reference curve at 500 Hz after shifting it in accordance with the method specified in [86]. The usage of a discrete valued constraint function characterized by integer values would discard gradient-based methods. However, the definition of this parameter can be slightly modified to include a certain number of decimals, $O\left(10^{(-4)}\right)$, and allow computing the partial derivatives.

The functions involved in a gradient-based optimization process should also have another characteristic: the smoothness with respect to design variables. To investigate this aspect of the acoustic constraint function, two parametric studies were carried out, determining the TL of the test panel, while varying two design variables: the thickness of the upper face of the sandwich panel and the thickness of the core sheet. The other two parameters were not considered, since:

- the effect of the thickness of the lower sheet is supposed to be equal to that of the upper one;
- the floor cover, considered as a non-structural mass, mainly shifts the TL

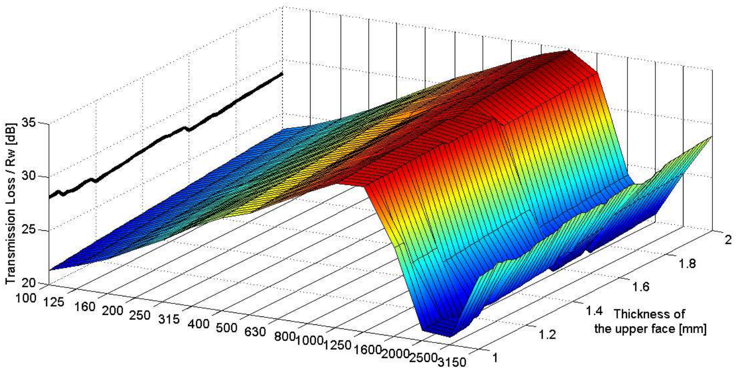

Figure 6.3: Parametric study on the TL spectra: influence of the t_u variable.

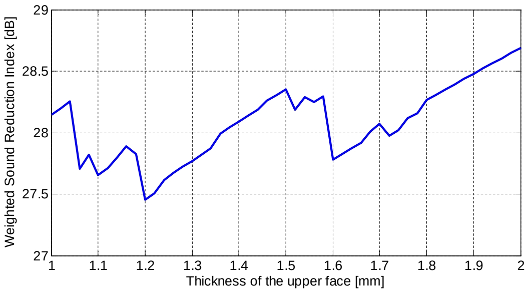

Figure 6.4: Parametric study on R_w: influence of the t_u variable.

curve of the sandwich panel without changing its shape – if the added mass is relatively small compared to the total mass per unit area.

In Figure 6.3, the TL spectra are plotted for different face thicknesses, ranging from 1 to 2 mm with a step of 0.02 mm, while in Figure 6.5, the spectra are shown varying the core sheet thickness from 0.02 to 1 mm with the same step size. The two figures show also – black curves – the trend of the modified R_w when varying the two design variables, better represented in Figure 6.4 and Figure 6.6.

The non-smoothness of the R_w can be partially attributed to variations around the coincidence frequency, probably a result from the averaging in third octave bands. One possibility to avoid this phenomenon could be to consider narrower frequency bands, but a new definition of the R_w would be necessary since the ISO standard [86] only defines it for octave and third octave bands. A modified definition in sixth octave bands, has shown a smoother behaviour running a parametric study – Figure 6.7 – varying the upper face thickness; similar results can be obtained varying the core sheet thickness. Nevertheless, to maintain the acoustic parameter as close as possible to the standardized one, the R_w in the present study has been computed in third octave bands, only allowing decimal addition.

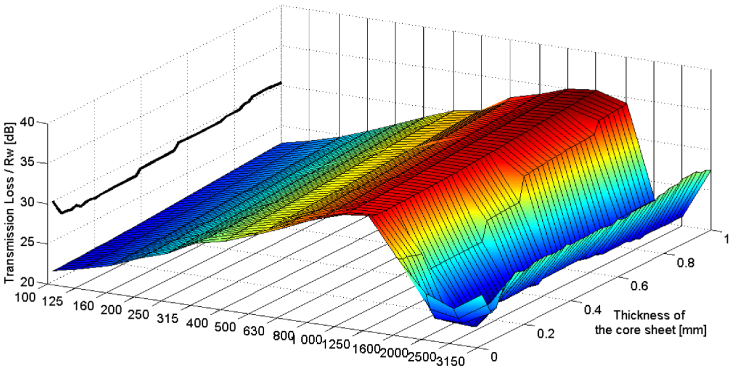

Figure 6.5: Parametric study on the TL spectra: influence of the t_c variable.

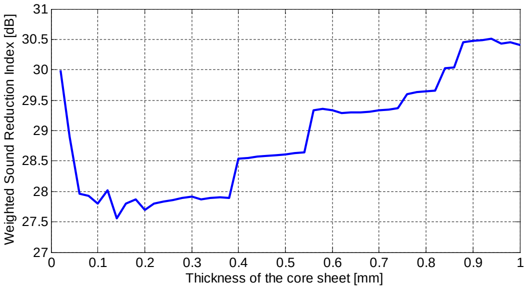

Figure 6.6: Parametric study on R_w: influence of the t_c variable.

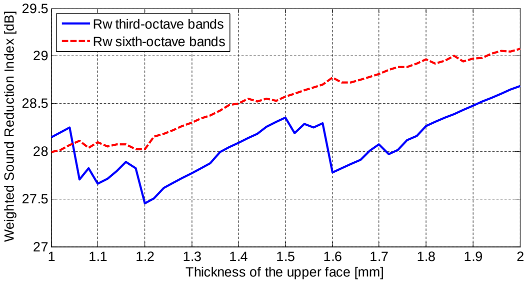

Figure 6.7: R_w with narrower bands.

	t_f [mm]	t_u [mm]	t_c [mm]	t_l [mm]	Mass [kg/m^2]
GB Optimum	1.05	1.53	0.10	1.53	10.90
MS Opt. 1	1.05	1.52	0.10	1.55	10.90
MS Opt. 2	0.10	2.68	0.10	0.87	10.69
ALGA Int. Rw	1.11	1.55	0.10	1.51	11.00
ALGA Mod. Rw	1.49	3.08	0.34	0.71	14.47
GA - PFM	0.14	0.85	0.10	2.71	10.80

Table 6.4: Optimal results obtained with the various techniques.

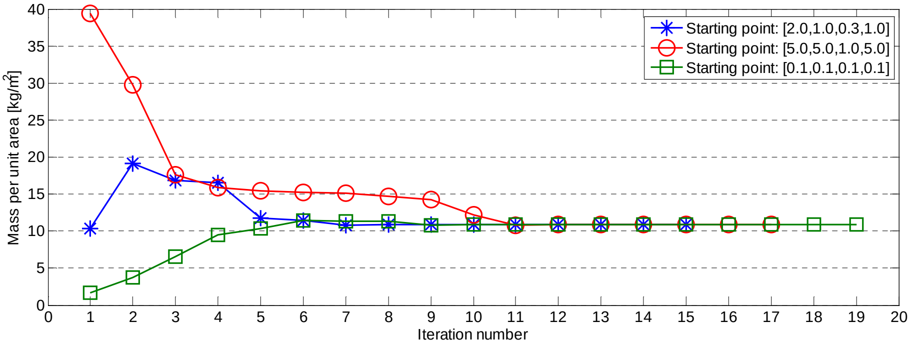

Figure 6.8: Objective function trends for the GB method.

6.4 Optimization results

In Table 6.4, the optimum configurations obtained with the various algorithms are listed.

For the GB method, three different starting points have been initially chosen to run the algorithm: the commercial configuration and two configurations corresponding to the upper and lower bounds of the design variables, see Table 6.2 for values and Figure 6.8 for OF trends. It can be noted in Figure 6.8 that, even though the number of iterations differs from case to case, the optimal solution is the same with all starting configurations. This may suggest that the solution found is a global one.

Nevertheless, running the optimization with an MS approach with six randomly chosen starting configurations and the same settings of the GB algorithm, has led to different results, as it can be seen in Table 6.4. Moreover, two different optima were obtained. This can be attributed to the discontinuous behaviour of the R_w, which strongly affects the convergence of the GB algorithm. Indeed, in the MS process, only four out of the six runs converged to a solution. The first optimum obtained with the MS approach, obtained in only one run, is very similar to that from the GB single start process: in fact, the mass is exactly the same but distributed in a slightly different balance between the two faces. On the other hand, the second optimum is a new solution, even better than the previous one

Optimization method	Function count	Iterations/ Generations	Optimum OF value	Max deflection [mm]	Rw [dB]
GB – single	150	19	10.90	2.50	30.00
GB – MS	1543	199	10.69	2.50	30.00
ALGA Int. Rw	6280	3	11.00	2.50	30.05
ALGA Mod. Rw	8480	4	14.47	2.28	29.99
GA – PFM	3120	78	10.80	2.51	30.02

Table 6.5: Comparison of the different optimization methods.

with 10.69 kg/m^2 instead of 10.90 kg/m^2.

Moving to GA optimization, one of the advantages of these algorithms is that there is no requirement regarding the constraint functions. This implies the possibility for GA to include discrete valued functions too. For this reason, the first attempt with GA considered the acoustic constraint as it is originally defined, i.e. as an integer value. First, GA with Augmented Lagrangian Method (ALGA) to handle constraints was used. The size of the population was set to 40 individuals with a random initial population spread over the whole design space. The optimal solution from this process can be seen in the fourth row of Table 6.4. The result configuration is similar to the GB methods, in the first row of Table 6.4.

Trying to include the modified version of the acoustic parameter – as it was defined for GB methods – led to a much worse situation than the previous ones in terms of OF value (fifth row of Table 6.4, “GA Mod R_w”). The reason of such an oversized configuration is that, if the acoustic constraint is “exactly” satisfied with an R_w of 30 dB, the static constraints are satisfied over the limit: 2.28 mm of maximum deflection under distributed load, instead of 2.5 mm.

Finally, the other constraint handling approach for GA was tested, i.e. GA in combination with PFM. The same population size of ALGA algorithm was used, i.e. 40 individuals. In the present problem, penalty factors were chosen to be constant over the iterations and set equal, for every constraint, to 100. Results for this computation are shown in the last row of Table 6.4. The optimal configuration is similar to the one obtained from MS approach to GB.

6.5 Discussion

One of the most important characteristics of an optimization algorithm that has to work with time-consuming computations is its efficiency. An efficient algorithm has a faster convergence rate and the lowest number of calculations within one design iteration. It means that the algorithm should converge to the optimum using as few function evaluations as possible. In this regard, Table 6.5 compares the methods used considering the number of evaluations done and the needed iterations/generations.

The following comments can be made:

- GB method is the fastest even when using the MS approach;

- the best optimum, candidate to be the global one, is obtained with the MS approach;
- every optimum is a feasible configuration since constraints are satisfied: please note that tolerance on constraints was set to 0.01 (mm or dB);
- the difference between results from single- and multiple-start GB can be due to the symmetric configurations of the sandwich panel chosen in the single run GB;
- GA with penalty functions seems to converge to the same configuration of the MS – even if with exchanged face thicknesses – but with a lower accuracy: indeed, constraint values for the best individual are not exactly the limit values imposed, as it is for MS optimization;
- the mass per unit area for all the local optimal solutions is greater than the initial value for the commercial panel, 10.3 kg/m^2; the needed mass increment is due to the infeasibility of the initial configuration, that has an R_w of 28 dB and a maximum deflection of 4.35 mm, not satisfying the requirements;
- ALGA, mainly due to the use of simulated Lagrangian multipliers allows drastically reducing the number of generations (compared to GA with penalty function method), but it needs too many function evaluations in total;
- ALGA with the integer R_w converges to a configuration similar to a local optimum obtained with GB methods, which is not the best one, but still it is much better than the one obtained using the modified definition of the R_w.

The phenomena observed on the ALGA method needs to be further investigated, but the time needed for the whole process with this method, approximately two weeks for the 6280 function evaluation, suggests the method to be discarded. In addition to this, GA in general has shown bad performance also in the quality of the final solution. In particular, difficulties in satisfying the constraints were observed both using PFM and ALGA.

Moreover, it can be stated that a single run GB approach is not satisfactory, but it was very useful to quickly adjust the setting parameters needed as input to the algorithm for the following MS optimization, mainly the constraint and objective function tolerances.

It is worth noting that in the global optimal configuration, the sandwich panel is an asymmetric structure having different upper and lower face thicknesses, see Table 6.4. Mass per unit area being equal, moving from two symmetric faces to an asymmetric configuration reduces the bending stiffness of the panel, but improves its transmission loss properties. To prove this, in Figure 6.9, the TL spectra are computed for the global optimum and for a configuration with same total mass, but with equal thickness of the two faces of the sandwich panel, i.e. 1.78 mm.

The curve for the asymmetric configuration shows a less pronounced peak in the coincidence region, increasing the R_w of 0.9 dB. This phenomenon is probably due to a decoupling of the eigenmodes of the faces. Please note that the difference

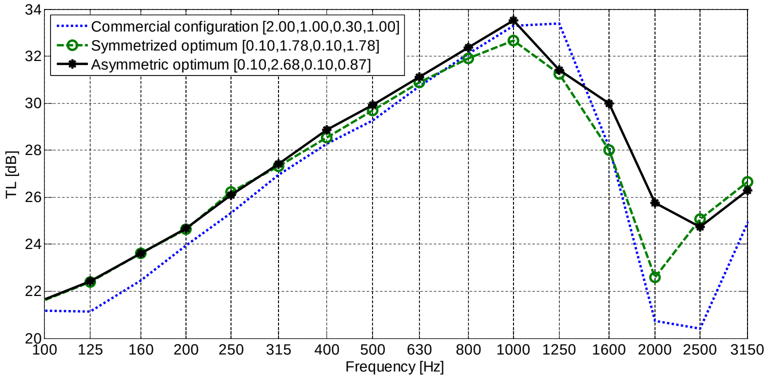

Figure 6.9: TL comparison: asymmetric and symmetrized configurations.

between the two spectra is well captured by the chosen acoustic parameter R_w, while other simpler parameters typically used, as the value of the TL at 500 Hz, would not have been able to distinguish between the two configurations.

6.6 Conclusions

The present chapter has shown that multidisciplinary optimization, if properly set up, can be a powerful tool to tailor a structure to the design needs. The subject of the optimization process was the inner floor of a train, a rather simple structure composed of a corrugated core sandwich panel with a rubber floor cover. The sandwich panel was modelled taking advantage of the analytical formulation developed in Chapter 4.

First, the optimization process has been introduced showing its multidisciplinary nature that combines structural and acoustic requirements. The parameter used to represent the acoustic behaviour of the panel is a modified version of the weighted sound reduction index R_w, to include a certain number of significant digits for computation of derivatives. A parametric study has been carried out on it, showing a strong non-linearity and discontinuity with respect to the design variables that could affect the performances of GB optimization methods.

The optimization problem has been solved with different algorithms: a GB method, based on sequential quadratic programming, and GA. The GB optimization has been run with both single- and multi-start approaches, while for GA, different constraint handling methods have been tried: ALGA and PFM. Summarizing obtained results, it has been observed that ALGA is the less efficient method, since it requires much more function evaluations than the others. Moreover, the result obtained from ALGA is better considering integer valued acoustic constraint, but still distant from the best optimum obtained with the other methods.

On the other hand, GB methods with a multi-start approach are shown to be the best solution for this problem, since they have given the best local optimum, supposed to be the global one, with the best accuracy in satisfying constraints and a high efficiency. In fact, MS has required half the function evaluations of the PFM for GA. The optimization with the latter converged to a solution close to the one obtained with the GB method, but with a lower accuracy in satisfying constraints. Finally, please note that the discontinuous behaviour of the acoustic constraint, observed in the preliminary parametric study, has influenced the number of converging runs in the MS optimization, but not the quality of the solution obtained, that is the best optimum.

The global optimum obtained with the MS approach is an appealing solution because the thickness of the rubber floor cover has reached its minimum value. Since the main effect of this kind of layers is to improve the acoustic behaviour of the structure, a more efficient and multifunctional structure has been obtained. Moreover, this proves that adding insulating material is not the best way of reaching acoustic requirements and that better solutions can be found with multidisciplinary optimization processes. Nevertheless, the importance of a simplified modelling technique as the one presented in Chapters 3 and 4 is evident looking at the number of function evaluations which are needed even for a pilot study as the one proposed.

Finally, it can be concluded that the task for this optimization, consisting in increasing the weighted sound reduction index by 2 dB and the bending stiffness by 70%, has been successfully reached at the cost of only 4% mass increase.

Chapter 7

Conclusions

The aim of the work presented in this dissertation was to develop efficient and accurate modelling techniques to properly represent the static and acoustic (dynamic) behaviour of all-metal corrugated cores sandwich panels which would allow the inclusion of these structures in MDO processes.

The relevance of this work is justified by the importance metal sandwich panels are increasingly covering as multi-functional components in many industrial areas, e.g. elements in train walls and floors, in electric car floors or in ship decks. Nowadays, one of the main drivers in the industrial design is component weight and competitive solutions are enabled thanks to the high stiffness-to-mass ratio of such panels, especially under bending conditions.

Among all sandwich panels, corrugated core structures are an interesting alternative to other core topologies that is being increasingly used in the transportation industry. This is mainly due to their characteristic of providing good structural performances with very limited total thicknesses. In particular, an appealing solution for corrugated cores is the sinusoidal shape, which originates from cardboard panels. Nevertheless, the greater mechanical properties of metals, compared to paper, allows a greater customization of such panels and a wider applicability range in various fields of engineering.

The customization of panels can be industrially achieved only if all the different requirements of these structures are contemporarily taken into consideration in the design phase. Therefore, to have an optimized design, efficient and accurate MDO processes must be set up. Nevertheless, these iterative processes requires the computation of the performance parameters of the target component several times.

If the static mechanical properties can be derived with FE methods in relatively short time, other properties, such as crash or acoustic simulations, are very time consuming. The main reason is that, to accurately reproduce with FE techniques the 3D panel geometry, including the complex shaped cores, would require a very fine mesh. This detailed mesh, together with typical big overall dimensions of the structures involved, implies the model to be very computationally expensive due to the great number of elements and nodes.

In this context, in the present dissertation, an analytical formulation to represent the complex shaped core as an equivalent homogeneous layer is proposed. The process is usually referred to as *homogenization* and have been already applied to different core typologies. Nevertheless, the analytical formulations developed in the literature were specific for only one kind of core. The lack of a general analytical formulation is highlighted in the state-of-the-art analysis in Chapter 2, together with other critical issues of the existing formulations. The objective of the first part of the dissertation, Chapter 3 was therefore to present an innovative general analytical formulation to overcome all the major drawbacks of the existing ones. In particular, the main contributions in this field can be summarized by the characteristics of the developed formulation as follows.

Generality. The formulation proposed is valid for every corrugation profile, since it is based on a Fourier series representation of the core shape. The validity for the most common core shapes was proved by means of comparisons with specific formulations available in the literature.

Asymmetry. No single formulations was found in the literature which could address also asymmetric profiles. The accuracy is proved for asymmetric shapes by comparing results with an FE-based formulation on a properly built validation case.

Beams or plates. The developed analytical formulation can easily be modified to be representative either of a beam-like or a plate-like structure. Usually, in the literature, only one case was considered.

2D or 3D. All the parameters for a solid description of the equivalent layer are given, even though typically only some of them are used, assuming a plate representation which disregard the through-thickness stresses and strains. Moreover, a Reissner-Mindlin representation of the equivalent plate layer is possible since both in-plane and out-of-plane shear moduli are derived analytically.

Sole core. The analytical formulation is developed to accurately represent the sole core. Nevertheless, the equivalent parameters for the complete panel can be easily derived as explained in the dissertation.

As already mentioned, particular attention was focused in the present work on sinusoidal core sandwich panels, which are the subject of Chapter 4. Indeed, given the absence in the literature of an accurate analytical formulation to homogenize such cores, the general formulation was simplified to obtain a specific, yet accurate, formulation for sinusoidal cores. The simplifications are due to the much easier analytical description of the corrugated curve (no Fourier series needed) and to the symmetry of the corrugation. Accuracy of results is comparable with the general formulation and was proven by means of comparisons with FE simulations and previous authors. Moreover, for this core shape, both static and acoustic, thus dynamic, validations of the equivalent modelling were carried out.

The most important validation of the analytical formulations was shown in Chapter 5. Indeed, in that chapter, results from a measurement campaign were compared with those from the analytical modelling. Measurements involved a tensile testing and a modal analysis on four panel configurations with sinusoidal corrugated cores. Such campaign, and particularly the modal part, proved the importance of an accurate representation of the core shape, which is possible only with the general formulation presented in this dissertation. Indeed, it was shown that the slight difference in the corrugation shape, due to the manufacturing process, can decrease the equivalent parameters of the core up to around 65%. This reduction was found on one transverse shear modulus and could not be disregarded because the modal behaviour of the total panel is strongly influenced by transverse shear moduli. The difference was less marked when comparing the tensile results for the equivalent in-plane Young's moduli. Indeed, the core has a smaller contribution to the overall behaviour, respect to the modal case. In both cases, the equivalent layered model was proven to be in good agreement with measurements.

The computational time needed to compute the acoustic properties for a 3D model of the corrugated sandwich panel is around 14 hours on a normal desktop computer and is reduced by the equivalent layered model to less than 2 minutes. This strong reduction can be used to include such property as a driving factor in an optimization process. Therefore, in Chapter 6, an MDO process was set up and solved to find a balance between two conflicting characteristics: bending stiffness and acoustic insulation of sinusoidal corrugated core panels. In particular, it was shown that an increase in the sound insulation by 2 dB and in the bending stiffness by 70%, was successfully reached at the cost of only 4% mass increase. Even though the pilot nature of this study is evident, the aim of that study was to prove the potentiality of such an MDO tool, which would not have been possible without the homogenization technique proposed in this dissertation.

Interesting peculiarities of corrugated core panels were highlighted in this dissertation and would require a deeper investigation in future works. In particular, concerning the analytical formulation developed, different behaviours in pure shear were observed in a generic x_1x_2*-plane* when applying the load in the x_1- or x_2-*direction*. This phenomenon should be further investigated and possibly checked with experimental tests.

Moreover, the typical way to deal with the obtained multi-layer panel is to assume perfect bonding between layers. Nevertheless, since the coupling between core and faces is not continuous, the effect of this assumption could be investigated. This is particularly true when local effects, e.g. localized strains or stresses, are desired in the future.

Another observation involves the connection between core and faces of the corrugated sandwich panels, which was realized by means of a thick film of glue. Since the presence of the glue is not considered in the analytical modelling of the complete panel, a study on its influence would be of interest both on the static and dynamic behaviour of these structures.

Finally, the field that has probably more room for improvement is the MDO of these structures, which can be extended in several ways: addition of constraints, different optimization algorithms, inclusion of different sub-assembly, etc.

Appendix A

Experimental stress-strain curves

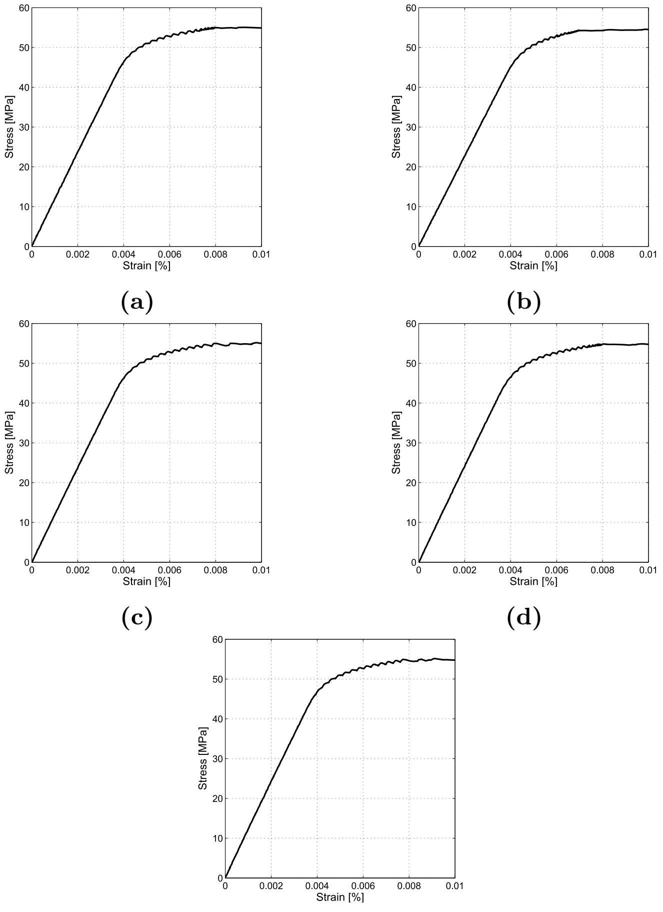

(a)

(b)

(c)

(d)

(e)

Figure A.1: Panel 05_02_05 H6 – *x-direction*

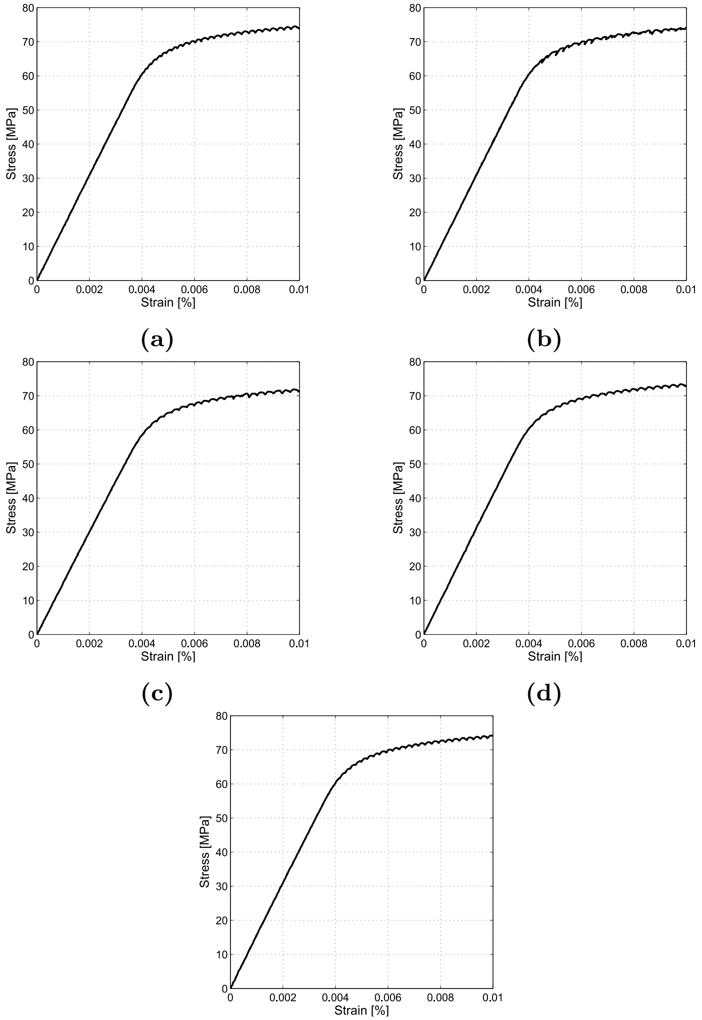

Figure A.2: Panel 05_02_05 H6 – *y-direction*

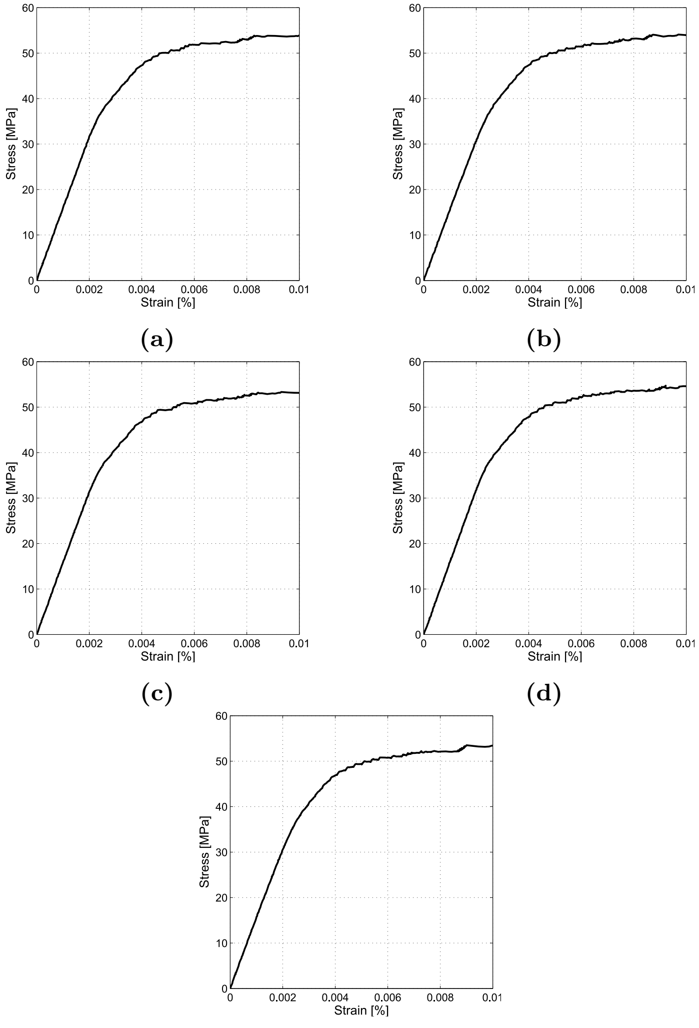

(a) **(b)** **(c)** **(d)** **(e)**

Figure A.3: Panel 08_02_05 H6 – *x-direction*

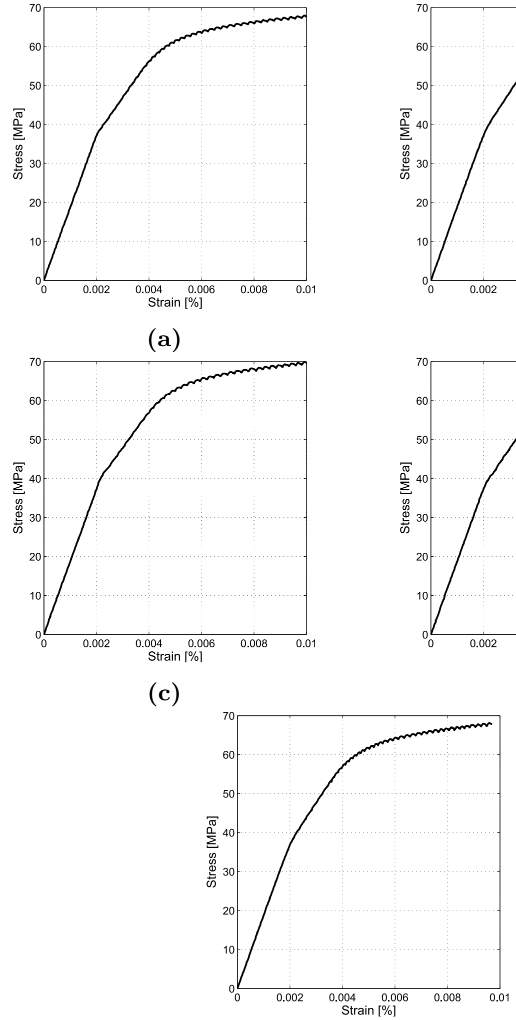

(a)

(b)

(c)

(d)

(e)

Figure A.4: Panel 08_02_05 H6 – *y-direction*

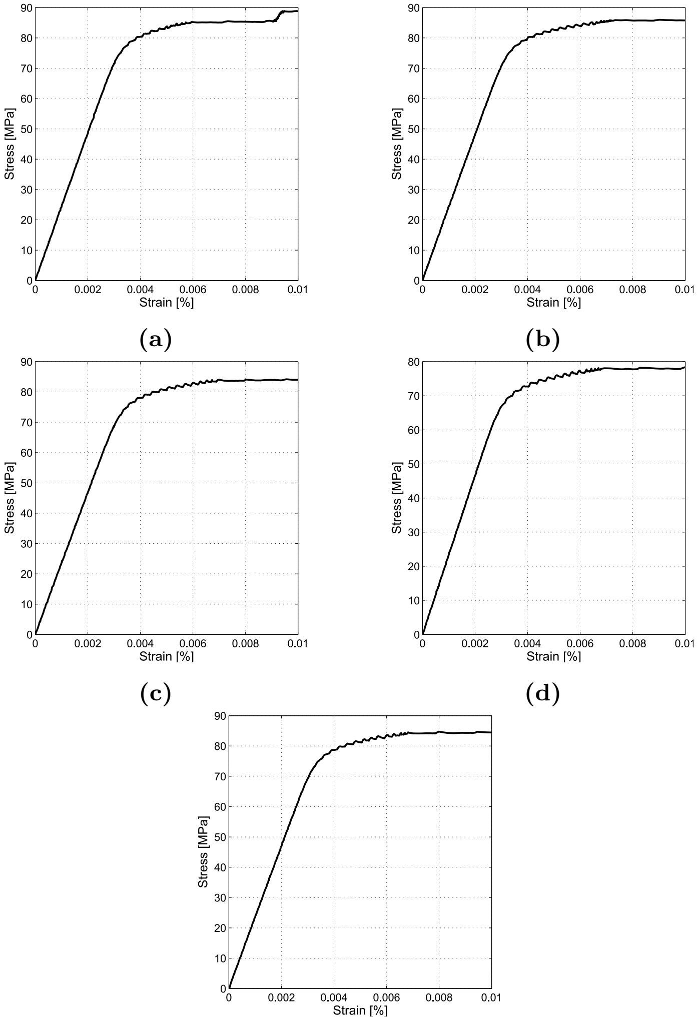

(a)

(b)

(c)

(d)

(e)

Figure A.5: Panel 10_03_10 H6 – *x-direction*

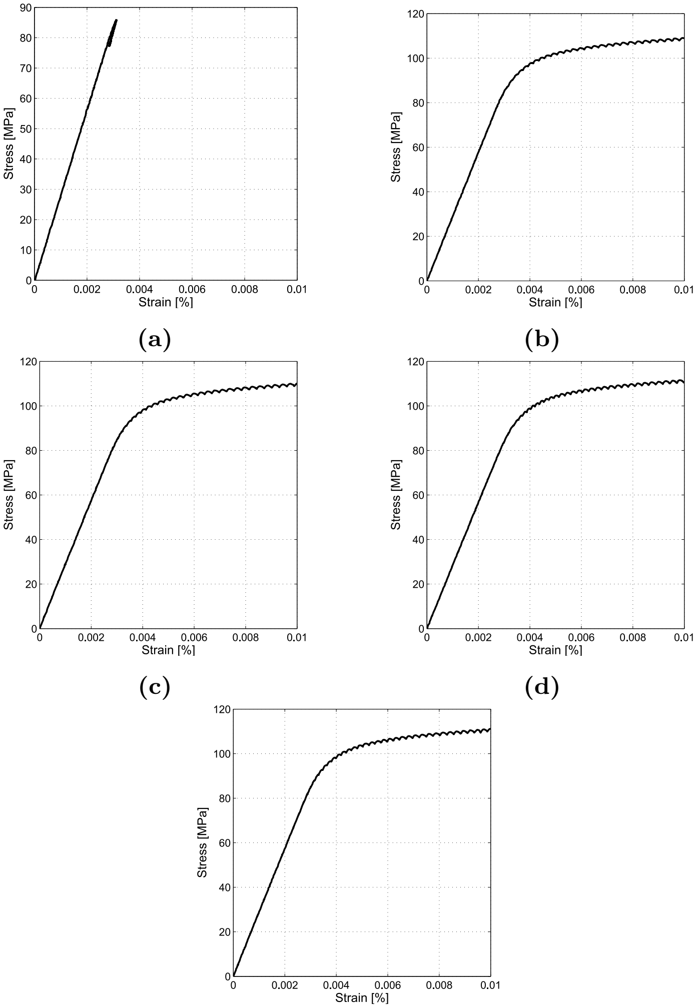

(a) **(b)**

(c) **(d)**

(e)

Figure A.6: Panel 10_03_10 H6 – *y-direction*

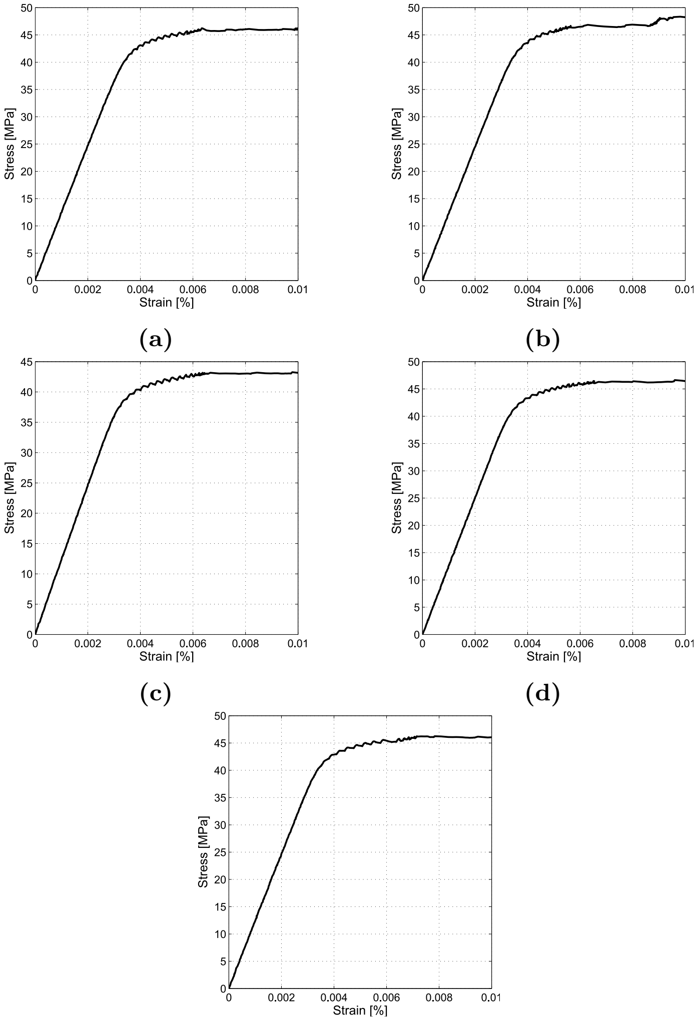

(a) **(b)** **(c)** **(d)** **(e)**

Figure A.7: Panel 10_03_10 H11.5 – *x-direction*

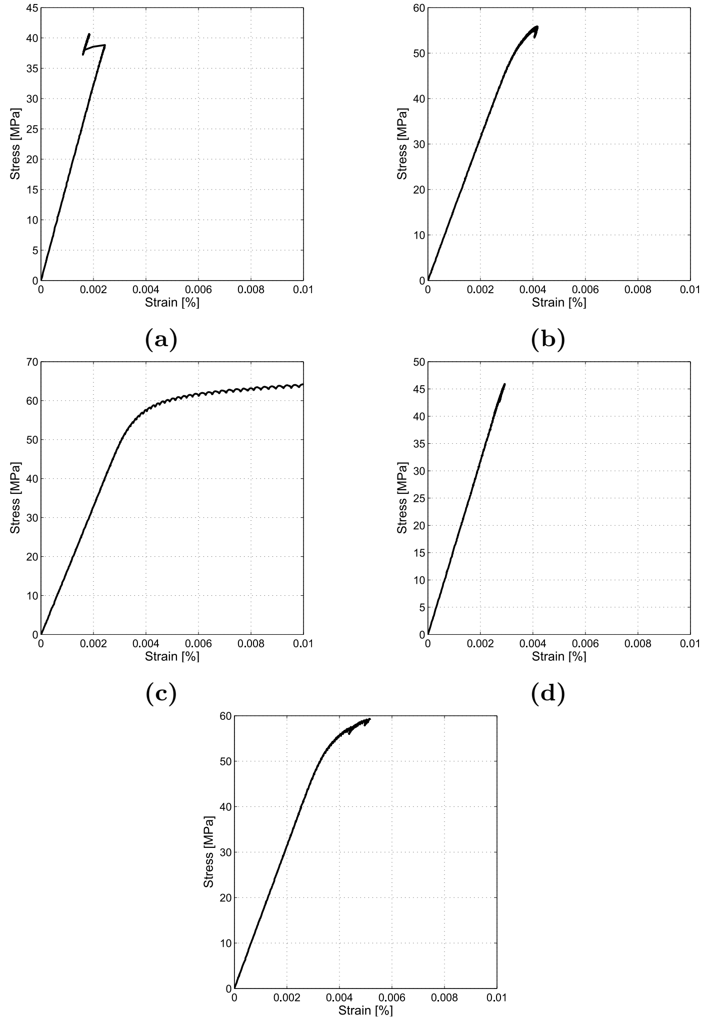

(a) **(b)** **(c)** **(d)** **(e)**

Figure A.8: Panel 10_03_10 H11.5 – *y-direction*

Appendix B

Datasheets of tested panels

Among the several different configurations of sinusoidal core sandwich panels available on the market, the four which were deeply investigated and experimentally tested in the present dissertation were supplied by the german Metawell Company [1]. Information from the supplier are included in the datasheets given in the following.

---

[1] Metawell GmbH – Metal Sandwich Technology – *http://www.metawell.de/en/metawell-aluminium-sandwich-panels-and-lightweight-components/*

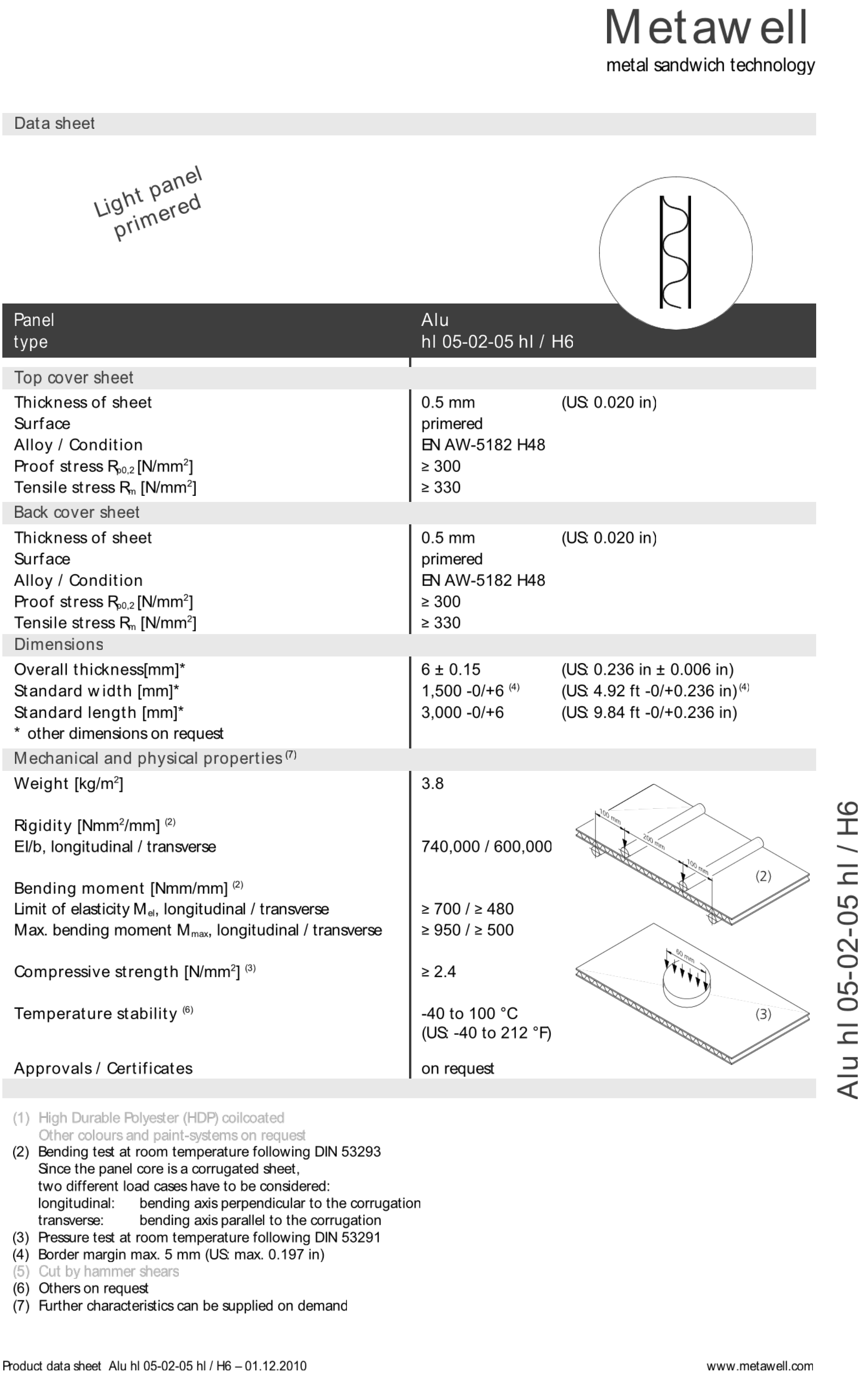

Metawell

metal sandwich technology

Data sheet

Light panel primered

Panel type	Alu hl 05-02-05 hl / H6	
Top cover sheet		
Thickness of sheet	0.5 mm	(US: 0.020 in)
Surface	primered	
Alloy / Condition	EN AW-5182 H48	
Proof stress $R_{p0,2}$ [N/mm^2]	≥ 300	
Tensile stress R_m [N/mm^2]	≥ 330	
Back cover sheet		
Thickness of sheet	0.5 mm	(US: 0.020 in)
Surface	primered	
Alloy / Condition	EN AW-5182 H48	
Proof stress $R_{p0,2}$ [N/mm^2]	≥ 300	
Tensile stress R_m [N/mm^2]	≥ 330	
Dimensions		
Overall thickness[mm]*	6 ± 0.15	(US: 0.236 in ± 0.006 in)
Standard width [mm]*	1,500 -0/+6 (4)	(US: 4.92 ft -0/+0.236 in) (4)
Standard length [mm]*	3,000 -0/+6	(US: 9.84 ft -0/+0.236 in)
* other dimensions on request		
Mechanical and physical properties (7)		
Weight [kg/m^2]	3.8	
Rigidity [Nmm^2/mm] (2) EI/b, longitudinal / transverse	740,000 / 600,000	
Bending moment [Nmm/mm] (2)		
Limit of elasticity M_{el}, longitudinal / transverse	≥ 700 / ≥ 480	
Max. bending moment M_{max}, longitudinal / transverse	≥ 950 / ≥ 500	
Compressive strength [N/mm^2] (3)	≥ 2.4	
Temperature stability (6)	-40 to 100 °C (US: -40 to 212 °F)	
Approvals / Certificates	on request	

Alu hl 05-02-05 hl / H6

(1) High Durable Polyester (HDP) coilcoated
Other colours and paint-systems on request
(2) Bending test at room temperature following DIN 53293
Since the panel core is a corrugated sheet,
two different load cases have to be considered:
longitudinal: bending axis perpendicular to the corrugation
transverse: bending axis parallel to the corrugation
(3) Pressure test at room temperature following DIN 53291
(4) Border margin max. 5 mm (US: max. 0.197 in)
(5) Cut by hammer shears
(6) Others on request
(7) Further characteristics can be supplied on demand

Metawell
metal sandwich technology

Data sheet

All-round-panel
primered

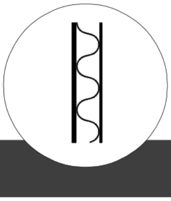

Panel type	Alu hl 08-02-05 hl / H6	
Top cover sheet		
Thickness of sheet	0.8 mm	(US: 0.032 in)
Surface	primered	
Alloy / Condition	EN AW-5754 H42	
Proof stress $R_{p0,2}$ [N/mm^2]	≥ 140	
Tensile stress R_m [N/mm^2]	≥ 220	
Back cover sheet		
Thickness of sheet	0.5 mm	(US: 0.020 in)
Surface	primered	
Alloy / Condition	EN AW-5182 H48	
Proof stress $R_{p0,2}$ [N/mm^2]	≥ 300	
Tensile stress R_m [N/mm^2]	≥ 330	
Dimensions		
Overall thickness [mm]*	6.0 ± 0.15	(US: 0.217 in ± 0.006 in)
Standard width [mm]*	1,500 -0/+6 (4)	(US: 4.92 ft -0/+0.236 in) (4)
Standard length [mm]*	3,000 -0/+6	(US: 9.84 ft -0/+0.236 in)
* other dimensions on request		
Mechanical and physical properties (7)		
Weight [kg/m^2]	4.6	
Rigidity [Nmm^2/mm] (2) EI/b, longitudinal / transverse	700,000 / 625,000	
Bending moment [Nmm/mm] (2) Limit of elasticity M_{el}, longitudinal / transverse Max. bending moment M_{max}, longitudinal / transverse	≥ 550 / ≥ 500 ≥ 900 / ≥ 600	
Compressive strength [N/mm^2] (3)	≥ 3.0	
Temperature stability (6)	-40 to 100 °C (US: -40 to 212 °F)	
Approvals / Certificates	on request	

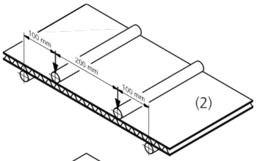

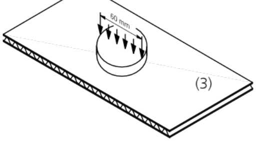

Alu hl 08-02-05 hl / H6

(1) High Durable Polyester (HDP) coilcoated
Other colours and paint-systems on request
(2) Bending test at room temperature following DIN 53293
Since the panel core is a corrugated sheet,
two different load cases have to be considered:
longitudinal: bending axis perpendicular to the corrugation
transverse: bending axis parallel to the corrugation
(3) Pressure test at room temperature following DIN 53291
(4) Border margin max. 5 mm (US: max. 0.197 in)
(5) Cut by hammer shears
(6) Others on request
(7) Further characteristics can be supplied on demand

Metawell
metal sandwich technology

Data sheet

High compressive strength
ideal for floors

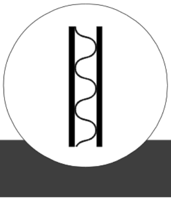

Panel type	Alu hl 10-03-10 hl / H6	
Top cover sheet		
Thickness of sheet	1.0 mm	(US: 0.039 in)
Surface	primered	
Alloy / Condition	EN AW-5754 H48	
Proof stress $R_{p0,2}$ [N/mm^2]	≥ 220	
Tensile stress R_m [N/mm^2]	≥ 280	
Back cover sheet		
Thickness of sheet	1.0 mm	(US: 0.039 in)
Surface	primered	
Alloy / Condition	EN AW-5754 H48	
Proof stress $R_{p0,2}$ [N/mm^2]	≥ 220	
Tensile stress R_m [N/mm^2]	≥ 280	
Dimensions		
Overall thickness [mm]*	6 ± 0.2	(US: 0.236 in ± 0.008 in)
Standard width [mm]*	1,500 -0/+6 (4)	(US: 4.92 ft -0/+0.236 in) (4)
Standard length [mm]*	3,000 -0/+6	(US: 9.84 ft -0/+0.236 in)
* other dimensions on request		
Mechanical and physical properties (7)		
Weight [kg/m^2]	6.9	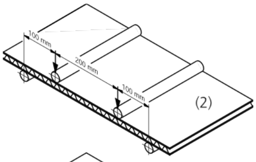
Rigidity [Nmm^2/mm] (2) EI/b, longitudinal / transverse	1.1 E+6 / 1.0 E+6	
Bending moment [Nmm/mm] (2)		
Limit of elasticity M_{el}, longitudinal / transverse	≥ 1,000 / ≥ 900	
Max. bending moment M_{max}, longitudinal / transverse	≥ 1,250 / ≥ 1,000	
Compressive strength [N/mm^2] (3)	≥ 12	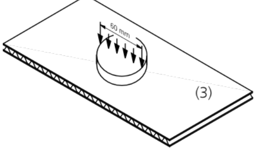
Temperature stability (6)	-40 to 100 °C (US: -40 to 212 °F)	
Approvals / Certificates	on request	

(1) High Durable Polyester (HDP) coilcoated
Other colours and paint-systems on request
(2) Bending test at room temperature following DIN 53293
Since the panel core is a corrugated sheet,
two different load cases have to be considered:
longitudinal: bending axis perpendicular to the corrugation
transverse: bending axis parallel to the corrugation
(3) Pressure test at room temperature following DIN 53291
(4) Border margin max. 5 mm (US: max. 0.197 in)
(5) Cut by hammer shears
(6) Others on request
(7) Further characteristics can be supplied on demand

Alu hl 10-03-10 hl / H6

Metawell
metal sandwich technology

Data sheet

Very rigid panel
with high load-bearing capacity

Panel type	Alu hl 10-03-10 hl / H11.5	
Top cover sheet		
Thickness of sheet	1.0 mm	(US: 0.039 in)
Surface	primered	
Alloy / Condition	EN AW-5754 H48	
Proof stress $R_{p0,2}$ [N/mm^2]	≥ 220	
Tensile stress R_m [N/mm^2]	≥ 280	
Back cover sheet		
Thickness of sheet	1.0 mm	(US: 0.039 in)
Surface	primered	
Alloy / Condition	EN AW-5754 H48	
Proof stress $R_{p0,2}$ [N/mm^2]	≥ 220	
Tensile stress R_m [N/mm^2]	≥ 280	
Dimensions		
Overall thickness [mm]*	11.5 ± 0.2	(US: 0.453 in ± 0.008 in)
Standard width [mm]*	1,500 -0/+6 (4)	(US: 4.92 ft -0/+0.236 in) (4)
Standard length [mm]*	3,000 -0/+6	(US: 9.84 ft -0/+0.236 in)
* other dimensions on request		
Mechanical and physical properties (7)		
Weight [kg/m^2]	7.2	
Rigidity [Nmm^2/mm] (2) EI/b, longitudinal / transverse	5.1 E+6 / 3.5 E+6	
Bending moment [Nmm/mm] (2) Limit of elasticity M_{el}, longitudinal / transverse	≥ 2,200 / ≥ 900	
Max. bending moment M_{max}, longitudinal / transverse	≥ 3,000 / ≥ 1,000	
Compressive strength [N/mm^2] (3)	≥ 3.75	
Temperature stability (6)	-40 to 100 °C (US: -40 to 212 °F)	
Approvals / Certificates	on request	

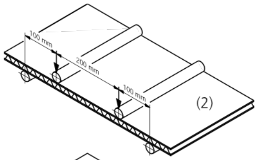

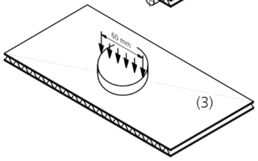

Alu hl 10-03-10 hl / H11.5

(1) High Durable Polyester (HDP) coilcoated
Other colours and paint-systems on request
(2) Bending test at room temperature following DIN 53293
Since the panel core is a corrugated sheet,
two different load cases have to be considered:

longitudinal:	bending axis perpendicular to the corrugation
transverse:	bending axis parallel to the corrugation

(3) Pressure test at room temperature following DIN 53291
(4) Border margin max. 5 mm (US: max. 0.197 in)
(5) Cut by hammer shears
(6) Others on request
(7) Further characteristics can be supplied on demand

Bibliography

[1] S. Timoshenko and S. Woinowsky-Krieger. *Theory of plates and shells.* McGraw-Hill, New York, 1959.

[2] Q. H. Cheng, H. P. Lee, and C. Lu. A numerical analysis approach for evaluating elastic constants of sandwich structures with various cores. *Composite Structures*, 74(2):226–236, July 2006.

[3] J. Mackerle. Finite element analyses of sandwich structures: a bibliography (1980 – 2001). *Engineering Computations*, 19(2):206–245, 2002.

[4] M. Grediac. A finite element study of the transverse shear in honeycomb cores. *International Journal of Solids and Structures*, 30(13):1777–1788, January 1993.

[5] A. K. Noor and W. S. Burton. Assessment of continuum models for sandwich panel honeycomb cores. *Computer methods in applied mechanics and engineering*, 145(3):341–360, 1997.

[6] L. J. Gibson, M. F. Ashby, G. S. Schajer, and C. I. Robertson. The mechanics of two-dimensional cellular materials. In *Proceedings of the Royal Society of London. Series A, Mathematical and Physical Sciencies*, volume 382, pages 25–42, 1982.

[7] X. F. Xu and P. Qiao. Homogenized elastic properties of honeycomb sandwich with skin effect. *International Journal of Solids and Structures*, 39(8):2153–2188, April 2002.

[8] S. O. Oghumu. *Finite element modeling approach and performance evaluation of fiber reinforced polymer sandwich bridge panels.* Msc thesis, Louisiana State University, USA, 2005.

[9] A. Chen and J. F. Davalos. Transverse Shear Including Skin Effect for Composite Sandwich with Honeycomb Sinusoidal Core. *Journal of Engineering Mechanics*, 133(3):247–256, March 2007.

[10] P. Qiao and J. Wang. Mechanics of Composite Sinusoidal Honeycomb Cores. *Journal of Aerospace Engineering*, 18(1):42–50, 2005.

[11] T. Liu, Z. C. Deng, and T. J. Lu. Structural modeling of sandwich structures with lightweight cellular cores. *Acta Mechanica Sinica*, 23(5):545–559, July 2007.

[12] J. Hohe and W. Becker. Effective stress-strain relations for two-dimensional cellular sandwich cores: Homogenization, material models, and properties. *Applied Mechanics Reviews*, 55(1):61–87, 2002.

[13] H. X. Wang and S. W. Chung. Equivalent Elastic Constants of Truss Core Sandwich Plates. *Journal of Pressure Vessel Technology*, 133(4):1–6, 2011.

[14] C. Libove and S. B. Batdorf. A general small-deflection theory for flat sandwich plates. Technical report, NACA Report 899, Washington, D.C., USA, 1948.

[15] L. Valdevit, Z. Wei, C. Mercer, F. W. Zok, and A. G. Evans. Structural performance of near-optimal sandwich panels with corrugated cores. *International Journal of Solids and Structures*, 43(16):4888–4905, August 2006.

[16] L. Valdevit, J. W. Hutchinson, and A. G. Evans. Structurally optimized sandwich panels with prismatic cores. *International Journal of Solids and Structures*, 41(18-19):5105–5124, September 2004.

[17] D. Briassoulis. Equivalent orthotropic properties of corrugated sheets. *Computers & Structures*, 23(2):129–138, January 1986.

[18] G. Kress and M. Winkler. Corrugated laminate homogenization model. *Composite Structures*, 92(3):795–810, February 2010.

[19] M. Winkler and G. Kress. Deformation limits for corrugated cross-ply laminates. *Composite Structures*, 92(6):1458–1468, May 2010.

[20] G. Kress and M. Winkler. Corrugated laminate analysis: A generalized plane-strain problem. *Composite Structures*, 93(5):1493–1504, April 2011.

[21] M. Winkler and G. Kress. Influence of corrugation geometry on the substitute stiffness matrix of corrugated laminates. *Composite Structures*, 94(9):2827–2833, September 2012.

[22] T. Yokozeki, S. I. Takeda, T. Ogasawara, and T. Ishikawa. Mechanical properties of corrugated composites for candidate materials of flexible wing structures. *Composites Part A: Applied Science and Manufacturing*, 37(10):1578–1586, October 2006.

[23] Y. Xia, M. I. Friswell, and E. I. S. Flores. Equivalent models of corrugated panels. *International Journal of Solids and Structures*, 49(13):1453–1462, June 2012.

[24] C. Libove and R. F. Hubka. Elastic constants for corrugated core sandwich plates. Technical report, NACA Technical Notes TN-2289, Washington, D.C., USA, 1951.

[25] W. L. Ko. Elastic constants for superplastically formed/diffusion-bonded sandwich structures. Technical report, NASA Technical Paper TP-1562, Edwards, California, USA, 1980.

[26] A. Samanta and M. Mukhopadhyay. Finite element static and dynamic analyses of folded plates. *Engineering Structures*, 21(3):277–287, 1999.

[27] C. A. Castigliano. *Intorno ai sistemi elastici.* Dissertation, Politecnico di Torino, IT, 1873.

[28] W. S. Chang, E. Ventsel, T. Krauthammer, and J. John. Bending behavior of corrugated-core sandwich plates. *Composite Structures*, 70(1):81–89, 2005.

[29] T. S. Lok and Q. H. Cheng. Elastic stiffness properties and behavior of truss-core sandwich panel. *Journal of Structural Engineering*, 126(May):552–559, 2000.

[30] K. M. Liew, L. X. Peng, and S. Kitipornchai. Vibration analysis of corrugated Reissner-Mindlin plates using a mesh-free Galerkin method. *International Journal of Mechanical Sciences*, 51(9-10):642–652, September 2009.

[31] K. M. Liew, L. X. Peng, and S. Kitipornchai. Nonlinear analysis of corrugated plates using a FSDT and a meshfree method. *Computer Methods in Applied Mechanics and Engineering*, 196(21-24):2358–2376, April 2007.

[32] P. Isaksson, A. Krusper, and P. A. Gradin. Shear correction factors for corrugated core structures. *Composite Structures*, 80(1):123–130, September 2007.

[33] G. A. Baum, D. C. Brennan, and C. C. Haberger. Orthotropic elastic constants of paper. *Tappi Journal*, 64:97–101, 1981.

[34] Z. Aboura, N. Talbi, S. Allaoui, and M. L. Benzeggagh. Elastic behavior of corrugated cardboard: experiments and modeling. *Composite Structures*, 63(1):53–62, January 2004.

[35] N. Talbi, A. Batti, R. Ayad, and Y. Q. Guo. An analytical homogenization model for finite element modelling of corrugated cardboard. *Composite Structures*, 88(2):280–289, April 2009.

[36] T. Nordstrand, L. A. Carlsson, and H. G. Allen. Transverse shear stiffness of structural core sandwich. *Composite Structures*, 27(3):317–329, 1994.

[37] J. R. Vinson and S. Shore. Structural Optimization of Corrugated Core and Web Core Sandwich Panels Subjected to Uniaxial Compression. Technical report, AD0654936, STRUCTURAL MECHANICS ASSOCIATES NARBERTH PA, 1967.

[38] J. R. Vinson and S. Shore. Minimum weight corrugated-core sandwich panels subjected to uniaxial compression. *Fibre Science and Technology*, 1(2):151–163, October 1968.

[39] J. R. Vinson. Optimum design of composite honeycomb sandwich panels subjected to uniaxial compression. *AIAA Journal*, 24(10):1690–1696, October 1986.

[40] J. S. Lamancusa. Numerical optimization techniques for structural-acoustic design of rectangular panels. *Computers & Structures*, 48(4):661–675, August 1993.

[41] J. S. Lamancusa and H. A. Eschenauer. Design optimization methods for rectangular panels with minimal sound radiation. *AIAA Journal*, 32(3):472–479, March 1994.

[42] C. A. Coello Coello and A. D. Christiansen. Multiobjective optimization of trusses using genetic algorithms. *Computers & Structures*, 75(6):647–660, May 2000.

[43] J. W. Hutchinson and M. Y. He. Buckling of cylindrical sandwich shells with metal foam cores. *International Journal of Solids and Structures*, 37(46-47):6777–6794, November 2000.

[44] Z. Xue and J. W. Hutchinson. A comparative study of impulse-resistant metal sandwich plates. *International Journal of Impact Engineering*, 30(10):1283–1305, November 2004.

[45] J. W. Hutchinson and Z. Xue. Metal sandwich plates optimized for pressure impulses. *International Journal of Mechanical Sciences*, 47(4-5):545–569, April 2005.

[46] S. Gu, T. J. Lu, and A. G. Evans. On the design of two-dimensional cellular metals for combined heat dissipation and structural load capacity. *International Journal of Heat and Mass Transfer*, 44(11):2163–2175, June 2001.

[47] J. S. Liu and T. J. Lu. Multi-objective and multi-loading optimization of ultralightweight truss materials. *International Journal of Solids and Structures*, 41(3-4):619–635, February 2004.

[48] Y. S. Tian and T. J. Lu. Optimal design of compression corrugated panels. *Thin-Walled Structures*, 43(3):477–498, March 2005.

[49] A. E. H. Love. The Small Free Vibrations and Deformation of a Thin Elastic Shell. *Philosophical Transactions of the Royal Society A: Mathematical, Physical and Engineering Sciences*, 179(January):491–546, January 1888.

[50] L. Euler. De curvis elasticis. *Lausanne und Genf*, pages 245–310, 1744.

[51] D. Bernoulli. De vibrationibus et sono laminarum elasticarum. *Commentarii Academiae Scientiarum Imperialis Petropolitanae*, 13:105–120, 1751.

[52] R. D. Mindlin. Influence of rotatory inertia and shear on flexural motions of isotropic, elastic plates. *Journal of Applied Mechanics*, 18:31–38, 1951.

[53] E. Reissner. The effect of transverse shear deformation on the bending of elastic plates. *Journal of Applied Mechanics*, 12(A):69–77, 1945.

[54] S. P. Timoshenko. On the transverse vibrations of bars of uniform cross-section. *Philosophical Magazine*, 43(6):125–131, 1922.

[55] A. H. Nilson and A. R. Ammar. Finite element analysis of metal deck shear diaphragms. *Journal of the Structural Division*, 100(4):711–726, 1974.

[56] G. Bartolozzi, M. Pierini, U. Orrenius, and N. Baldanzini. An equivalent material formulation for sinusoidal corrugated cores of structural sandwich panels. *Composite Structures*, 100:173–185, June 2013.

[57] N. Buannic, P. Cartraud, and T. Quesnel. Homogenization of corrugated core sandwich panels. *Composite Structures*, 59(3):299–312, 2003.

[58] G. Bartolozzi, U. Orrenius, A. Pratellesi, and M. Pierini. An equivalent orthotropic plate model for sinusoidal core sandwich panels in optimization processes. In *Proceedings of NOVEM2012*, Sorrento, IT, 2012.

[59] G. Bartolozzi, M. Pierini, and U. Orrenius. Handling of acoustic constraints in multidisciplinary optimization processes. In *Proceedings of ISMA2012*, pages 3679–3694, Leuven, BE, 2012.

[60] MSC.Software. MD Nastran 2010r1, Quick reference guide, 2010.

[61] DIN53293. Testing of sandwiches; Bending test, 1982.

[62] V. Cotoni, R. S. Langley, and P. J. Shorter. A statistical energy analysis subsystem formulation using finite element and periodic structure theory. *Journal of Sound and Vibration*, 318(4-5):1077–1108, December 2008.

[63] American Society for Testing and Materials. *ASTM C297 - Standard Test Method for Flatwise Tensile Strength of Sandwich Construction.* 2004.

[64] American Society for Testing and Materials. *ASTM C365 - Standard Test Method for Flatwise Compressive Properties of Sandwich Cores.* 2003.

[65] American Society for Testing and Materials. *ASTM C273 - Standard Test Method for Shear Properties of Sandwich Core Materials.* 2000.

[66] American Society for Testing and Materials. *ASTM E8 - Standard Test Methods for Tension Testing of Metallic Materials.* 2008.

[67] American Society for Testing and Materials. *ASTM D3039 - Standard Test Method for Tensile Properties of Polymer Matrix Composite Materials.* 2008.

[68] P. Wennhage. *Structural - Acoustic Optimization of Sandwich Panels.* PhD thesis, Royal Institute of Technology - Stockholm, Sweden, 2001.

[69] C. J. Cameron. *Design of Multifunctional Body Panels for Conflicting Structural and Acoustic Requirements in Automotive Applications.* PhD thesis, Doctoral Thesis, KTH, 2011.

[70] Mathworks. MATLAB R2010a, User Manual, 2010.

[71] R. Barrett, M. Berry, T. F. Chan, J. Demmel, J. Donato, J. Dongarra, V. Eijkhout, R. Pozo, C. Romine, and H. van der Vorst. *Templates for the Solution of Linear Systems: Building Blocks for Iterative Methods.* Society for Industrial and Applied Mathematics, January 1994.

[72] R. A. Waltz, J. L. Morales, J. Nocedal, and D. Orban. An interior algorithm for nonlinear optimization that combines line search and trust region steps. *Mathematical Programming*, 107(3):391–408, November 2005.

[73] K. Schittkowski. NLQPL: A FORTRAN-Subroutine Solving Constrained Nonlinear Programming Problems. *Annals of Operations Research*, 5:485–500, 1985.

[74] P. E. Gill, S. M. Cobb, W. Murray, and M. H. Wright. *Practical Optimization*, volume 66. Academic Press, New York, October 1981.

[75] J. Arora. *Introduction to optimum design.* Elsevier Academic Press, 2004.

[76] W. Karush. *Minima of Functions of Several Variables with Inequalities as Side Constraints.* PhD thesis, M.Sc. Dissertation, University of Chicago, 1939.

[77] H. W. Kuhn and A. W. Tucker. Nonlinear programming. In *Proceedings of 2nd Berkeley Symposium*, number x, pages 481–492, Berkeley, 1951.

[78] R. Courant. Variational methods for the solution of problems of equilibrium and vibrations. *Bull. Amer. Math. Soc*, 49:1–23, 1943.

[79] A. F. Kuri-Morales and J. Gutiérrez-García. Penalty function methods for constrained optimization with genetic algorithms: A statistical analysis. In *MICAI 2002: Advances in Artificial Intelligence*, pages 187–200, Yucatan, Mexico, 2002.

[80] C. A. Coello Coello. Theoretical and numerical constraint-handling techniques used with evolutionary algorithms: a survey of the state of the art. *Computer Methods in Applied Mechanics and Engineering*, 191(11-12):1245–1287, January 2002.

[81] A. R. Conn, N. Gould, and P. Toint. A globally convergent augmented Lagrangian algorithm for optimization with general constraints and simple bounds. *SIAM Journal on Numerical Analysis*, 28(2):545–572, 1991.

[82] A. R. Conn, N. Gould, and P. L. Toint. A globally convergent Lagrangian barrier algorithm for optimization with general inequality constraints and simple bounds. *Mathematics of Computation*, 66(217):261–289, January 1997.

[83] T. A. El-Mihoub, A. A. Hopgood, L. Nolle, and A. Battersby. Hybrid Genetic Algorithms: A Review. *Engineering Letters*, 13(2):124–137, 2006.

[84] D. Beasley, R. R. Martin, and D. R. Bull. An overview of genetic algorithms: Part 1. Fundamentals. *University computing*, 15:58–69, 1993.

[85] ESI. VA One 2012, User's manual, 2012.

[86] ISO717-1:1996+AM1:2006. *Rating of sound insulation in buildings and of building elements -Part 1: Airborne sound insulation.* International Organization for Standardization, 2006.

Acknowledgements

The biggest part of the research presented in this dissertation has been carried out at the Department of Industrial Engineering, at the University of Florence. The research was partially funded by the European Commission within the MID-MOD project (GA-2009-218508), during a secondment of six months at Bombardier Transportation Sweden, in Västerås. In addition, the support provided by ESI R&D regarding software licensing is highly appreciated.

Many people have contributed to this thesis in one way or another. First, this work has been made possible by my supervisor Prof. Marco Pierini: thank you for having given me the opportunity to do my PhD, but most importantly for believing in me. A particular thank you is for Dr. Niccolò Baldanzini for his support, especially in the last part of the project. Thanks to Dr. Ulf Orrenius, who gave his valuable contribution in terms of knowledge and experience from an industrial point of view, supervising me in Sweden. Heart-felt thanks to my ex co-supervisor Dr. Alessandro Pratellesi, who guided me in the first year.

I wish to express my gratitude to all my colleagues, past and present, from Via Rossi, who made the working days look shorter. A special thank you is for my office mate Daniele, who is now a friend more than a colleague...but please, stop formatting PCs, really, you are being addicted!

Special thanks are for the things that would not need it: every note played or sung and every line recited is essential to me. Nevertheless, they would be nothing without the guys who share their passions with me: thanks everybody!

To all my friends, near or far away, because I know I can count on you every time I need. In particular Marta and Stefano: I couldn't even imagine it was possible to share our lives as much as we do.

To my family, who has always supported me in so many ways...thank you, especially Niccolò and Greta, who bring the future in our lives.

But first and foremost, I would like to thank Silvia, for putting up with me every day. Your love makes everything easier.

Giorgio Bartolozzi,
Florence, December 2013

Ringraziamenti

La maggior parte della ricerca presentata in questa tesi è stata svolta presso il Dipartimento di Ingegneria Industriale, Università degli Studi di Firenze. La ricerca è stata in parte finanziata dalla Commissione Europea all'interno del progetto MID-MOD (GA-2009-218508), durante un soggiorno di sei mesi presso Bombardier Transportation Sweden, a Västerås. Inoltre, il supporto fornito da ESI R&D per quanto riguarda le licenze del software è fortemente apprezzato.

Molte persone hanno contribuito a questa tesi, in un modo o nell'altro. Innanzitutto, questo lavoro è stato reso possibile dal Prof. Marco Pierini: grazie per avermi dato questa opportunità, ma ancor di più per la fiducia riposta in me. Un grazie particolare al Dott. Niccolò Baldanzini per il suo supporto, specialmente nell'ultima parte dell'attività. Grazie al Dott. Ulf Orrenius, che ha fornito il suo prezioso contributo in termini di conoscenza e esperienza da un punto di vista industriale durante, e non solo, la sua supervisione in Svezia. Un ringraziamento di cuore al mio ex "capo" Alessandro, che mi ha guidato nel primo anno.

Vorrei esprimere la mia gratitudine a tutti i colleghi di Via Rossi, presenti e passati, che hanno alleggerito le giornate lavorative. Soprattutto, un grazie speciale al mio compagno di ufficio Daniele, che è adesso un amico più che un collega...ma per favore, basta formattare i computer, davvero, stai diventando dipendente!

Ringraziamenti particolari per le cose che non ne hanno bisogno: ogni battuta recitata e ogni nota suonata o cantata sono per me essenziali. Tuttavia, non sarebbero possibili senza tutte le persone che condividono con me la loro passione: grazie a tutti!

A tutti i miei amici, vicini e lontani, perchè so di poter contare su di voi quando ne ho bisogno. Specialmente Marta e Stefano: non pensavo fosse possibile condividere le nostre vite così a fondo.

Alla mia famiglia, che mi ha sempre supportato in innumerevoli modi...grazie! Soprattutto a Niccolò e Greta, che portano il futuro nelle nostre vite.

Ma soprattutto voglio ringraziare Silvia che mi sopporta ogni giorno. Il tuo amore rende tutto più semplice.

Giorgio Bartolozzi,
Firenze, Dicembre 2013

List of publications

International peer reviewed journal articles

G. Bartolozzi, M. Pierini, U. Orrenius, N. Baldanzini. An equivalent material formulation for sinusoidal corrugated cores of structural sandwich panels. *Composite Structures*, 100:173-185, June 2013. doi: 10.1016/j.compstruct.2012.12.042.

G. Bartolozzi, N. Baldanzini, M. Pierini. Equivalent properties for corrugated cores of sandwich structures: A general analytical method. *Composite Structures*, 108:736-746, February 2014. doi:10.1016/j.compstruct.2013.10.012.

G. Bartolozzi, M. Pierini, N. Baldanzini, G. Zonfrillo. Experimental validation of analytical homogenization models for corrugated core sandwich panels. *Submitted to Composite Structures.*

Full papers in proceedings of international conferences

G. Bartolozzi, R. D'amico, A. Pratellesi and M. Pierini. An Efficient Method for Selecting CHIEF Points. In *Proceedings of the International Conference on Structural Dynamics EURODYN2011*, Leuven, Belgium, July 2011.

G. Bartolozzi, U. Orrenius, A. Pratellesi and M. Pierini. An Equivalent Orthotropic Plate Model for Sinusoidal Core Sandwich Panels in Optimization Processes. In *Proceedings of Noise and Vibration: Emerging Methods NOVEM2012*, Sorrento, Italy, April 2012.

G. Bartolozzi, M. Pierini and U. Orrenius. Handling of Acoustic Constraints in Multidisciplinary Optimization Processes. In *Proceedings of the International Conference on Noise and Vibration Engineering ISMA2012*, Leuven, Belgium, September 2012.